

**LEIBNIZ UNIVERSITÄT HANNOVER**

FAKULTÄT FÜR MATHEMATIK UND PHYSIK  
INSTITUT FÜR QUANTENOPTIK

**Temperature Measurement with Lanthanide  
doped Nanocrystals**

Von der Fakultät für Mathematik und Physik  
der Gottfried Wilhelm Leibniz Universität Hannover

zur Erlangung des akademischen Grades  
Doktor der Naturwissenschaften  
Dr. rer. nat.

genehmigte Dissertation von

JONAS THIEM

2022

REFERENT:

Prof. Dr. Detlev Ristau

KOREFERENTEN:

Prof. Dr. Bernhard Roth

Prof. Dr. Martina Gerken

Tag der Promotion: 19. Januar 2022

## ABSTRACT

---

Temperature is one of the fundamental physical state variables through out most scientific and technological applications. Its influence ranges from the microscopic rate of chemical reactions to the macroscopic mechanical properties of construction materials. However, measuring temperature is not always as straight forward as it may seem, especially if a high degree of precision is required. Obstacles in the assessment of the temperature of an object can be feedback loops between instrument and measurand or a susceptibility to external fields. Optical thermometry is able to overcome many of the common challenges by offering for example non-contact measurements. There are many different optical temperature sensor concepts, ranging from fiber based sensors to thermal radiation cameras. Among those, this thesis focuses on the temperature measurement with optically active nanocrystals. This approach emerged around 2010 and can be incorporated in many applications. The first part of this thesis provides the underlying theoretical principles and physical correlations. After that, different optimization routes for both thermal and spatial resolution, respectively, are presented in the separate chapters. The results that were achieved in the context of this work were also published in [1–3]. First, a numerical model was developed to incorporate the influence of different pumping regimes in nanothermometry measurements. Through these calculations, it was shown that pumping sources either in the picosecond regime or continuous emitting lasers minimize the temperature error. Following this, the experimental characterizations of different nanocrystal systems are presented. The temperature resolution was determined for a dispersion of Pr:YLF nanocrystals and a polymer fiber doped with Er,Yb:YNaF nanocrystals. Particularly the fiber based approach helps to optimize the temperature resolution and with values of roughly 20 mK a significant upgrade to many currently used thermometers was provided. Lastly, a numerical concept to optimize the spatial resolution of measurements by utilizing stimulated emission depletion is presented. By combining this microscopy technique with doped nanocrystals it was shown that non-contact 3-D temperature measurements even below the diffraction limit are possible, while still maintaining single degree precisions in terms of temperature. This numerical work constitutes an important step towards voluminous temperature measurements with high spatial precision. Future developments that lie ahead in nanothermometry are discussed in the concluding section.

**Keywords:** nanothermometry, nanocrystals, optical metrology

## ZUSAMMENFASSUNG

---

Die Temperatur ist eine der grundlegenden physikalischen Zustandsgrößen in den meisten wissenschaftlichen und technischen Anwendungen. Ihr Einfluss reicht von der mikroskopischen Geschwindigkeit chemischer Reaktionen bis zu den makroskopischen Eigenschaften von Baumaterialien. Das präzise Messen von Temperaturen stellt allerdings oftmals noch eine große Herausforderung dar. Hindernisse bei der Bestimmung der Temperatur eines Objekts sind zum Beispiel Rückkopplungen zwischen Messgerät und Messgröße oder die Anfälligkeit des Sensors für externe Felder. Die optische Temperaturmessung ist in der Lage, viele dieser Herausforderungen zu überwinden, indem sie beispielsweise berührungslose Messung bietet. Aktuell verwendete optische Temperatursensorkonzepte sind beispielsweise faserbasierten Sensoren oder Wärmestrahlungskameras. Inhalt dieser Arbeit ist die Temperaturmessung mittels optisch aktiver Nanokristallen. Dieses Messkonzept wurde um 2010 entwickelt und bietet aufgrund der Vielfalt an aktiven Materialien eine sehr flexibel anwendbare Plattform. Der erste Teil dieser Arbeit erklärt die zugrunde liegenden theoretischen Grundlagen und physikalischen Zusammenhänge. Danach werden drei verschiedene Optimierungswege, sowohl für die thermische als auch für die räumliche Auflösung vorgestellt. Die erreichten Ergebnisse wurden darüber hinaus in Fachartikeln[1–3] veröffentlicht. Als erster Ansatz wurde ein numerisches Modell entwickelt, um den Einfluss von verschiedenen Pumpregimen bei nanothermometrischen Messungen zu berücksichtigen. Durch diese Berechnungen wurde gezeigt, dass Pumpquellen im Pikosekundenbereich oder kontinuierlich emittierende Laser den Temperaturfehler minimieren. Im Anschluss daran wurden verschiedener Nanokristall Systeme experimentell charakterisiert. Die Temperaturauflösung wurde ermittelt für dispergierte Pr:YLF-Nanokristallen und eine Polymerfaser, dotiert mit Er,Yb:YNaF-Nanokristallen. Insbesondere der faserbasierte Ansatz ermöglichte es sehr niedrige Auflösungen von etwa 20 mK zu erreichen und bietet damit eine deutliche Verbesserung zu vielen derzeit verwendeten Thermometern an. Danach wird ein numerisches Konzept zur Optimierung der Ortsauflösung von Temperaturemessungen durch Nutzung der stimulierten Emission vorgestellt. Durch die Kombination dieser Mikroskopie Technik mit dotierten Nanokristallen konnte gezeigt werden, dass berührungslose 3-D-Temperaturmessungen auch unterhalb der Beugungsgrenze möglich sind, bei gleichzeitigen einstelligen Genauigkeiten in Bezug auf die Temperatur. Im letzten Abschnitt dieser Arbeit werden weitere Ausblicke auf zukünftige Entwicklungen in der Nanothermometrie diskutiert.

**Schlagwörter:** Nanothermometrie, Nanokristalle, Optische Messtechnik

# CONTENTS

---

## I INTRODUCTION

1	DEFINITION OF TEMPERATURE	3
2	METHODS OF TEMPERATURE MEASUREMENT	7
2.1	Macroscopic Temperature sensing . . . . .	10
2.2	Nanoscale Temperature sensing . . . . .	11

## II FLUORESCENCE BASED NANOTHERMOMETRY

3	ENERGY LEVELS IN LANTHANIDE IONS	15
3.1	Theory of Level Splitting . . . . .	15
3.2	Spectral Line Shape . . . . .	17
4	INTERACTION OF LASERLIGHT WITH NANOCRYSTALS	21
4.1	Population Dynamics in Active Media . . . . .	21
4.2	Temperature Effects on the Nanoscale . . . . .	23
5	FLUORESCENCE THERMOMETRY	27
5.1	Thermal Coupling of Energy Levels . . . . .	27
5.2	Temperature Resolution . . . . .	29
5.2.1	Idealized Temperature Resolution . . . . .	29
5.2.2	Influence of Pump Regimes . . . . .	31
5.2.3	Influence of Pump Fluctuations . . . . .	34
5.3	Calibration for different Pump Regimes . . . . .	37
5.4	Spatial Resolution . . . . .	38
6	MATERIAL SELECTION	41
6.1	Spectroscopic Properties of the Active Ions . . . . .	41
6.2	Selection of the Host Crystals . . . . .	43

## III TEMPERATURE RESOLUTION IN NANOTHERMOMETRY

7	SAMPLE DESCRIPTION	49
7.1	Pr:YLF Nanodispersions . . . . .	50
7.1.1	Nanoparticle Synthesis . . . . .	50
7.1.2	Influence of the Dispersion Medium . . . . .	50
7.1.3	Emission Characteristics of Pr:YLF Nanocrystal Dispersions . . . . .	52
7.2	Er,Yb:YNaF Doped Polymer Fiber . . . . .	54
7.2.1	Er,Yb:YNaF Nanocrystals . . . . .	55
7.2.2	Manufacturing of the Fiber . . . . .	56
7.2.3	Absorption in Polymer Fibers . . . . .	57
8	MEASUREMENT SETUPS	61
8.1	Dispersion Characterization . . . . .	61
8.2	Fiber Characterization . . . . .	62
9	PR:YLF NANOTHERMOMETERS	65
9.1	Sensitivity and Temperature Resolution . . . . .	66

9.2	Continuous Wave Pumping . . . . .	67
9.2.1	Laser induced Heating Effects . . . . .	67
9.2.2	Calibration of Temperature Measurements . . . . .	70
9.3	Conclusion Pr:YLF Dispersion Measurements . . . . .	71
10	Er,Yb:YNAF DOPED POLYMERFIBER THERMOMETER	73
10.1	Sensor Calibration . . . . .	74
10.2	Sensitivity and Temperature Resolution . . . . .	78
10.3	Influence of Fiber Dimensions . . . . .	80
10.4	Influence of external Fields . . . . .	80
10.4.1	Electric Fields . . . . .	81
10.4.2	Magnetic Fields . . . . .	82
11	CONCLUSION TEMPERATURE RESOLUTION	85
<b>IV SPATIAL RESOLUTION IN NANOTHERMOMETRY</b>		
12	NUMERICAL MODEL FOR STED NANOTHERMOMETRY	89
12.1	Stimulated Emission Depletion . . . . .	89
12.2	Beam Propagation Method for Active Media . . . . .	90
12.2.1	Wide Angle Beam Propagation . . . . .	91
12.2.2	Depletion Intensity . . . . .	95
13	RESOLUTION IN STED NANOTHERMOMETRY	97
13.1	Sample Thickness and Position . . . . .	101
13.2	Absolute Temperature Resolution . . . . .	102
<b>V CONCLUSION</b>		
14	SUMMARY AND OUTLOOK	107
	BIBLIOGRAPHY	111
<b>VI APPENDIX</b>		
A	PUBLICATIONS	125
B	CURRICULUM VITAE	127



## LIST OF ABBREVIATIONS

---

Notation	Description
<i>ems</i>	emission
<i>abs</i>	absorption
STED	stimulated emission depletion
FIR	fluorescence intensity ratio
FWHM	full-width at half-maximum
OPO	optical parametric oscillators
NC	nanocrystal
NT	nanothermometer
UC	up-conversion
SNR	signal-to-noise ratio
POF	polymer optical fiber
EXC	excitation
DEP	depletion
PR	power ratio
BR	beam waist ratio

---



Part I

INTRODUCTION



## DEFINITION OF TEMPERATURE

---

There are only few quantities that play a part in the description of nearly all physical phenomena. Among those, temperature finds a special place, as it is both, easy accessible even in non-scientific contexts, and yet sometimes seems difficult to define for example in microscopic dimensions. Therefore, the first chapters aim to provide an understanding of the definition of temperature, briefly explain the historical context of their evolution, and identify the temperature regions as well as applications where lanthanide doped nanocrystals can be used.

Temperature is mostly measured in one of the three quantities Kelvin (K), degree Celsius ( $^{\circ}\text{C}$ ) or degree Fahrenheit ( $^{\circ}\text{F}$ ), of which only Kelvin and Celsius are of importance in the scientific community and consequently in this thesis. A schematic overview of these scales is given in Figure 1.1, alongside with important macroscopic measurable phase transitions in water. The reason these phase transi-

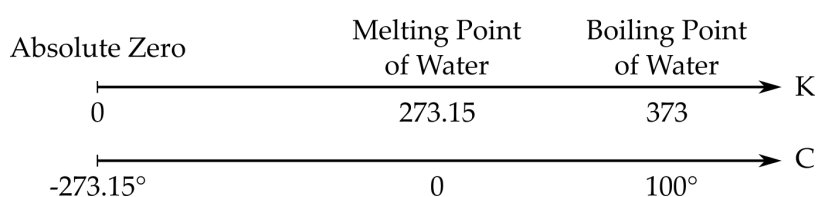


Figure 1.1: Schematic overview of two different temperature scales namely Kelvin and Celsius.

tions are included is that in early days they were used as calibration points. However, this calibration was not very precise, as for example the boiling point of water also depends on the pressure. Still, if the other influencing factors are controlled boiling water yields a robust calibration because once the corresponding temperature, of roughly  $100^{\circ}\text{C}$ , is reached any additional input energy is used for the phase transition and does not further increase the temperature. This stability in the presence of two different phases was used by Anders Celsius in the 18th century to define the Celsius scale [4], which to this day is still the most used temperature unit. Therefore throughout this thesis absolute temperatures will mostly be given in Celsius as this provides an easier understanding for readers.

The second temperature unit, the Kelvin, was first invented by and consequently, named after the Irish physicist William Thomson, the first Baron Kelvin in 1848 [5] Thomson saw the need for an absolute temperature scale with a zero as the lowest value. He calculated the corresponding Celsius value to be  $-273^{\circ}\text{C}$  and kept the proportionality

to the Celsius scale. In 1954 the Kelvin was redefined and connected to then triple-point of water, with the absolute zero being the 273.16th part of the corresponding temperature [6], to ensure continuity in the definition. This description was then used until the World Metrology Day the 20th May 2019 [6]. On this day, as result of efforts made to link the standard international (SI) units to fundamental physical constants, the definition of the Kelvin was again changed and the unit is now expressed depending on the Boltzmann constant  $k_B$ , which is mostly used to link temperature and energy. The temperature change  $\Delta T$  equal to one Kelvin is by this definition equivalent to an energy difference of one times  $k_B$ , and therefore, approximately  $1.38 \times 10^{-23}$  J [6].

Although it may be the most universal definition, the direct conversion of K to J leads to the question whether a distinctive temperature unit, besides the Celsius is even necessary in a scientific context or if knowing the energy might be sufficient. One obvious answer for that is again continuity both in experiments and engineering. However, this questions helps to understand the aforementioned problem of temperature definition in microscopic environments and the establishment of an absolute zero temperature. Considering bulk materials, the classical approach to describe the temperature of an atom at position  $i$  with mass  $m$  and velocity  $v_i$  is derived from its kinetic energy [7] by

$$\left\langle \frac{1}{2} m v_i^2 \right\rangle = \frac{3}{2} k_B T_i. \quad (1.1)$$

This approach therefore seems to assign distinct temperature values to single atoms and the feasibility of atomic level temperatures have been extensively researched. One way to address this is in the context of thermodynamics and entropy [8–10] and a correlation between the average temperature  $\langle T \rangle$  of particles in a system and its temperature  $T_0$  with

$$\langle T \rangle = T_0 \left( 1 + \frac{k_B}{c_V N} \right) \quad (1.2)$$

was derived. Besides the temperatures, the Boltzmann constant and the specific heat  $c_V$ , Equation 1.2 contains the number of particles  $N$  and as a result, the temperature uncertainty is therefore anti-proportional to  $N$  [9]. Another approach is to connect the minimum size of region with fixed temperature to the phonons inside a material [7] and this proposes the length of the mean free path of the phonons as the minimum size of regions with a fixed temperature. Both of these considerations share the aspect that microscopic temperature definition can only be applied to a certain size and statistical effects need to be considered for small regions.

Besides the spatial extensions, the maximum amplitude of temperature is also worth to look at. As mentioned before, the Kelvin scale aims to include the value of absolute zero temperature which judging

by Equation 1.1 would occur if particles were motionless. Even if the uncertainty principle prohibits such particles, because in this case both impulse and location of the particle would be exactly defined, very low temperatures have already been reached, as shown in Figure 1.2. One way to estimate the opposite site of the scale and to gain a theoretical value for the highest temperature possible is based on black body radiation. The result of this calculation is called the Planck temperature [11] and is approximately  $10^{32}$  K. The reasoning behind this, is that every body radiates light with a wavelength depending on the temperature of the body and therefore the shortest possible wavelength should correspond to highest temperature that this body possibly could have.

Even though these absolute temperature limits are interesting research topics, this work focusses on a temperature range from  $-50$  °C up to  $100$  °C since the vast majority of practical applications are found in this range. Figure 1.2 shows a small overview of different temperatures observed in nature or evaluated through experiments. This small set can already be used to identify some of the requirements temperature measurement methods need to fulfil. For instance, monitoring the temperatures inside a human body and a lithium battery may seem like a task for the same thermometer, as the expected measurement range is comparable. However, due to external constraints, such as non-toxicity for medical applications or insensitivity to electrical fields the actual used sensor can be fundamentally different. Another example can be connected to the material parameters of mercury. The highest naturally occurring temperatures on the surface of earth of  $82$  °C could easily be measured using standard mercury thermometers, whereas the counterpart falls below the melting point of mercury, as shown in Figure 1.2, and therefore cannot be accessed with this particular system.

These constraints highlight the need for suitable thermometers depending on the environment. In addition to that the spatial resolution required to obtain the desired value might even differ in a single environment, which can be illustrated by the difference between measurement of the human body temperature and the temperature inside a human cell. The following chapter therefore provides the fundamental principles of temperature measurement both in macroscopic and microscopic applications and describes where lanthanide doped nanothermometers find their place among them.

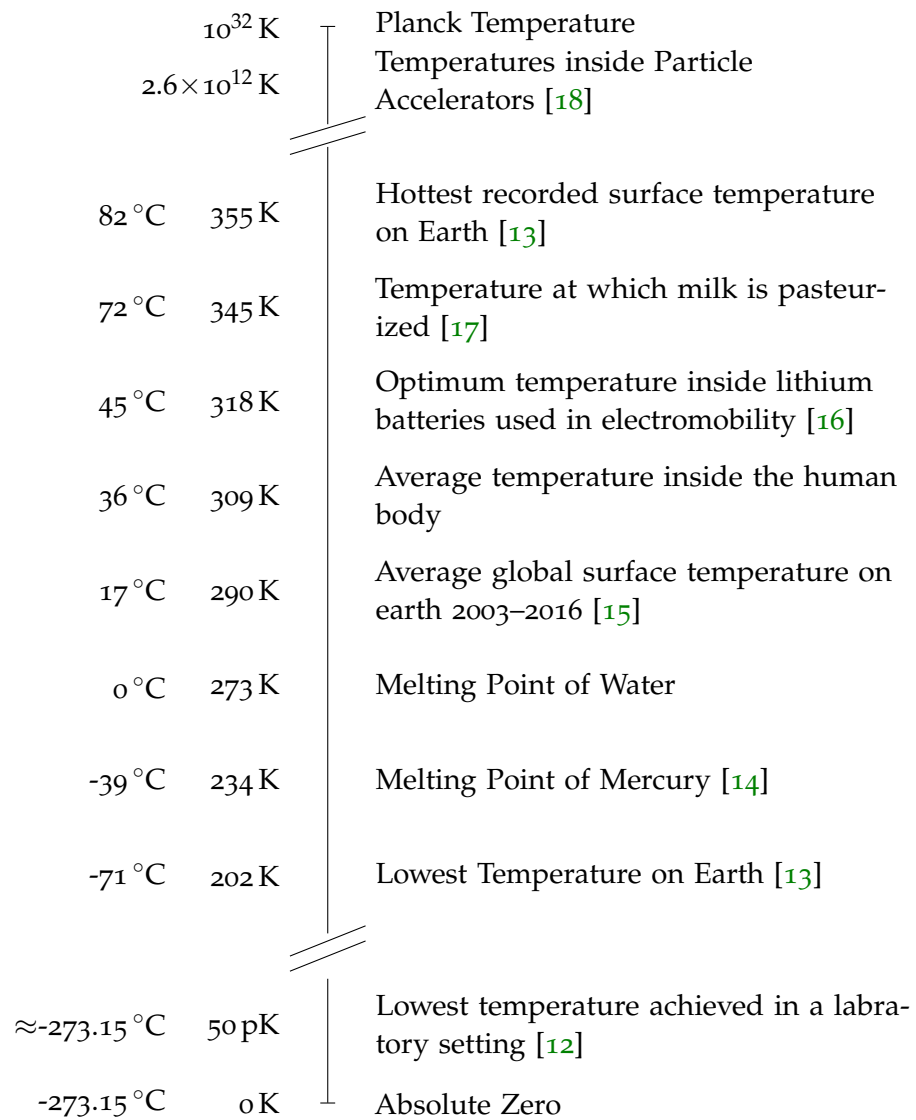


Figure 1.2: Overview of temperatures found in nature, engineering and biology.



The distinction between temperatures is one of the most fundamental measurement concepts in human history. Its origin dates back to early humans subjectively differentiating between hot and cold objects to avoid or inflict injuries, and evolved from there on alongside the progress in science for example to modern nanoscale high resolution measurements.

The first documented attempts to objectify the methods were made by Galileo and others in the early 17. century [19]. One exemplary principle was to connect tubes filled with air to a liquid reservoir. If the air tube was placed in the sun light it expanded and therefore produced bubbles inside the water. This rudimentary setup was first used not as a thermometer, but rather as a thermoscope, because of the lack of quantification of temperature changes. Nevertheless, it is regarded as one of the first steps in the long evolution of temperature measurements methods.

The next major breakthrough in thermometry can be connected to the definition of temperature scales, as mentioned in the previous section. This innovation enabled independent calibration and therefore comparable measurements. Many different physical or chemical effects were investigated in terms of temperature sensitivity since then. The sensitivity  $S$  of a quantity  $X$  to temperature changes [19]

$$S = \frac{\partial X}{\partial T}. \quad (2.1)$$

was the main inclusion requirement. However, additional criteria can be identified which can be applied in the evaluation of thermometers [19].

1. *Unambiguous Response.* A clear correlation between temperature and sensor signal is the fundamental requirement for a temperature sensing. For example, the density of water is not usable to measure temperature changes around  $4^\circ$  because of the maximum density at this temperature. In more sophisticated measurements ambiguity can be caused by the correlation of different effects, that may arise inside the thermometer through temperature changes.
2. *Sensitivity.* The temperature resolution of the sensor needs to match the relevant temperature changes inside the regarded system. For instance, the activity in biochemical processes is heavily influenced by temperature changes of a few degrees.

3. *Stability.* A basic requirement of a physical measurement is stability or reproducibility. This criterion guarantees the comparability of different measurements conducted by different persons.
4. *Measurement Range.* The thermometer chosen for a specific application needs to cover the whole range of possible occurring temperatures. Because of this, the required range depends on the utilization, and very demanding measurement tasks may justify the usage of thermometers with a very small range. Still, for evaluations of sensor concepts a wide range is always beneficial.
5. *Thermometer Size.* Thermometers always measure their own temperature and this value can only be accurately translated to the surrounding media if the thermal exchange between both is efficient enough. This efficiency of this exchange is for one is enhanced by a high surface-to-volume ratio. Besides this, the spatial resolution of the temperature also depends on the thermometer size, and therefore small thermometers are preferable in high resolution measurements.
6. *Heat Capacity.* The heat capacity is a parameter which affects the sensitivity of a thermometer, as it determines the amount of energy input necessary to increase the thermometer temperature by one degree. A minimal heat capacity is additionally desired because it minimizes the influence of the measurement on the sample.
7. *Response.* Comparable to the wide range the measurement needs to be fast enough to follow temperature changes or else only averaged values can be obtained in the case of rapidly oscillating temperatures.
8. *Robustness against external influences.* The temperature measurement needs to be independent of additional external influences, like for example electric or magnetic fields.
9. *Usable Output.* This last requirement, may again strongly depend on the application, but it is crucial that the sensor readout is easily accessible to ensure the validity of the temperature measurements.

This list can be applied to the plethora of possible thermometers with the purpose of narrowing them down to the nowadays known concepts. The most commonly used thermometers are electronic and optical sensors, and the benefits of the available methods are discussed in the following sections in terms of macroscopic and nanoscale temperature sensing.

Generally, this thesis focuses on optical temperature measurements and more specifically the utilization of optically active nanocrystals.

Optically excited lanthanide doped nanocrystals were added to variety of optical thermometers in the early 2010s [20]. This was enabled by the discovery that the temperature based emission characteristic of these nanocrystals is a reliable measurand, with a high sensitivity and easy readout possibilities. More specifically, these nanothermometers utilize spontaneous emission and the fact that the strength of this emission depends on population density of the excited energy state, which subsequently depends on the temperature.

The first step of a temperature measurement consists of a collection of the emission spectrum after optical excitation. Following this, emission lines originating from different energy levels need to be identified, and the integrated intensity is accessed either by fitting the spectrum or simply by integrating the data. The ratio of two emission intensities is calculated and by comparing this ratio to calibration data the temperature can be obtained. The temperature resolution depends on the sensitivity and the signal-to-noise ratio of the measurement. A more detailed description of the underlying physical principles can be found in Chapter 5 of this thesis.

In a more abstract way, the potential of nanothermometry and nanocrystals can also be deduced by accessing the number of publications and citations per year, as shown in Figure 2.1. Two exemplary search terms were used in *Nanothermometry* and *Lanthanide Nanocrystals*. It can be seen that the research fields correlated to this searches take off around 2010 and 2005, respectively, and both show rising behaviour but seem to reach a plateau, depicted in Figure 2.1a. The number of publications and citations of the year 2021, however is preliminary due to the access date the 26.06.2021. The citations given in

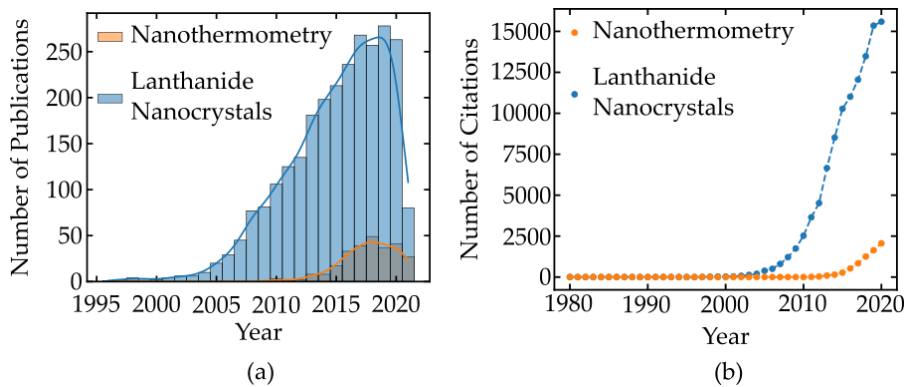


Figure 2.1: Amount of publications and citations over the years. Data collected using the search terms "Lanthanide Nanocrystals" and "Nanothermometry" inside the search engine <https://apps.webofknowledge.com/> with date of access 26.06.2021.

Figure 2.1b even appear to rise exponentially which could hint at the ongoing implementation of nanothermometry in various applications.

An overview of the most prominent research fields belonging to the publications is presented in Figure 2.2. Material science and chemistry

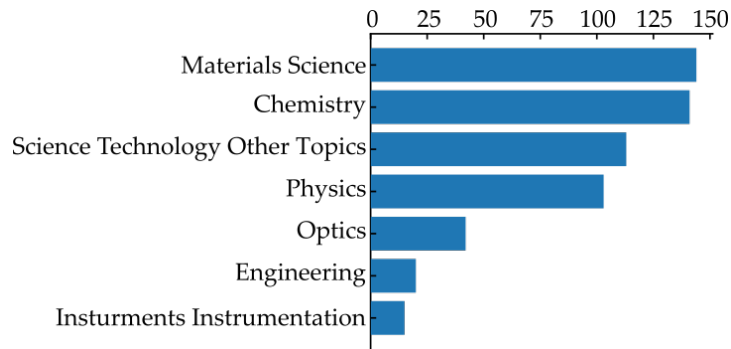


Figure 2.2: Research areas of nanothermometry publications with the possibility of overlaps. Data collected using the search terms "Lanthanide Nanocrystals" and "Nanothermometry" inside the search engine <https://apps.webofknowledge.com/> with date of access 26.06.2021.

currently are the strongest fields, as expected. However, physics, optics and engineering also contribute many publications. The distinction between these two blocks can again be correlated to an optimization of the temperature resolution. Material research and chemistry mostly address the thermal sensitivity of a nanothermometer, whereas optics and engineering are used to reduce the measurement error.

One of the first and to this day the most prominent material used as nanothermometer are Er,Yb:YNaF nanocrystals. Since then many different laser crystals have been also investigated and used in sensing applications, such as Nd:YAG [21], Pr:YLF [22] or Yb,Ho:Y<sub>2</sub>O<sub>3</sub> [23], but also other materials such as quantum dots like CdSe/ZnS [24]. The advantages and disadvantages of material classes e.g. energy level structure or resilience against external fields are discussed in detail in Chapters 3-6.

The results presented in this thesis fit into optics, physics, and engineering, as they all provide steps to optimize the signal-to-noise ratio, by adapting pumping regimes, doping of nanocrystals into solids or utilizing stimulated emission.

## 2.1 MACROSCOPIC TEMPERATURE SENSING

For a long time period, temperature sensing was mostly done by exploiting electronic effects, most commonly the thermally induced resistance change. One of the most widespread sensors is the Pt100 a platinum based sensor with a resistance of 100  $\Omega$  at 0 °C. This success story can again be explained by the aforementioned list of criteria. Platinum based sensors provide an unambiguous response and can be used over a wide temperature range from below -200 °C up to 750 °C [19]. They offer a high sensitivity and temperature resolution of  $\pm 1$  mK can be achieved in laboratory setups [19]. They are small and the signal is already measured in voltage or as current, making it is easy

to implement these sensors in different setups. But besides all these benefits, there are some drawbacks to this sensor type. First of all, this measurement is contact based, which means the sensor and sample need to share a surface. Even with little heat capacity of the sensors this always leads to a deviation in the sample temperature. Measuring inside e.g. biological specimen is difficult because of this. A second draw back comes from the susceptibility to electronic fields, which prevents the easy application of this sensor in such environments.

The other increasingly common used measurement branch is optical temperature sensing, which can be found in multiple fields [25]. Different types of optical sensors are available and already implemented in many everyday systems from motion detectors to fever thermometers. These sensors may rely on the emission of thermal infra-red (IR) radiation like IR cameras, or on temperature induced deviations of the light transmission as demonstrated with fiber thermometers. Again each of the sensor concepts has specific advantages and disadvantages. IR cameras infer temperature from a portion of black body radiation emitted by a specimen. Current devices are able to resolve temperature changes smaller than 0.1 K [26], but only if the emissivity is known. This is often not the case, especially for exotic or unknown materials. Furthermore, the specimen must have a particular size and volume which makes this method unsuitable for temperature sensing in gases. Current fiber based sensors are mostly manufactured by inscribing Bragg gratings inside optical fibers (FBG). These gratings reflect light [25] depending on the grating constant, which in terms is influenced by the fiber temperature. Optical thermometers based on FBGs offer all the benefits of optical fibers, such as spatial separation between the monitoring place and most of the other equipment. However, mechanical deformation of the fiber also influences the grating constant and with that distort the measurement.

In this thesis, a different concept was chosen for macroscopic temperature sensing and a fiber doped with nanocrystals was used. As shown in later chapters, this fiber thermometer shows an exceptionally good temperature resolution and still maintains all advantages of fiber based measurements.

## 2.2 NANOSCALE TEMPERATURE SENSING

Another way to benefit from nanocrystals is by utilizing them as nanothermometers due to their size. They can be flexibly doped inside different host media or dispersed in various solutions. This makes them a suitable candidate for temperature sensing in confined spatial regimes. There is a growing need for such temperature sensing solutions [27] following the technical evolution of microscopic devices or the medical progression in identifying interactions on protein level. A substantial effort was made to improve the spatial resolution  $\Delta x$ , rang-

ing from contact measurements similar to atomic force microscopy to contact-less fluorescence nanothermometry [27]. For example, scanning thermal microscopy is able to resolve features below 50 nm and a temperature uncertainty in the range of  $10^{-3}$  K [27]. This method is based on the atomic force microscopy, where a sensor tip is precisely positioned relative to a sample to measure e.g. surface roughness. In the case of scanning thermal microscopy, a temperature sensitive material is used as the tip enabling the high spatial resolution. Still, because it is directly applied to surface measurements and the surface quality of the sample remains a limitation of the measurement. Raman thermometry [27] is another method where the temperature is acquired by measuring the ratio of Stokes and anti-Stokes shifted responses. Raman thermometry is therefore limited by either the spot size or the sample dimension to enable high resolution.

Besides these and other mostly contact based procedures, contact-less fluorescence thermometry was also applied and by using the organic dye Rhodamine B as active material spatial resolutions of 500 nm with a thermal resolution of  $5^{\circ}$ – $10^{\circ}$  C were achieved [28]. The major restrictions of this approach were the laser induced degradation of optical dyes and the spot size of the excitation laser. While the first one could be avoided with carefully timed illumination periods [28] the latter one still remained as fundamental border. Also the low signal-to-noise ratio partly caused by the excitation restrictions due to degradation, prevents more precise temperature measurements [28]. The approach presented in this thesis via the development of a numerical model is stimulated emission depletion (STED) nanothermometry. This method potentially overcomes all of the mentioned restrictions, as nanocrystals do not show photodegradation, and with the STED based approach the spot size of the excitation beam also loses its boundary character. The numerical model was used to calculate signal-to-noise ratio values achievable with a spatial resolution below the diffraction limit, and these values were then used to calculate temperature resolutions of currently used lanthanide doped nanocrystals. The results of these calculations indicate that STED nanothermometry can be used to push the spatial resolution limit below the diffraction limit. This improvement comes on the cost of a reduced temperature resolution but even with currently available nanocrystals resolution in the range of  $\pm 1$  K should be reached and further optimization of the active materials may further push this value.

## Part II

### FLUORESCENCE BASED NANOTHERMOMETRY





## ENERGY LEVELS IN LANTHANIDE IONS

Lanthanide ions, also commonly known as rare earth elements, are often used as active material in optical applications ranging from high power Nd:YAG lasers to luminescence based sensing approaches. They are used in both macroscopic bulk crystals and nanocrystals and the reason for this is their unique electron configuration.

The rare earth elements consist of yttrium, lanthanum and the elements found in the f-block inside the sixth group of the periodic table. All rare earth ions share an electron configuration similar to xenon (Xe) [29] with additional electrons added to the 4f, 5d, or 6s shell, respectively. In the majority of cases, the optical transitions are located inside the multiplets of the 4f shell. However, in recent years applications of 4f<sup>x</sup>5d transitions also gained a lot of interest [30]. These reason that these transitions are of particular interest is the shielding of the 4f<sup>x</sup> shell by the completely filled 5s, 5d shells and partially filled 6s<sup>2</sup> shell [30, 31]. This shielding strongly reduces the coupling to external fields e.g. caused by the host medium, and therefore minimizes the distortions of spectral characteristics of the emission lines compared to a free ion.

The mechanisms that cause splitting of energy levels as well as the resulting line shape are the contents of this chapter. The explanations aim to deepen the understanding of emission measurements conducted from lanthanide doped nanocrystals, which constitute the main part of the temperature measurements discussed in this thesis.

## 3.1 THEORY OF LEVEL SPLITTING

Energy level diagrams describing a single atomic shell often consist of a multitude of energy levels. This occurrence of multiple levels due to level splitting is caused coupling effects inside the single ion and also by additional effects originating from the host medium. The splitting of energy levels is of importance to this thesis as it is the main base of the observed spectroscopic properties of active materials. Therefore, detailed looks on the underlying mechanisms are necessary to evaluate the later on presented measurement data.

The positions of the energy levels in the absence of a crystal field can be calculated by the Hamiltonian for the associated 4-f shells [29]

$$\mathcal{H} = -\frac{\hbar^2}{2m} \sum_{i=1}^N \Delta_i - \sum_{i=1}^N \frac{Z_{\text{eff}} e^2}{r_i} + \sum_{i < j}^N \frac{e^2}{r_{i,j}} + \sum_{i=1}^N \zeta(r_i) s_i l_i. \quad (3.1)$$

This equation contains the electron mass  $m$ , the number of electrons inside the 4-f shell  $N$ , the effective charge of the nucleon due to the protons inside the core  $Z_{\text{eff}}$ , the spin orbit coupling strength  $\zeta(r)$  which depends on the distance of the electron and the core  $r$  and the quantum numbers  $s$  and  $l$  for spin and angular momentum, respectively. The operators are summarised over all  $i$  electrons. In a more descriptive approach the different parts of the equation can be assigned to specific physical mechanisms and the expression is written as

$$\mathcal{H} = \mathcal{H}_{\text{KE}} + \mathcal{H}_{\text{N-4f}} + \mathcal{H}_{4f_i-4f_j} + \mathcal{H}_{\text{S-O}}. \quad (3.2)$$

Here the first part accounts for kinetic energy (KE) of the electrons, the second part describes the interaction of the electrons and the protons inside the core (N-4f). The third part includes coulomb interactions of the two electrons with the indices  $i$  and  $j$ , respectively, and lastly the spin orbit interactions (S-O) are factored in. Both, the influence of kinetic energy and the interaction of protons and electrons are negligible compared to the latter two terms of the sum. The hierarchy of the splitting mechanisms is depicted in Figure 3.1, with typical amplitudes of Coulomb and spin-orbit splitting of  $10^4 \text{ cm}^{-1}$  and  $10^3 \text{ cm}^{-1}$ , respectively.

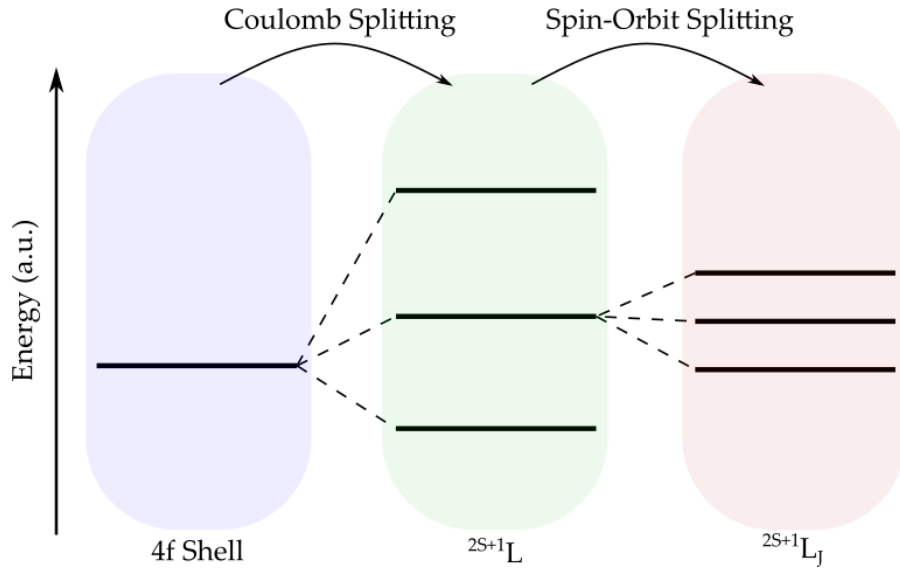


Figure 3.1: Different energy level splitting mechanisms present in a free ion.

After the different splitting mechanisms are accounted for, the actual term symbol for the energy sub-level is formed as illustrated in the following for  $\text{Er}^{3+}$ . First, the notation is introduced, which is based on the quantum numbers  $L = |\vec{L}|$  with  $\vec{L} = \sum_i \vec{l}_i$  and  $S = |\vec{S}|$  with  $\vec{S} = \sum_i \vec{s}_i$  for the total angular momentum and total spin, respectively [31]. Therefore, the notation is called LS coupling scheme [30] or Russel-

Sanders notation. The total angular momentum is  $\vec{J} = \vec{L} + \vec{S}$  and with that the energy levels are referred to as

$$^{2S+1}L_J.$$

Trivalent erbium has the electron configuration  $[\text{Xe}]^4f_{11}$ . The value of the total angular momentum for the f-shell is 3, as shown in 3.1. The maximum quantum number  $m_l$  is equal to  $2L+1$  and therefore 7, meaning 7 electrons with a parallel spin can be placed in this shell. The electron spins are aligned to ensure a maximum spin value, according to Hund's rule [32], and the total spin resulting from 11 electrons is  $7 \times 1/2 + 4 \times -1/2 = 3/2$ . The summarized angular momentum L is

L	0	1	2	3	4	5	6	7
Symbol	S	P	D	F	G	H	I	J

Table 3.1: Convention for the symbols to describe different orbitals in an atomic shell [32].

equal to 6, which corresponds to the letter I, again shown in Table 3.1. Lastly, J is formed by adding the two values and the resulting term symbol is  $^4I_{15/2}$ .

Additional external perturbations caused by the host medium can further introduce a Stark splitting in the order of  $10^2 \text{ cm}^{-1}$  and lead to a distribution of Stark levels inside the atomic shells [33]. This splitting is significantly weaker than the mechanisms presented in 3.1, but a shift of  $10^2 \text{ cm}^{-1}$  has still a major influence in fluorescence measurements, as introduced in the following chapters.

The influence of the host crystal field (CF) can again be presented by the corresponding Hamiltonian and the external potential is defined by

$$\mathcal{H}_{CF} = \sum_{i,b,k} B_q^k C_q^{(k)}(i). \quad (3.3)$$

$B$  is a parameter accounting for the crystal field,  $C$  is a tensor operator of spherical harmonics and the indices  $i, b, k$  as indices for different crystal axis and electrons [30]. In general, this crystal field influences the level degeneracy and causes a shift of the emission to lower energies, also called the nephelauxetic effect [34]. The amount of non vanishing terms in Equation 3.3 decreases for higher degrees of host crystal symmetry.

### 3.2 SPECTRAL LINE SHAPE

The line shape of an emission line is mainly determined by the energetic distribution of Stark levels in the upper emission level. Even though in practical measurements the actual number of Stark levels and their energy characteristics is not always accessible, due to a lack

of spectral resolution, a general knowledge of the possible splitting effects helps to interpret the emission spectra, as shown in Figure 3.2. Moreover, it helps to assure a correct assignment of emission lines to energy levels as needed to build the emission ratio used in fluorescence based temperature measurements. As seen in the Figure 3.2,

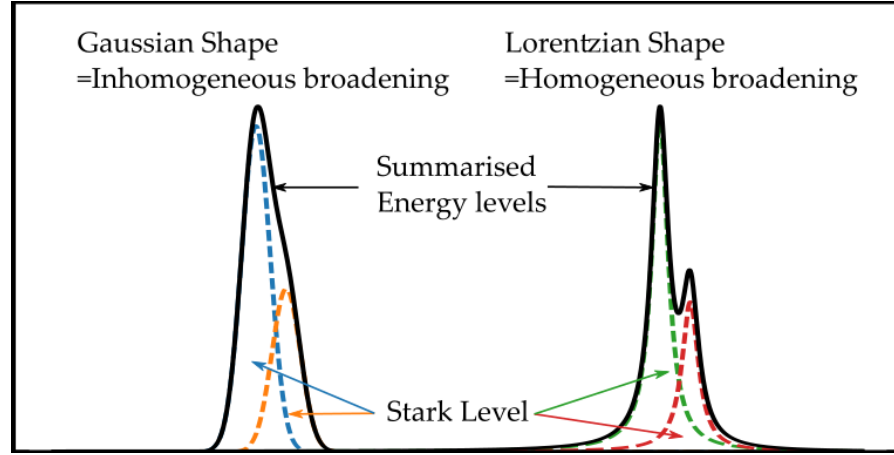


Figure 3.2: Spectral line shape of the emission from energy levels caused by the Stark splitting. Both cases of line broadening are shown by their characteristic shape, the Gaussian and Lorentzian distributions.

the measured spectral shape of the emission originating from a single energy level is formed by a superposition of the emission lines of the single Stark levels. Mathematically the shape of the emission lines can then be approximated by summarized Gaussian or Lorentzian functions, that are defined by

$$G(x, \mu, \sigma, A) = A \exp\left(-\frac{(x - \mu)^2}{2\sigma^2}\right) \quad (3.4)$$

and

$$L(x, \mu, \sigma, A) = A \left( \frac{\sigma^2}{(x - \mu)^2 + \sigma^2} \right), \quad (3.5)$$

respectively [35]. The parameters in these equations are the transversal  $x$  coordinate, the center value  $\mu$ , the width  $\sigma$  and the amplitude  $A$ . The two different functions are used to account for the two different mechanisms that cause line broadening, with the Gaussian distribution correlating to inhomogeneous broadening and the Lorentzian distribution for the case of homogeneous broadening. These mechanisms are for example interactions of the excited ion with phonons in the host crystal or emission shifts due to the Doppler effect [35]. The sum of all mechanisms defines whether inhomogeneous and homogeneous broadening is present. If all particles in a sample are subjected to the identical line broadening mechanisms the resulting line shape is homogeneous broadened. If different effects are present than inhomogeneous broadening occurs. Purely homogeneous line

broadening therefore only appears for isolated ions, because else small difference between even two emitting ions can always be expected. In the case of nanocrystals, this differences are e.g. caused by quenching to the surrounding material which strongly varies depending on the position of the ion inside the crystal [36]. Therefore, in nanothermometry measurements inhomogeneous broadening is expected to be dominant.

However, even in this case an overlap of Gaussian and Lorentzian can be present and different types of weighted Voigt function are then often used to approximate the spectral shape of an emission line. One specific type, the Pseudo-Voigt function [37], consists of a linear combination of a Gaussian function and a Lorentzian function, with an added weighting factor  $\nu$  and is therefore equal to

$$V(x, \mu, \sigma, A) = \nu L(x, \mu, \sigma, A) + (1 - \nu)G(x, \mu, \sigma, A). \quad (3.6)$$

This function allows for a flexible fitting of emission data and with that an allocation of emission peaks to different energy levels. Therefore, all fitting routines presented in this thesis were carried out using the Pseudo-Voigt function.



## INTERACTION OF LASERLIGHT WITH NANOCRYSTALS

Laserlight can interact with matter in various ways [38] and this chapter gives an overview for the ones most relevant in the context of nanothermometry being, absorption of photons and spontaneous or stimulated emission of photons [39]. Especially the ability to spontaneously emit photons is the basis of the measurement principle presented in this thesis, which will be discussed in Chapter 5.

All three mechanisms depend on population densities of the involved energy levels.

The first section is dedicated to the derivation of a set of rate equations to calculate the population densities and to estimate the corresponding changes in photon density by either absorption or emission. The second section provides a survey of temperature effects on the nanoscale and mainly deals with the role of laser induced heating and its influence on the temperature readout in emission based temperature measurements.

### 4.1 POPULATION DYNAMICS IN ACTIVE MEDIA

For this thesis the three dominant interaction mechanisms of light and matter are absorption, spontaneous emission, and stimulated emission. A schematic representation of the related electronic transitions is shown in Figure 4.1. As depicted, photons can be absorbed by electrons

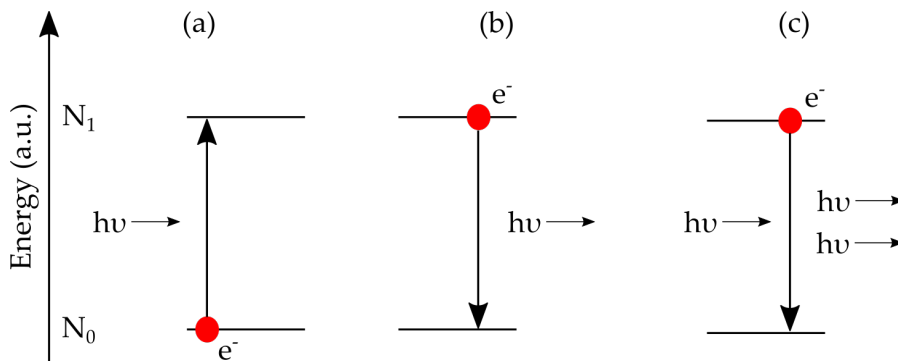


Figure 4.1: Interaction of light and matter as shown by the transitions between electron energy levels with the population densities  $N_0$  and  $N_1$  caused by (a) absorption, (b) spontaneous emission and (c) stimulated emission.

which results in a transition of the electron to a high energy level. The energy difference between both energy levels has to be equivalent to

the energy of the absorbed photon  $h\nu$ . The time dependent rate of this transition in population densities  $N_0$  and  $N_1$  is described by

$$\frac{dN_1}{dt} = n\sigma_{\text{abs}}N_0 \quad (4.1)$$

with  $n$  as the number of incident photons per area and time [35]. The relation of incident photons and electrons is weighted with the absorption cross section  $\sigma_{\text{abs}}$ , which is a measure of the transition probability [35].

The absorption process leaves the electron in an excited state. These electron states are mostly metastable and have a statistical lifetime  $\tau$ . If the electron transitions back into the ground state, another photon with the energy  $h\nu$  is emitted undirected. This emission process is also known as spontaneous emission or fluorescence and its rate is given by

$$\frac{dN_1}{dt} = -\frac{1}{\tau}N_1 = A_{10}N_1. \quad (4.2)$$

The Einstein coefficient  $A = 1/\tau$  is also be used to describe the rate of this process instead of  $\tau$  [35].

The third process remaining from Figure 4.1 is the stimulated emission. In this case an incident photon with energy  $h\nu$  stimulates the electronic transition between the upper and lower laser level, coupled with the emission of another photon. One peculiarity compared to spontaneous emission is that both photons share the same polarization and are emitted in the same direction. Similar to the absorption the probability of this process is modelled by a cross section  $\sigma_{\text{ems}}$  and the variation of  $N_1$  is given by [35]

$$\frac{dN_1}{dt} = -\sigma_{\text{ems}}nN_1. \quad (4.3)$$

A complete set of laser rate equations, used to calculate the population density of an active material, is then formed by combining the different production and annihilation operators. An exemplary set of these equations for a two level laser is

$$\begin{aligned} \frac{dN_1}{dt} &= \sigma_{\text{abs}}nN_0 - \frac{1}{\tau}N_1 - \sigma_{\text{ems}}nN_1 \\ \frac{dN_0}{dt} &= -\sigma_{\text{abs}}nN_0 + \frac{1}{\tau}N_1 + \sigma_{\text{ems}}nN_1 \\ N_{\text{total}} &= N_1 + N_0 \end{aligned} \quad (4.4)$$

The third equation in this set is the boundary condition for the total electron density in the system  $N_{\text{total}} = N_1 + N_0$ .

The laser power travelling along the axis  $z$  inside the system is calculated using the population densities and material parameters by

$$\begin{aligned} \frac{\partial P(\lambda)}{\partial z} &= +\sigma_{\text{ems}}(\lambda)N_1P(\lambda, z) \\ &\quad -\sigma_{\text{abs}}(\lambda)N_0P(\lambda, z) \\ &\quad +\frac{N_1}{\tau}\frac{hc}{\nu}\epsilon_{\text{ems,Sp}}(\lambda)\beta A. \end{aligned} \quad (4.5)$$



Equation 4.5 again consists of different parts accounting for stimulated emission, absorption and spontaneous emission. The additional parameters are  $\epsilon_{\text{ems,Sp}}(\lambda)$  as the probability for emission of wavelength  $\lambda$  and  $\beta$ , which denotes the solid angle of fluorescence that is considered [40]. These coupled equations are solved either time dependent or in the steady-state, both variants shown in later sections of this thesis.

#### 4.2 TEMPERATURE EFFECTS ON THE NANOSCALE

Another possibility of a transition between an excited state and the ground state is a non-radiative transitions. Through this transition, energy deposited inside the system is converted to heat instead of another photon via interactions with phonons. The following section provides an insight into the fundamentals of laser induced heating effects. For simplicity, radiative transfers are neglected and all absorption is assumed to contribute to heating. This could be included by inserting the quantum defect, which is the difference between the energy of the absorbed photon and the emitted photon, if needed.

The topic of laser induced heating in nano-dispersions has mostly been researched in terms of metallic nanoparticles e.g. [41–44]. However, the basic principles of heat generation and transport can be transferred to other nanocrystals classes, as only the degree of absorption and material parameters change. The main equation necessary to understand the occurring changes of temperature  $T$  is the heat equation [44]

$$\rho_0 c_0 \frac{\partial T}{\partial t} = \nabla(k_0(T)\nabla T) + q_0 \quad (4.6)$$

which includes the density  $\rho_0$ , heat capacity  $c_0$  and thermal conductivity  $k_0$  of the material, and the source term for internal heat generation  $q_0$ .

The energy balance model is one approach to use these equations to access the heating of nanocrystals [42]. In this model, the rate of temperature change of the particle is set equal to the difference of the heating rate  $Q_l$  and the heat dissipation rate  $Q_{\text{diss}}$ , such as

$$m_p c_p \frac{\partial T}{\partial t} = Q_l - Q_{\text{diss}} \quad (4.7)$$

The heating rate depends on the absorption coefficient  $\alpha = \sigma_{\text{abs}}N$  of the nanocrystal and the incident laser intensity  $I$ , which is defined similar to the previous section, with

$$Q_l = I\sigma_{\text{abs}}N. \quad (4.8)$$

The heat dissipation can be calculated from the temperature gradient  $T-T_0$  between particle and surrounding medium, a projected surface  $S$  and the heat transfer coefficient  $h$

$$Q_{\text{diss}} = hS(T - T_0). \quad (4.9)$$

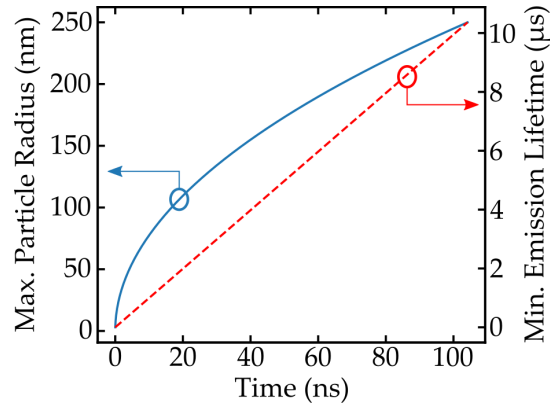


Figure 4.2: The maximum particle radius for local equilibrium temperature to form depending on the time on the left y-axis. Emission lifetime resulting in statistically only 1% of photons the emitted depending on the time on the right y-axis.

The temperature inside the nanocrystal is assumed to be homogeneous for this calculation. This is a reasonable assumption for nanothermometry measurements because the spatial resolution of the measurement is much larger to the radius  $r_0$  of a single nanocrystal.

Inserting 4.8 and 4.9 into 4.6 yields the new equation

$$\frac{\partial T}{\partial t} = \frac{I\sigma_{\text{abs}}N}{m_p C_p} - \frac{hS(T - T_0)}{m_p C_p} \quad (4.10)$$

again with two rates for heating and cooling as the both parts of the equation, respectively.

The consequence for nanothermometry can be easily explained for the case of a measurement with short pulsed excitation. The temperature difference between nanocrystal and surrounding media before the measurement is negligible since both materials are assumed to be in a steady state. The heating rate can then be attributed to the absorption of the incident laser radiation inside the nanocrystal. If a delta pulse is assumed as heating source, the first term of Equation 4.10 vanishes and the duration  $t_p$  until nanocrystal and surrounding are in an equilibrium again is reached after this temperature disruption is given by [44] with

$$t_p \approx \frac{r_0^2}{4\chi}. \quad (4.11)$$

In this equation  $\chi$  is the thermal diffusivity parameter, and is determined by the thermal diffusivity of the surrounding media. Besides this the time necessary for heat exchange is quadratically dependent on the particle size represented by the radius  $r_0$ .

In nanothermometry it is desired that the intensity ratio of two emission lines correlates directly to the temperature of the host media and not only the particle. Assuming only the particle is heated by the pump pulse, it is therefore imminent to assure that that most of the

photons are emitted after a local temperature equilibrium between nanocrystal and surrounding is again reached. Figure 4.2 shows the relation between the particle radius and the time until such an equilibrium is reached, if a delta pulse is taken as the heating source. The correlation between the two parameters is given by Equation 4.2. Also depicted in this figure is the emission lifetime  $\tau_{\text{ems}}$  that results in statistically 1% of emission at any given duration.

These depicted values show for example that emission lifetimes in the microsecond range are needed to make sure that most of the emission occurs after the local temperature is in a steady state. This is minimized the effect of the time dependent particle heating on the temperature measurement. This lifetime requirement is met for most rare earth ions [45], again showing their potential for nanothermometer applications. Other optically active materials such as dyes inhibit much shorter lifetimes [40] meaning that potential temperature measurements need to be more cautious of the involved time scales.

This relation can also be useful to make a first assumption in terms of spatial resolution. If  $\tau_p \ll \tau_{\text{ems}}$  as desired, the resulting emission ratio corresponds to the local temperature inside the host medium. If the particle is then moving inside a medium with a strong temperature gradient, this also leads to a difference in the temperature readout. In other words, for very long emission times or fast moving particles the spatial resolution is not only limited by the excitation function but also by the particle movement. Additionally, potential measurement errors may arise due to varying temperatures inside the host medium. One way to overcome this is the suppression of emission originating from nanocrystals outside a desired region, which can be achieved by stimulated emission depletion, as discussed in Chapter 12.



Building up on the fundamental physics of energy levels and light matter interactions described in the previous chapters, the next sections shifts the focus to a more detailed description of the thermometry approach. The thermal coupling caused by phonon relaxations is described, as this is the mechanism responsible for the correlation of temperature and emission intensity. After that the definitions for the sensitivity and the temperature resolution are derived and the influence of the energy gap between the emitting levels is discussed. The last part of this chapter constitutes of a detailed discussion of measurement errors caused by shift in the pump regime. The outlined numerical model, as well as the presented data, was developed and calculated as part of this thesis and are published in [3].

### 5.1 THERMAL COUPLING OF ENERGY LEVELS

The temperature of a collective of particles is a measure for the mean energy, as described in the introduction. Considering that the population of electronic states is also an indicator of the particle energy, a direct connection between temperature and population of electronic energy levels seems apparent. The relation of the population densities of two energy levels  $N_1$  and  $N_2$  obey the Boltzmann law and are described by [20]

$$\frac{N_2}{N_1} \propto A \exp\left(-\frac{\Delta E}{k_B T}\right). \quad (5.1)$$

In this equation  $A$  is a constant used to incorporated physical constants such as e.g. the level degeneracy,  $\Delta E$  is the energy gap between the two energy levels and  $k_B$  is the Boltzmann constant, respectively. Based on Equation 5.1 it can be seen that the relative thermal population depends on the energy gap and the temperature. This basic relation is further illustrated in Figure 5.1. For this depiction, arbitrary energy levels with an energy defined by the Rydberg formula  $E=hcR_\infty Z_2^2/n_2^2$ [46] were used. A more detailed discussion of the Rydberg formula, its parameters and its usage in the description of energy level distributions can be found in [46]. Figure 5.1b also gives an overview of different energy levels defined by their quantum number, which again shows the exponential character of the relative population and the shift with temperature.

The thermalization rate mostly depends on the relation of the energy gap between the energy levels and the phonon energy of the host material, as it is a phonon based process [47]. In many crystals, the

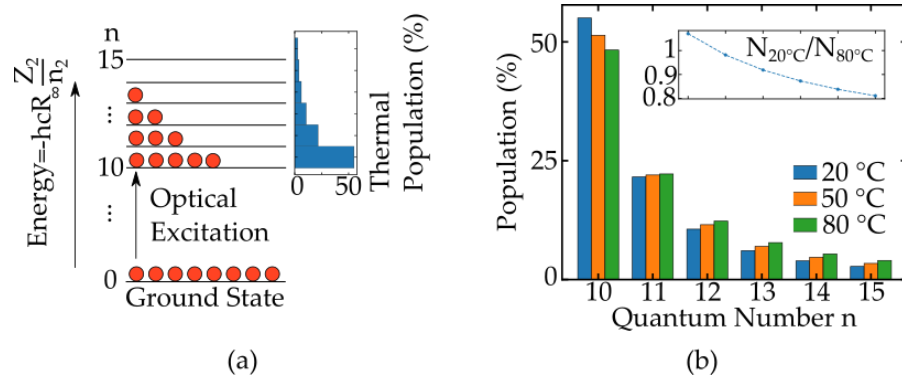


Figure 5.1: Exemplary depiction of the thermal population distribution of arbitrary energy levels ( $n=10\dots15$ ) after optical excitation from the ground state in (a). Depicted in (b) is the percentage of populations of energy levels for different temperatures.

energy gap between two energy levels, e.g.  $10^4 \text{ cm}^{-1}$  in the case of the Coulomb splitting, is far greater than the phonon energy. Therefore multiple phonons are needed to bridge this gap. The transfer rate heavily depends on the number  $p$  of phonons and the relation between lower and higher order processes given by [48]

$$\frac{w(p)}{w(p-1)} = \epsilon. \quad (5.2)$$

In this equation the electron-phonon coupling coefficient  $\epsilon$  is generally much smaller than 1 [48], and the assumption that the lowest order dominates is therefore reasonable. Apart from  $p$  the transfer rate depends on the occupation density of the phonon states that follows the Bose-Einstein [48] occupation. The maximum phonon energy  $h\nu_{max}$  has an average occupation  $\bar{n}$  of

$$\bar{n}(\nu_{max}) = \left[ \exp\left(\frac{h\nu_{max}}{k_B T}\right) - 1 \right]^{-1} \quad (5.3)$$

Only the highest phonon energy is considered in this approach, because it corresponds to the lowest order of the transfer process. Applying this, the transfer rate is expressed as a function of temperature by

$$W^p(T) = W_0^p (\bar{n}(\nu) + 1)^p \quad (5.4)$$

with  $W_0$  being the rate at low temperatures [49]. The temperature dependence of higher order phonon transitions is shown in Figure 5.2 and as expected the relative increase due to higher temperatures is stronger for the higher orders. High temperatures therefore potentially allow for a wider range of host crystals due to the enhanced transfer rate, as depicted in Figure 5.2. This behaviour can also be used to estimate the order of phonon processes in a given system.

However, most laser crystals have phonon energies between  $100 \text{ cm}^{-1}$  and  $1000 \text{ cm}^{-1}$  like for example YAG ( $700 \text{ cm}^{-1}$  [48]), YNaF ( $360 \text{ cm}^{-1}$

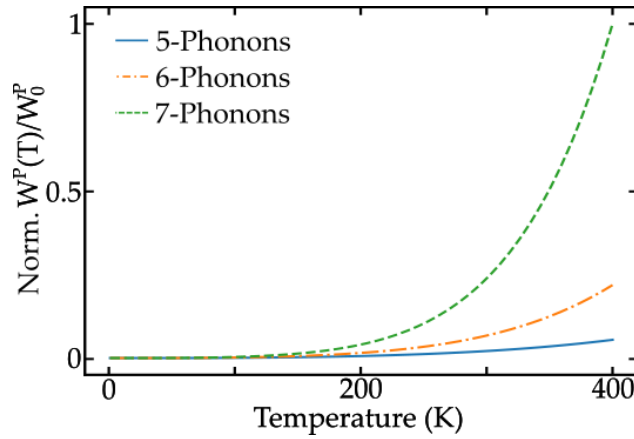


Figure 5.2: Temperature dependency of different orders of phonon transitions

[50]), or YLF ( $560 \text{ cm}^{-1}$  [51]), and therefore, the thermalization of energy levels with  $\Delta E \approx 10^3 \text{ cm}^{-1}$  happens via low order phonon processes is therefore assumed instantaneous compared to the fluorescence lifetime [47].

## 5.2 TEMPERATURE RESOLUTION

In idealized systems the temperature measurement depends on the ability to measure emission from different energy levels and the energy gap between the two emission levels. The first part of this section describes this idealized formalism and derives the basic formulas used in nanothermometry. Following this, the second sections provides a translation to real measurements by including the influence of the populations of lower energy levels and a variation of the pump regime.

### 5.2.1 Idealized Temperature Resolution

Among the aforementioned mechanisms of light-matter interaction fluorescence thermometry utilizes the spontaneous emission and more precise the intensity ratio (FIR) of different emission lines [20]. Consequently, the performance of the thermometer mostly depends on population densities  $N_2$  and  $N_1$  of thermally coupled excited electron states, as explained in chapter 4.1. The FIR originating from these energy levels is temperature dependent as given in Equation 5.1 and defined by

$$\text{FIR} = \frac{I_2}{I_1} \propto \frac{N_2}{N_1} = A \exp\left(-\frac{\Delta E}{k_B T}\right). \quad (5.5)$$

Variation of the temperature affects the change of the FIR with an amplitude depending on the energy gap and also the initial value. A schematic representation is shown in Figure 5.3. The dependence of FIR on temperature defined by equation 5.5 is exponential but can be linearly approximated for simplified measurements by apply-

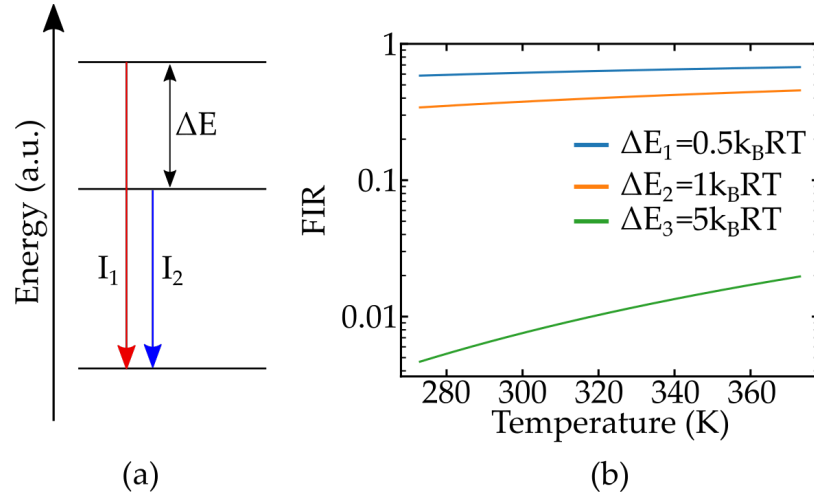


Figure 5.3: Schematic view on the influence of the energy gap  $\Delta E$  on the FIR. The shown  $\Delta E$  values correspond to multiples of the Boltzmann factor at room temperature  $RT$  of 293 K.

ing a Taylor series expansion. The approximated function  $P$  at room temperature  $T_R$  is

$$\begin{aligned} P(T) &= \text{FIR}(T_R) + \text{FIR}'(T_R)(T - T_R) \\ &= \exp\left(\frac{-\Delta E}{k_B T_R}\right) + \frac{\Delta E}{k_B T_R^2}(T - T_R) \end{aligned} \quad (5.6)$$

and the approximation error is calculated from the difference between  $P(T)$  and  $\text{FIR}(T)$ . This error can then be used to estimate a feasible temperature region in which the correlation between sensor read-out and temperature is assumed to be linear. Again, it is worth noting that this linear approximation only simplifies the measurement and the actual unambiguous FIR response to temperature changes exceeds this region. A schematic representation of this linearity approach and the resulting relative error is given in Figure 5.4. The sensitivity of the thermometer is derived from the temperature dependence of the FIR and the FIR at a given temperature. A distinction between absolute  $S_a$  and relative  $S_r$  sensitivity can be made according to [52] with

$$\begin{aligned} S_a &= \frac{d\text{FIR}}{dT} = \frac{\Delta E}{k_B T^2} \\ S_r &= \frac{1}{\text{FIR}} \frac{d\text{FIR}}{dT} \end{aligned} \quad (5.7)$$

and typical values range around 1–3 %/K.

Rearranging the equation for  $S_r$  helps to identify the achievable temperature resolution as

$$\Delta T = S_r^{-1} \text{FIR}^{-1} \Delta \text{FIR}. \quad (5.8)$$

This examination shows the influence of the signal-to-noise ratio expressed by  $\Delta \text{FIR}$  on the sensor performance. Since the signal-to-noise



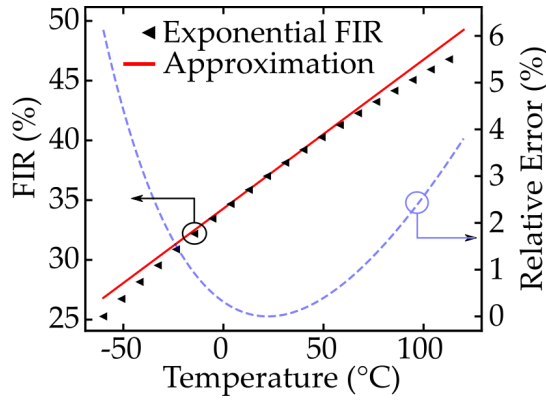


Figure 5.4: Linear approximation of the evolution of the FIR and the relative error resulting from the deviation of this approximation from the exponential FIR values.

ratio depends on two measurement uncertainties for both emission intensities  $I_1$  and  $I_2$ , Gaussian error propagation is applied and the value of  $\Delta\text{FIR}$  follows from

$$\Delta\text{FIR} = \left| \frac{\partial\text{FIR}}{\partial I_2} \right| \Delta I_2 + \left| \frac{\partial\text{FIR}}{\partial I_1} \right| \Delta I_1 = \frac{\Delta I_2}{I_1} + \frac{I_2}{I_1^2} \Delta I_1. \quad (5.9)$$

Basing on Equation 5.8 different approaches to minimize  $\Delta T$  can be identified. The most intuitive would be an improvement of the signal-to-noise ratio by reducing the noise or find ways to increase the signal e.g. through more sophisticated fitting routines.

Optimizing the sensitivity also results in an enhanced  $\Delta T$ , but again a differentiation between  $S_a$  and  $S_r$  has to be made [52]. Exclusively increasing  $S_a$  by tuning the value of  $\Delta E$  may not lead to the desired effects as the absolute value of FIR is also factored in this equation. Therefore, in terms of a high temperature resolution optimization should rather be aimed at improving  $S_r$ .

### 5.2.2 Influence of Pump Regimes

The population densities of the lower energy levels are another important parameters for emission measurements, as the resulting re-absorption can affect the measured emission intensities. This effect is often neglected in practical applications, even though this may cause measurement errors. Therefore numerical model was developed to estimate the measurement deviations arising from re-absorption, and the results were published in [3].

The role of this effect can be illustrated by looking at the energy level diagram of two currently used active ions, Erbium ( $\text{Er}^{3+}$ ) [20] and Praseodymium ( $\text{Pr}^{3+}$ ) [22], as depicted in Figure 5.5a. The combination of transitions used in  $\text{Er}^{3+}$  nanothermometry are  ${}^4\text{H}_{11/2} \rightarrow {}^4\text{I}_{15/2}$  centered around 525 nm with  ${}^4\text{S}_{3/2} \rightarrow {}^4\text{I}_{15/2}$  centered around 545 nm,

therefore including only one lower energy level. In contrast, using  $\text{Pr}^{3+}$  for nanothermometry enables different transitions e.g.  ${}^3\text{P}_1 \rightarrow {}^3\text{H}_5$  at 522 nm and  ${}^3\text{P}_0 \rightarrow {}^3\text{H}_6$  at 639 nm with varying lower energy levels. The same distinction applies to other active ions such as  $\text{Nd}^{3+}$  [21] or  $\text{Ho}^{3+}$  [23], respectively. The schematic 3- and 4-level laser diagrams provide a more general view and are shown in Figure 5.5b. Since the re-absorption depends on the population of the lower level different re-absorption values can be expected for the different transitions e.g. in  $\text{Pr}^{3+}$  with the consequence of temperature measurement errors. On the other hand one benefit of using varying lower energy levels is the spectral separation of the emission lines independent of the energy gap of the upper levels, therefore adding flexibility to measurements.

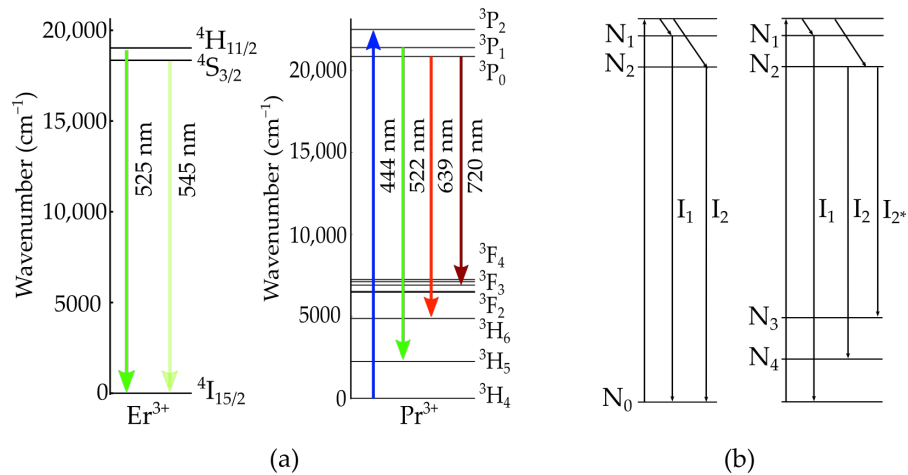


Figure 5.5: Energy levels of trivalent ions  $\text{Er}^{3+}$  and  $\text{Pr}^{3+}$  ions used in nanothermometry [20, 22] with the optical transitions for excitation and emission in (a) and the corresponding general 3-level and 4-level laser schemes in (b).

Currently the sensitivity of nanothermometers is characterized either under pulsed excitation [22, 23] or continuous excitation [1, 21]. This raises the question whether these pump regimes are interchangeable or if the pump regime has further influences on measurement errors besides the signal-to-noise ratio. Additionally, calibration data acquired with either of these systems may not be accurate for the other regime, even for the same active ion. Re-absorption of emission could prevent this transfer because the population densities of the absorbing energy levels differ between instantaneous and steady state conditions. Generally, re-absorption is a well-known phenomenon for example causing a reduced efficiency of  $\text{Pr}:\text{YLF}$  lasers emitting in the orange spectral range [53]. Fitting the thermal evolution of the FIR in  $\text{Pr}^{3+}:\text{YF}_3$  for the same upper levels but different lower laser levels also may yield different  $\Delta E$  values [54], which could also be attributed to re-absorption differences.

Consequently, population of lower energy levels has to be considered as origin of FIR deviations even in the absence of temperature variations, therefore, causing measurement errors. This issue can be addressed by utilizing time dependent laser rate equations. Figure 5.6 illustrates the relation of the populations of two lower energy levels depending on the relative strength of the spontaneous emissions, which is determined by their emission cross sections  $\sigma_{\text{ems},2}$  and  $\sigma_{\text{ems},2^*}$ , and the lifetimes of the levels  $\tau_3$  and  $\tau_4$ , respectively. In this figure the population relation is depicted depending on the ratio of the lifetimes  $\tau_{\text{rat}} = \tau_3/\tau_4$  for a constant ratio in (a) and a varying ratio in (b). Different calibration regimes for nanothermometry can be defined

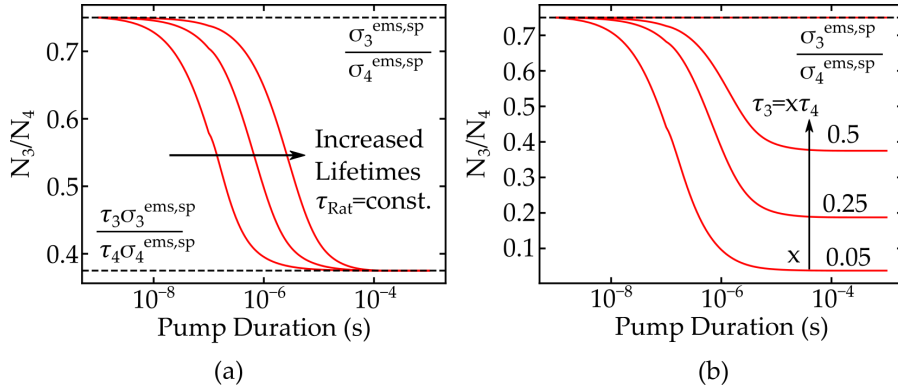


Figure 5.6: Relative relations of the population densities  $N_3$  and  $N_4$  of lower laser levels, as defined in Figure 5.5, depending on the pump duration. Depicted in (a) are relations for a constant ratio  $\tau_{\text{Rat}}$  of the emission lifetimes and in (b) for different ratios

depending on the pump duration and fluorescence lifetime, as a result of this.

Judging purely by the depicted populations, two operating regimes with stable relations can be identified, as seen in Figure 5.7. The first window corresponds to very short excitation times and the population relation is defined only by the relation of the emission cross sections. If the excitation duration reaches the range of a few micro seconds the steady state regime starts to build up and additionally  $\tau_3$  and  $\tau_4$  also need to be factored in, as given in Figure 5.6. These results generally apply to both laser schemes shown in Figure 5.5, however for materials like  $\text{Er}^{3+}$  the lower energy level is the same and with that the values for lifetime and cross sections are identical.

The deviation of the FIR following this, further depends on the absorption cross section  $\sigma_{\text{abs}}$ . This cross section  $\sigma_{\text{abs}}$  can be calculated using the McCumber relation [55] from  $\sigma_{\text{ems}}$ ,  $Z_1$  and  $Z_2$  as parameters for the degeneracy of the Stark levels in the two involved energy levels 1 and 2, and the energy distance  $E_0$  between the lowest energy levels of both manifolds 1 and 2 [56]. The relation is defined as follows

$$\sigma_{\text{ems}}(\nu) \simeq \sigma_{\text{abs}} \frac{Z_1}{Z_2} \exp \left[ \left( \frac{E_0 - h\nu}{k_B T} \right) \right]. \quad (5.10)$$

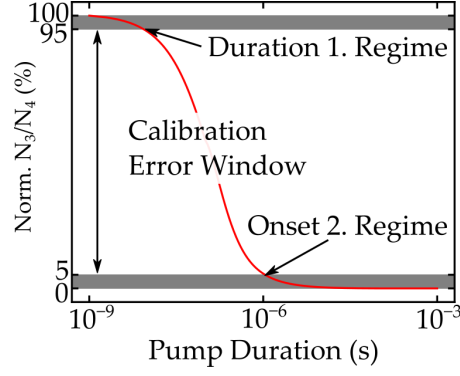


Figure 5.7: Exemplary depiction of the different calibration regimes caused by changes in energy level populations.

The material parameters used in the following calculations were taken from  $\text{Pr}^{3+}$  nanothermometer. This formalism gives a proportionality between absorption and emission cross section with an additional factor for the Stark level splitting and population [57]. It is therefore used to gain an estimation of the remaining fluorescence  $P(z)$  after absorption via Lambert-Beers Law. Applying the approximation for a short interaction length  $z$  the yields

$$P(z) = P_0 \exp(-N\sigma_{\text{abs}}z) \approx P_0(1 - N\sigma_{\text{abs}}z). \quad (5.11)$$

Based on these relations and Equation 5.5, a factor  $C$  to convert the instantaneous  $\text{FIR}^{\text{inst}}$  to the steady state  $\text{FIR}^{\text{too}}$  is defined

$$\text{FIR}^{\text{too}} = \text{FIR}^{\text{inst}}C \quad (5.12)$$

$$= \text{FIR}^{\text{inst}} \frac{1 - \sigma_{\text{abs},1}N_1z}{1 - \sigma_{\text{abs},2}N_2z} \quad (5.13)$$

This formalism can be used to recalibrate FIR measurements depending on the pump regime.

### 5.2.3 Influence of Pump Fluctuations

The pump rate heavily influences the population density of energy levels, as mentioned in the previous sections. A detailed look at the influence of fluctuations in this rate helps to understand the temperature resolution achievable with a specific measurement configuration.

Pulsed excitation sources operating in the nanosecond regime are frequently used in nanothermometry [22, 23], and typical pump sources, such as OPOs or q-switched lasers, are prone to power and energy fluctuations, respectively. As the value of  $\sigma_{\text{abs}}$  is wavelength dependent, fluctuations of the emission wavelength can also be treated as energy fluctuations, as can be seen from Equation 5.11. Furthermore, the pulse duration may also fluctuate resulting in another source of measurement errors. The temporal evolution of population densities

and from that the onset of fluorescence is simulated to characterize these effects and to gain the amplitude of  $\Delta\text{FIR}$ . The corresponding

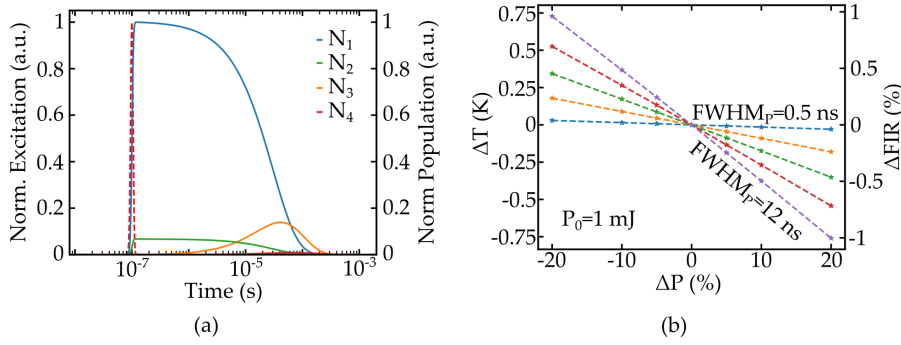


Figure 5.8: Temporal evolution of population density calculated for an approximated  $\text{Pr}^{3+}$  doped system (a) and the consequence on FIR measurements in dependency of pump energy fluctuations.

temperature error  $\Delta T$  caused by the fluctuations can be accessed by using the specifications of Pr:YLF nanothermometers with  $\text{FIR}_0 \approx 1.2$  and  $S \approx 1.1\%/\text{K}$  [22] through Equation 5.8. The lifetimes of energy levels for a given dopant also depends on the host material. Unfortunately, the lifetimes of Pr:YLF crystals were not available in the literature, so the lifetimes of the  ${}^3\text{F}_3$  or  ${}^3\text{F}_4$  levels in Pr:LaCl<sub>3</sub> reported to be  $58\ \mu\text{s}$  [58] were used for the calculations. However, the proposed formalism is still valid for different lifetimes, and the calculations can easily be adapted after measuring the transition rates inside the desired material.

The results are shown in Figures 5.8 and Figures 5.9. As seen in

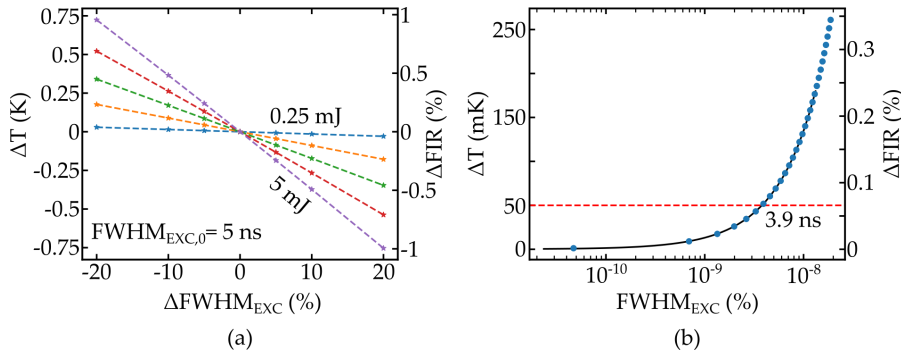


Figure 5.9: Temporal pulse fluctuations and the consequence on the FIR measurement (a) and the estimation of the achievable resolution depending on pulse duration (b)

Figure 5.8a the populations of the thermally coupled emission levels  $N_1$  and  $N_2$  reach their respective maximum closely following the excitation pulse, whereas the population of the lower levels  $N_3$  and  $N_4$  are shifted due to the lifetime of the upper levels, as expected. The FIR caused by the fluorescence emission over time is given in Figure 5.8b and 5.9a depending on energy and pulse duration fluctuations,

respectively. The amplitude of the error is similar and for both types of fluctuations fluctuation ranges of 20% were calculated to cause a temperature error of approximately 0.75 K.

This error  $\Delta T$  does not directly correlate to the actual resolution achievable in a measurement, as additional noise sources need to be factored in. Therefore, this value should rather be considered as a minimum value. It becomes apparent that in order to perform high precision temperature measurements, pump rate fluctuations need to be minimized by using stabilized short pulse pump lasers, however even stabilized OPO systems exhibit  $\pm 6\%$  energy fluctuations [59]. The dependency of  $\Delta T$  on pulse duration and a constant energy

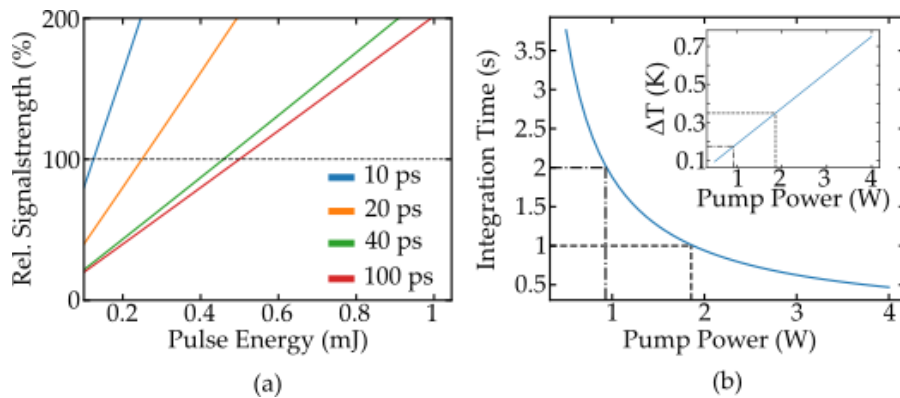


Figure 5.10: Requirements for pulse energy (a) and pumping power (b) to maintain the signal strength of a nanosecond excitation and the temperature deviation caused by laser absorption (inset b).

fluctuation of 10% is shown in Figure 5.9b, and as seen pump pulse durations below one nanosecond should be preferred.

Apart from pump noise, the overall error budget is also influenced by the strength of the emitted fluorescence. Therefore, pump energy and power for picosecond and continuous lasers, respectively, were calculated so that signal strength remains equal to that achieved with a 3.9 ns pulse excitation as marked in Figure 5.9b. The results are shown in Figure 5.10 and highlight the two optimum pump regimes for nanothermometry: short pulse and continuous wave excitation.

The pulse energy needed for an excitation duration of 100 ps is approximately 0.5 mJ, and this pump regime can be used for high precision measurements even without the exact knowledge of material parameters like the emission lifetimes. However, especially for cost effective measurements, this approach can be undesired as it requires more complex laser sources. A continuous excitation is hence favourable.

On the other hand, the integration time necessary to achieve the same signal strength with a simplified setup using continuous emitting laser diode lies in the range of 1-2 seconds and is thus not applicable for high sampling rates. Additionally, high laser powers may lead to

an increased heat input, and the tolerance of heat input to the sample need to be considered. The steady state temperature deviation caused by 1-2 W incident pump power was estimated with approximately 0.15 K–0.35 K, as depicted in the inset of Figure 5.10. The quantum defect of the Pr:YLF emission was considered as the main heating source and doped SiO<sub>2</sub> was assumed as host material in this calculation. The formalism used for this estimation can be found in [60]. Additional absorption e.g. by the host material may further increase  $\Delta T$  but the overall measurement error caused by heat input can be easily calibrated as shown in Chapter 10.1.

### 5.3 CALIBRATION FOR DIFFERENT PUMP REGIMES

Both of the presented pumping regimes have advantages and disadvantages, and their usage should be carefully chosen depending on the desired application. Since most baseline measurements currently used are conducted with either pulsed or continuous excitation, the formalism presented in Equation 5.13 can be used to transfer baseline measurements. This procedure is described in the following for a switch from pulsed to continuous excitation. The first step is to

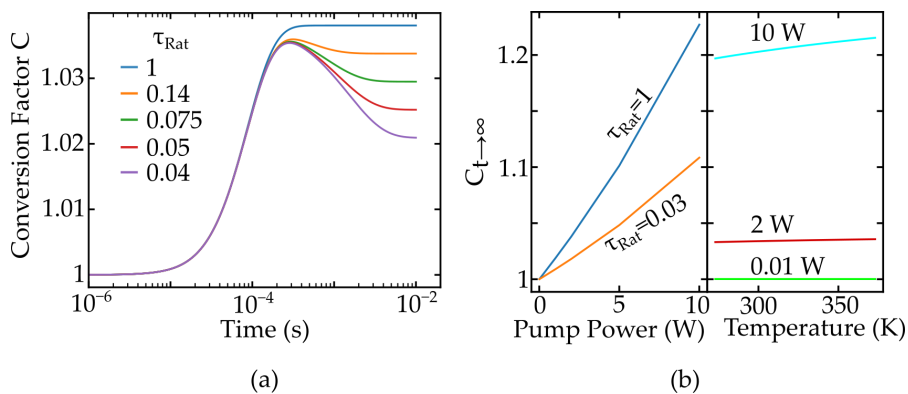


Figure 5.11: Conversion factor  $C$  depending on time and the ratio of lifetimes  $\tau_{\text{Rat}}$  of the lower laser levels in (a), and shown in (b) is the value of  $C$  for long times in dependency of the temperature and the pump power.

measure the lifetimes of the lower levels, giving access to  $\tau_{\text{Rat}}$ . In Figure 5.11a, the conversion factor is again given for different values of  $\tau_{\text{Rat}}$ , with one value fixed to 58  $\mu\text{s}$ . The temporal evolution can be explained by the different onsets of the steady state regime combined with varying absorption strength of the emission lines. Once the material coefficients are identified the main parameters varied during measurements are pump power and temperature of the surrounding media. The pump power is adjusted during a measurement to improve the signal-to-noise ratio. The temperature needs to be included, because re-absorption also depends on temperature via the Stark level

population, as seen in Equation 5.10. Especially the dependency of re-absorption on the temperature is important for the formalism, as it shifts the assumed single exponential Boltzmann dependency of the FIR on temperature given in Equation 5.5. This shift factor is applied

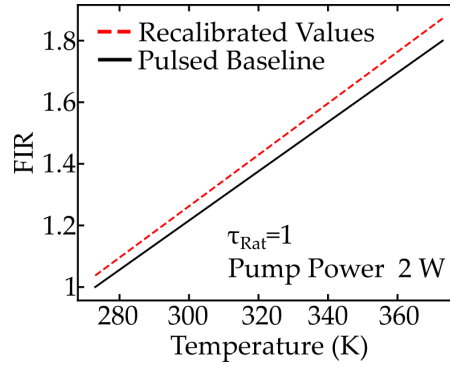


Figure 5.12: Typical FIR evolution for Pr:YLF nanothermometers [22] measured with pulsed excitation in black and the re-calibrated version determined by applying the correction factor  $C$ .

to an approximated FIR evolution for Pr:YLF nanothermometers [22] and the results are shown in Figure 5.12. As depicted the correction of FIR therefore helps to prevent a systematic overestimation of the measured temperature in cw-measurements.

#### 5.4 SPATIAL RESOLUTION

Besides a good temperature resolution, the ability to measure temperature inside spatially restricted volume is another major benefit of nanothermometers. But measurement of the actual spatial resolution is difficult especially in the case of dispersed nanocrystals. The three most important parameters for this are the focal size of the excitation beam, the microscopic statistical movement of single crystals, and in the case of dispersed nanocrystals the displacements caused by macroscopic convection. However, because macroscopic convection flows heavily depend on the application their influence is not dealt with in this general description.

The most basic restriction on spatial resolution stems from the spatial distribution of the excitation function, which is proportional to the focal diameter of the pump laser. The minimal diameter of a laser beam depends on its wavelength  $\lambda$ , the beam divergence  $\nu$ , the refractive index  $n$  of the medium and the beam quality factor  $M^2$ . Put together the beam waist  $w_0$  [35] in the case of a Gaussian beam is defined by

$$w_0 = M^2 \frac{\lambda}{\pi n \nu}. \quad (5.14)$$

This equation reveals that the minimal beam waist is mainly limited by wavelength, as the beam divergence can be set by the optics used



in the setup. The  $M^2$  for an ideal Gaussian beam is equal to one, but as most laser systems are not single mode, their  $M^2$  parameter may be in the range of 10 or 20 leading to a spot size in the micro meter range.

The spatial resolution for a given excitation diameter further depends on the particle movement. The mean displacement

$$\lambda_x = \sqrt{\left(\frac{k_b T}{3r\eta\pi} t\right)} \quad (5.15)$$

of particles dispersed in a liquid depends on the temperature  $T$ , the particle radius  $r$ , the viscosity of the dispersion  $\eta$  and the time  $t$  [61]. The influence of this displacement on the spatial resolution is illustrated in Figure 5.13 for a particle radius of 15 nm. The maximal

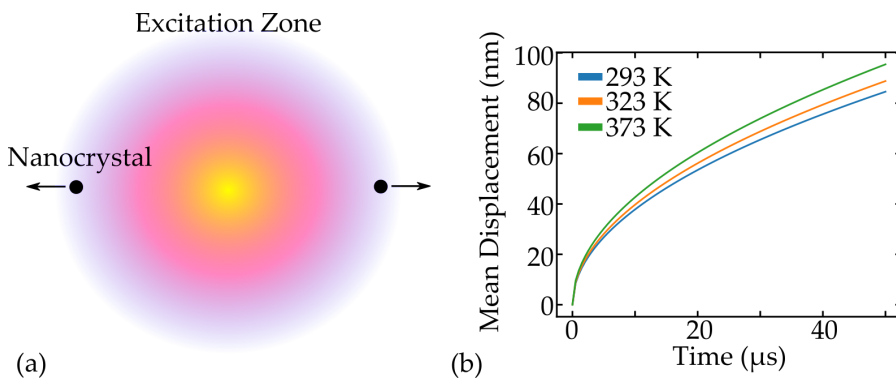


Figure 5.13: Influence of statistical particle movement on the spatial resolution, with the displacement assumed to be perpendicular to the excitation zone (a) and the mean displacement depending on the temperature (b).

effect can be estimated by assuming a movement perpendicular to the excitation zone, as seen in Figure 5.13a. The temporal emission of fluorescence is bounded by the emission lifetime and therefore the mean displacement is calculated for times below  $50 \mu s$ , corresponding to an approximated emission duration. As depicted in Figure 5.13b particles move approximately 100 nm in this time span, corresponding to a velocity of 2 mm/s depending on the temperature.

Because the heat exchange of the particle and the surrounding media is much faster than the emission lifetime, as established in the previous sections, this translates not only to a reduced spatial resolution but also a potential temperature error if different temperature reservoirs are considered. However, strong temperature gradients are not expected in this thesis and the influence in spatial resolution outweighs the temperature error.

Consequently, if a high spatial resolution even in the presence of particle movement is desired either the emission lifetimes needs to be minimized, which results in a worsening of the efficiency or the fluorescence emerging from ions outside the considered region needs

to be excluded. As mentioned before, short lifetimes are generally not desired and therefore, the second approach should be favoured. One way to suppress fluorescence emission is utilizing stimulated emission as described in Chapter [12](#).

## MATERIAL SELECTION

---

Based on the previously established relations, the selection of nanocrystals for nanothermometry can be carried out. The most important criteria are:

1. *Energy Gap of the Active Ion.* The relation  $\Delta E/k_B T$  [21] needs to be considered to balance high sensitivity, a large measurement range, as well as a fast thermalization of the energy levels. Generally,  $\Delta E$  values of  $400-1000\text{ cm}^{-1}$  should be optimal for measurements at room temperature.
2. *Energy Level Structure.* The relative energetic positions of the energy levels determine characteristics like the occurrence of re-absorption effects or sensitivity to external fields.
3. *Particle Size.* The particle size influences temperature exchange between nanocrystal and surrounding media, particle movement and the efficiency of fluorescence emission [36]. Therefore, a compromise in terms of particle size needs to be made between fast heat exchange and efficient emission. Based on this, particles with a radius  $\gg 200\text{ nm}$  should be excluded because of their slow heat exchange, as seen in Figure 4.2
4. *Chemical Characteristics.* Chemical aspects such as the complexity of synthesis or toxicity are criteria mostly used for selection of the host crystal systems.

The two crystal systems used in this work are Er,Yb:NaYF and Pr:YLF, and the following sections demonstrate why these two classes can be used to cover most applications based on the aforementioned criteria.

### 6.1 SPECTROSCOPIC PROPERTIES OF THE ACTIVE IONS

Rare earth ions are optimal candidates for the active material in nanothermometry as stated in the previous section of this part. Figure 6.1 presents an overview of different trivalent rare earth ions and their respective optical transitions [1, 20, 23, 45, 62]. All of the depicted ions fulfil the minimal requirement for nanothermometry, as they all offer emission lines from separated yet thermally coupled energy levels. In the context of this thesis, the transmissions in the visible spectrum are prominently included, because they avoid the absorption of different common host materials as e.g. water or polymer. The decision which of the ions suits the specific applications best can then be made based

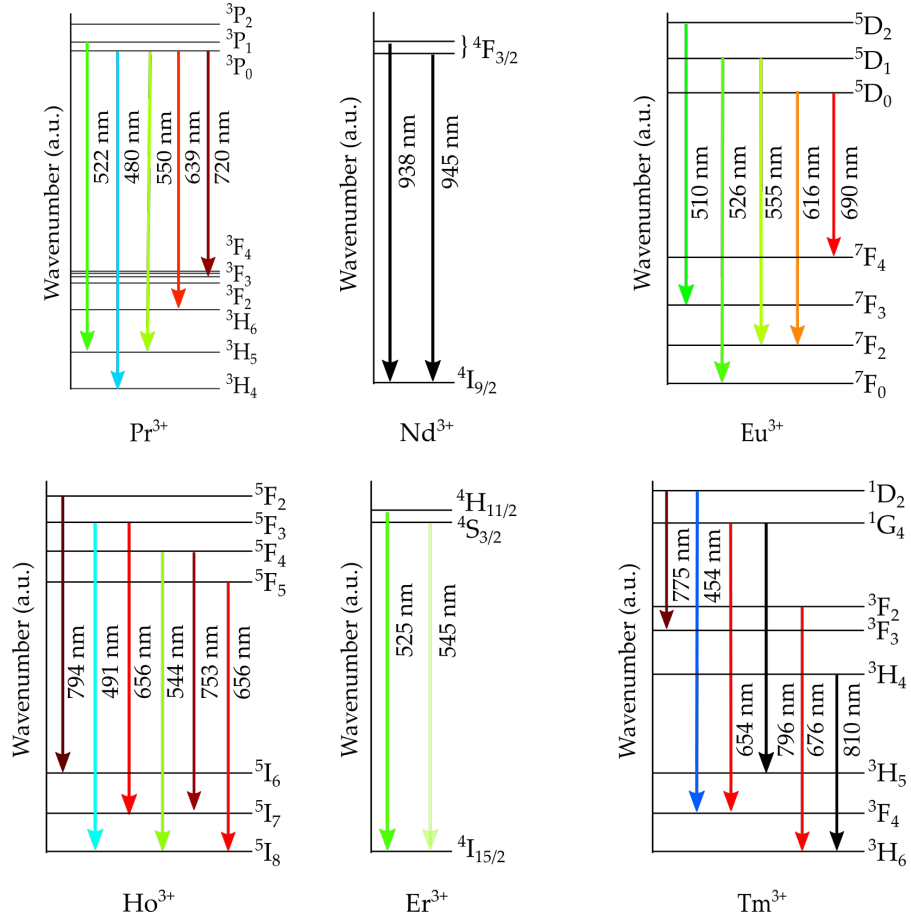


Figure 6.1: Schematic overview of the spectral emission lines present in different rare earth candidates for nanothermometry [1, 20, 23, 45, 62, 63].

on the criteria outlined in the previous sections. First the relevant energy gap has to be considered, as this is the main limitation for the sensitivity. The corresponding values are presented in Table 6.1, with values for the reasonable minimal and maximal gap between two emission levels, if there are multiple possibilities. The three most promising ions in that regard are  $\text{Pr}^{3+}$ ,  $\text{Ho}^{3+}$  and  $\text{Er}^{3+}$ , as the corresponding energy levels are large enough to ensure high sensitivity but still in the range of the phonon energy of common host materials. The respective emission cross sections can be compared as a measure for the relative strength of the emission. The relevant values for the largest individual cross section are taken from ions doped in  $\text{LiLuF}$  crystals to be  $210 \times 10^{-25} \text{ m}^{-2}$ ,  $32 \times 10^{-25} \text{ m}^{-2}$ ,  $19.1 \times 10^{-25} \text{ m}^{-2}$  for  $\text{Pr}^{3+}$ ,  $\text{Er}^{3+}$  and  $\text{Ho}^{3+}$ , respectively. Therefore in terms of emission cross section  $\text{Pr}^{3+}$  and  $\text{Er}^{3+}$  should be favoured. A closer look at the energy level structure is relevant to get an understanding of the possible re-absorption, as well as susceptibility to external fields. Especially  $\text{Er}^{3+}$  seems to be favourable in regards of re-absorption, as the two

Table 6.1: Energy gaps between upper energy levels of the transitions depicted in Figure 6.1

Ion	Host	$\Delta E_{\min}$ (cm <sup>-1</sup> )	$\Delta E_{\max}$ (cm <sup>-1</sup> )	Source
Pr <sup>3+</sup>	YF <sub>3</sub> , YLF	587, 583	–	[54, 64]
Nd <sup>3+</sup>	YAG	80	–	[21]
Eu <sup>3+</sup>	YNaF	1880	2410	[62]
Ho <sup>3+</sup>	ZBLAN	448	2949	[63]
Er <sup>3+</sup>	YNaF	700	–	[20]
Tm <sup>3+</sup>	Y <sub>2</sub> O <sub>3</sub>	3560	5980	[23]

dominant emission lines both share the same lower energy level. Based on this, nanothermometers utilizing Er<sup>3+</sup> are expected to be mostly insensitive to pump fluctuations and are promising candidates for high resolution measurements. Both, Pr<sup>3+</sup> and Ho<sup>3+</sup> offer similar pairs of emission lines, but e.g. the emission line centred at 550 nm of Pr<sup>3+</sup> is weak compared to the other emission lines. Considering external fields, a larger spectral separation of the emission peaks is beneficial, therefore Pr<sup>3+</sup> and Ho<sup>3+</sup> should provide more robust measurements in these cases.

The spatial resolution achievable with the specific ion can be linked to the pump wavelength, as this determines the minimal focus diameter. All of the three materials offer excitation transitions in the blue spectral range [45] with the largest corresponding cross section again for Pr<sup>3+</sup>. The efficiency of Er<sup>3+</sup> and Ho<sup>3+</sup> pumping is often increased by co-doping with Yb<sup>3+</sup> shifting the transition wavelength to the infrared region, giving Pr<sup>3+</sup> the edge in this regard. Lastly the degree of research in other applications can be considered for a simplified access to material parameters, where Pr<sup>3+</sup> and Er<sup>3+</sup> have a strong background in laser development. As a result of this section, the active ions Pr<sup>3+</sup> and Er<sup>3+</sup> can be identified as an active material combination that covers all necessary specifications.

## 6.2 SELECTION OF THE HOST CRYSTALS

The suitable host crystal is identified after the active ions are found. Although assumptions of the phonon energy were already included in the previous sections, the range of crystals fulfilling these assumptions is huge. The criteria for this selection are controllability of the synthesis, state of research or biological compatibility.

The most commonly used laser crystals are either oxide crystals e.g. YAG or fluoride crystals e.g. YLF. Especially fluoride crystals offer advantages for nanothermometry based on their chemical structure. One benefit is the high band gap of fluorides of up to 12 eV [65], which results in reduced optical losses and a wide range of transparency.

Another asset is that fluorides also have lower phonon energies than comparable oxides [65], which reduces quenching effects, but are still high enough for rapid thermalization. Other plus points that are more prominent for laser applications, such as minimized thermal lensing, due to a negative thermo-optic coefficient [65], do not directly affect nanothermometry but increase the general use of fluoride crystals and with that the research of the material. Therefore, these advantages also help to push fluoride crystals in nanothermometry.

Table 6.2 presents a selection of fluorides that are compatible host crystals for the chosen active ions. The different crystals are grouped according to their symmetry. The space group of the crystals is denoted

Table 6.2: Selection of active ions and compatible fluoride host crystals with ordered structure [66] denoted by the Schönflies notation.

Ln <sup>3+</sup>	Space Groups in ascending order of symmetry						
	C <sub>2h</sub> <sup>3</sup>	D <sub>2h</sub> <sup>16</sup>	C <sub>4h</sub> <sup>6</sup>	D <sub>3d</sub> <sup>2</sup>	D <sub>3d</sub> <sup>4</sup>	C <sub>3h</sub> <sup>1</sup>	O <sub>h</sub> <sup>5</sup>
Pr	$\beta$ -BaYF		LiYF, LiGdF, LiLuF		KYF, LaF, PrF		
Er	$\beta$ -BaYF, $\beta$ -BaErF, $\beta$ -BaTmF	$\alpha$ -BaLuF, ErF	LiYF, LiYbF, LiLuF		KYF, NaYF LaF		CaF, SrF
Ho	$\beta$ -BaYF	HoF	LiYF, LiHoF, LiYbF, LiLuF	KYF			CaF, SrF

by the Schönflies notation and its degree of symmetry determines the maximal symmetry of the ion site at which the emitting ion is positioned [67]. Therefore, the space group strongly influences the emission characteristics. Unordered crystals, such as YAG, lead to a broadening of the energy levels whereas ordered structures tend to preserve discrete transitions [66]. Laser crystals with a high degree of symmetry should therefore be preferred for nanothermometry. Besides this, the atomic radius of the replaced ion, e.g. Lu in LuLiF, and the dopant, e.g. Pr, should be as similar as possible to prevent further distortions of the crystal lattice.

The controllability of crystal synthesis is a more practical criterion to choose the host crystal. Both systems YLiF and YNaF can be synthesized using a thermal decomposition route [68, 69] which is widespread procedure. Additionally, coprecipitation methods [22] or hydrothermal methods [70] can be applied. Therefore, the availability of synthesis techniques is no strict limitation for the crystal selection.

The toxicity of nanocrystals was researched for YNaF, where no strong cytotoxic effects were found for particles smaller than 30 nm

[71], and the observed effects were attributed to the cyclohexane present in the synthesis. In terms of research and available material data, both YLiF and YNaF show a sufficient degree and both have already been used in various nanocrystal applications [20, 22, 62, 72]. Combined with the state of research performed for the different crystals systems, YLiF and YNaF were chosen as host crystals for  $\text{Pr}^{3+}$  and  $\text{Er}^{3+}$ , respectively. The specific synthesis routes performed for the different samples are briefly described in the following parts.





Part III

TEMPERATURE RESOLUTION IN  
NANOTHERMOMETRY



## SAMPLE DESCRIPTION

---

All samples used to obtain the results presented in this thesis were produced inside the collaboration project *LaPOF*<sup>1</sup> and were manufactured by scientist at the Technische Universität Braunschweig. This chapter aims to give a brief description of the preparation steps necessary to manufacture these samples.

As previously discussed, two different fluoride nanocrystal classes were used as nanothermometers, namely Yttrium-Lithium-Fluoride (YLF) and Yttrium-Sodium-Fluoride (YNaF). The crystals were doped with Praseodymium ( $\text{Pr}^{3+}$ ) or co-doped with Erbium ( $\text{Er}^{3+}$ ) and Ytterbium ( $\text{Yb}^{3+}$ ), respectively. The complete abbreviations for the active nanocrystals are therefore Pr:YLF and Er,Yb:YNaF, and both nanocrystals were further embedded in different host materials according to their respective advantages that were discussed in the previous chapters.

The most commonly used type of applications of nanothermometers are liquid dispersions. Consequently, the first characterized nanocrystal system in this thesis are Pr:YLF nanocrystals dispersed in cyclohexane. These types of crystals show efficient excitation in the blue spectral region making them suitable candidates for high spatial resolution measurements, as will be discussed in Chapter 12 of this thesis. Additionally, their energy level distribution leads to a large spectral separation between the emission lines, thus simplifying the measurements. Disadvantages of this dispersion system are also presented, such as a luminescence background or a reduced signal-to-noise ratio due to a short interaction length. The achieved temperature resolution with this system was limited to approximately 0.4 K due to this effects. Lastly, the numerical model presented in Chapter 5.2.2 was applied to correct errors caused by reabsorption in measurements conducted with continuous excitation, showing the viability of this approach.

These drawbacks, particularly in terms of signal-to-noise ratio, were addressed by utilizing a polymer as host material for the second nanocrystal system. Specifically, a polymer fiber was chosen as the host for the Er,Yb:YNaF nanocrystals. One benefit of this configuration is the energy level structure, which favours continuous excitation and with that enables high temperature resolutions. The light guiding effect of a fiber is expected to further boost the signal-to-noise ratio, albeit at the cost of spatial resolution. Therefore, the goal of this thermometer development was to optimize temperature resolution,

---

<sup>1</sup> The collaboration project LaPOF was funded by the state of Lower Saxony and the European Union, Fundnumbers EFRE-SER 2014-2020, 85003655 and 85003502.

and a resolution of 19 mK was reached thus improving the resolution of dispersed Pr:YLF nanocrystals by a factor of roughly 20.

## 7.1 PR:YLF NANODISPERSIONS

The first system investigated consists of active nanocrystals dispersed in a liquid solvent. The nanocrystals are Yttrium-Lithium-Fluoride (YLF) crystal doped with trivalent Praseodym  $\text{Pr}^{3+}$  (Pr). This section contains an overview of the material synthesis and characterization. The main parameters included are particle size and a description of the luminescence background caused by the oxidation of the ligand system.

### 7.1.1 Nanoparticle Synthesis

The Pr:YLF nanocrystals were manufactured by the Technische Universität Braunschweig, using a thermal decomposition method [73, 74]. Components of a lanthanide chloride ( $\text{PrCl}_3$ ) were combined with oleic acid and octadecene. The solution was then subjected to different heating steps, and additional chemical compounds such as  $\text{NH}_4\text{F}$  and  $\text{LiOH}$  were added in between, combined with stirring. After this cycling, ethanol was added to the solution to facilitate the precipitation the nanocrystals, which were then collected using a centrifuge. In the last step, the nanocrystals were washed and re-dispersed in cyclohexane. The desired doping concentration of  $\text{Pr}^{3+}$  ions was set by adjusting the concentration of lanthanide chloride added in the first step. However, no analysis of the doping concentration was performed, therefore values used in the following should be regarded as nominal doping concentrations.

TEM measurements were carried out to analyse the size distribution of the nanocrystals, and the results are shown in Figures 7.1 and 7.2, with  $AC$ ,  $BD$  and  $a$  corresponding to the long axis, the short axis and the edge length of the projected diamond shaped surface, as shown in the insets of Figures 7.1b and 7.2c, respectively.

In accordance with the literature a tetragonal crystal phase was assumed for this analysis [75]. The particle size, determined by the longest crystal axis was measured to be between  $\approx 11$  nm and  $\approx 16$  nm with a weak correlation between particle size and doping concentration, as reported in [75]. The length of the different crystal and the calculated volume is shown in Figure 7.3.

### 7.1.2 Influence of the Dispersion Medium

The synthesized nanocrystals were dispersed in a liquid medium, as mentioned in the previous section. The most two important chemical distinctions in terms of the dispersion medium are the one between

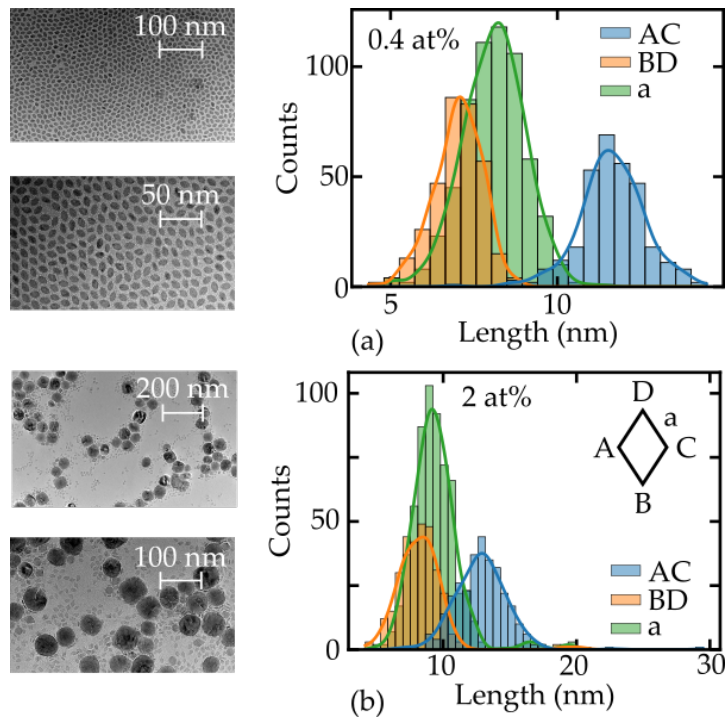


Figure 7.1: TEM measurements and size distribution of particles with doping concentrations 0.4 at% and 2 at%.

non-polar and polar, and also between hydrophilic and hydrophobic liquids [76]. These parameters determine the solubility of nanocrystals and the maximum concentration before agglomeration sets in.

In terms of temperature measurements especially the freezing point and the boiling point are also of importance, as a phase change of the host medium can be expected to heavily influence the measurement, e.g. by diminishing the heat exchange between nanocrystal and its surrounding medium. Additionally, knowledge of other temperature anomalies comparable to the density of water helps to identify error sources, as in the case of the density influences the viscosity and with that particle motion can be expected.

Some of the most commonly used dispersion media are chloroform [77], water [78] or cyclohexane [79]. Cyclohexane was used as host material in this thesis, however the influence of the mentioned solvents on the performance of the nanothermometers can be neglected, because all measurements were performed in the absence of phase transitions. The main reason cyclohexane was chosen instead of e.g. water is the similar polarity of cyclohexane and PMMA, which potentially enables further doping of these nanocrystals in polymers without additional surface treatments [69].

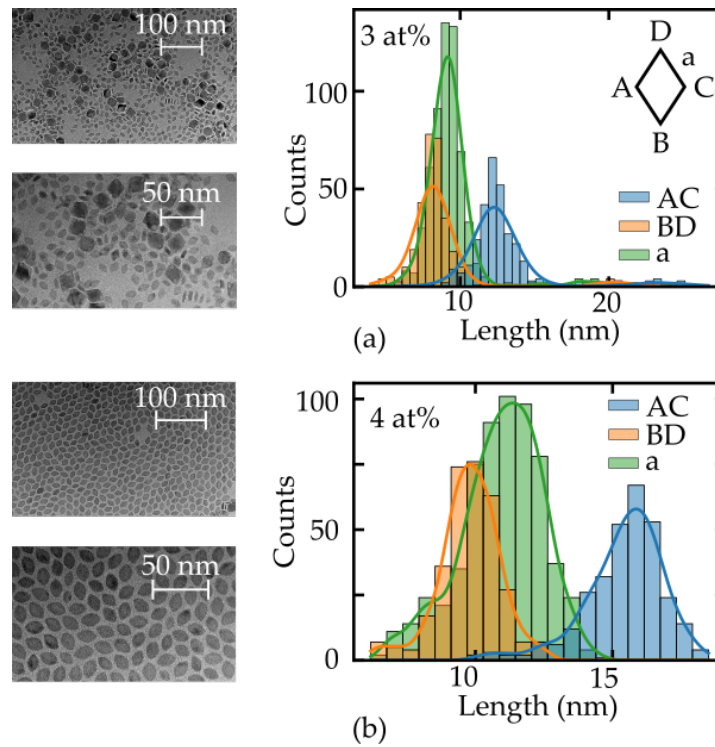


Figure 7.2: TEM measurements and size distribution of particles with doping concentrations 3 at% and 4 at%.

### 7.1.3 Emission Characteristics of Pr:YLF Nanocrystal Dispersions

Emission measurements were performed as an additional verification of the nanocrystal synthesis. An excerpt from the energy level scheme of Pr:YLF and exemplary measured emission spectra of bulk Pr:YLF are shown in Figure 7.4. The measured emission includes the main emission lines expected from the energy level scheme [22, 45], with the most prominent emission centred between 607 nm–611 nm. Relative to this, the lines at 639 nm, 522 nm and 720 nm, follow in descending order.

As described in previous sections, the key prerequisite for nanothermometry is emission from thermally coupled levels. This condition is met by the emission originating from  $^3P_1$  at 522 nm and the different lines starting from  $^3P_0$  at 607 nm, 639 nm and 720 nm, respectively. The energy gap between  $^3P_1$  and  $^3P_0$  is approximately  $550\text{ cm}^{-1}$  [64]. The fluorescence spectra recorded from different nanocrystal samples also includes the aforementioned emission lines with an additional luminescence background, as shown in Figure 7.5a. This broad signal can be attributed to the oleic acid ligand system, and similar phenomena were observed in [80]. More Specifically, the broad emission band from 400 nm to 850 nm can be attributed to an oxidation of the oleic acid which occurs under the influence of heating and in the presence of oxygen [80]. Undoped YLF nanocrystals were used to

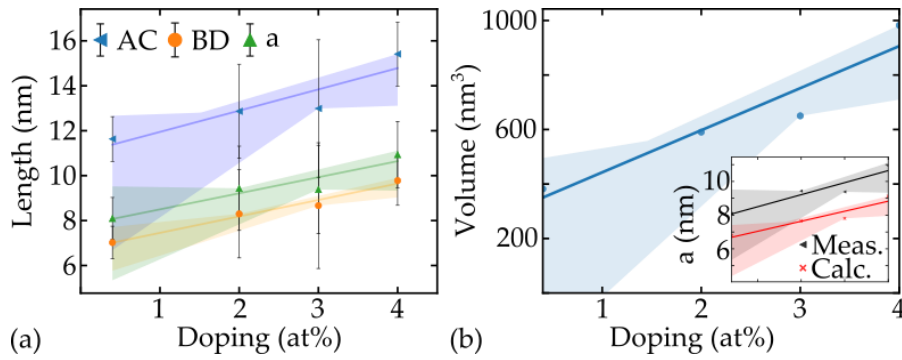


Figure 7.3: The length of the different crystal axis  $AC$ ,  $BD$  and  $a$  depending on the doping concentration in (a) and calculated values of the crystal volume depending on concentration (b) and the deviation the measured length of  $a$  from the expected value of a perfect tetragonal phase in the inset (b). The error bars in Figure (a) result from the statistical distribution of measured length values, and the coloured area gives the confidence interval of the linear fit.

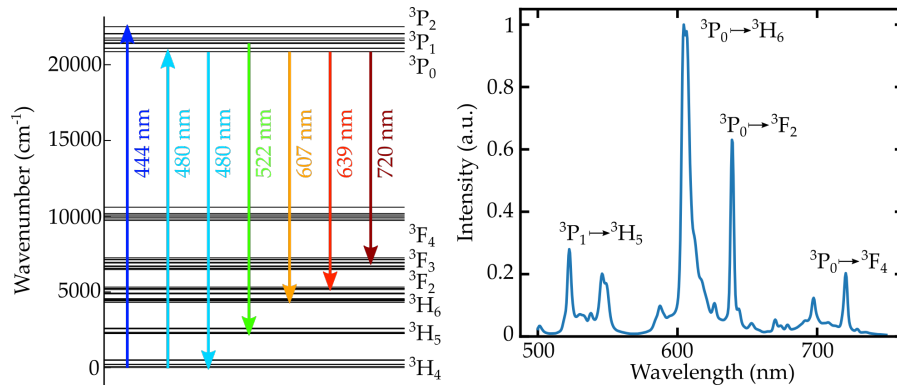


Figure 7.4: Excerpt from the energy level diagram of Pr:YLF [22, 64] with the relevant optical transitions in the visible spectrum (a) and a fluorescence spectrum of Bulk Pr:YLF measured after excitation at 444 nm (b).

further investigate this and confirm the independence of this emission from the active ions. The resulting broad emission normalized to the absorbed pump power is shown in Figure 7.5b. For this measurement, a continuous wave laser diode emitting at 444 nm was used and consequently a long pass filter was applied to remove the residual pump light. Again a broad signal centred around 555 nm-560 nm can be observed, but no dependence of the spectral shape on pump power occurs. This confirms the role of the ligand system and hints at oxygen contaminations during the particle synthesis.

Because this luminescence background varies with the wavelength and the degree of oxidation its influence on the usage of Pr:YLF nanothermometers is difficult to quantify. Therefore, great caution must be exercised in future synthesis to prevent the oxidation. Additionally, the ligand system may also be removed for example with acid [81].

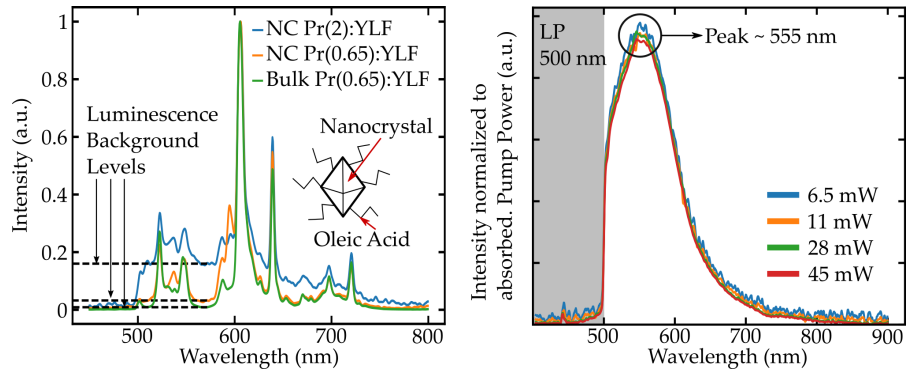


Figure 7.5: Emission Spectra of different Pr:YLF samples (a) and measurement of the luminescence background of undoped Pr:YLF nanocrystals after continuous wave excitation for different levels of absorbed pump power.

But in this case, the nanocrystals tend to agglomerate and chemical treatment of the surface is still necessary by adding other ligands [76].

This ligand exchange may even be advantageous as it might increase the luminosity of active nanocrystals. For example, oleic acid also has potential benefits for fluorescence applications, as it may provide a shielding against surface quenching effects [81]. One of the most prominent quenching mechanisms is the multiphonon quenching (MPQ) that describes the energy transfer from electrons to phonons of the host material [82]. The rate of this transfer is inverse proportional to the sixth power of the distance between donor and acceptor. Therefore even a thin layer of oleic acid on the surface of the nanocrystal may shield the electrons and minimize this quenching pathway. However, this shielding is for not as efficient as the shielding achieved by an additional crystal shell. Furthermore, the shielding depends on both, the optical transitions and the solvent [81], therefore disadvantages still outweigh the benefits. Different synthesis routes, such as coprecipitation [22], could also be used to minimize the influence of surface ligands, but the feasibility of this procedure to repeatedly produce monodisperse and small Pr:YLF nanocrystals has yet to be established. Because of this the optimization of the synthesis should be regarded as one main part of future nanothermometry research.

## 7.2 ER,YB:YNAF DOPED POLYMER FIBER

A polymer fiber doped with Er,Yb:YNaF nanocrystals was also manufactured by the Technische Universität Braunschweig [69]. The most important specifications of this doped fiber as well as a general analysis of loss mechanisms inside polymer fibers are discussed in the following sections.



7.2.1 *Er,Yb:YNaF Nanocrystals*

Er,Yb doped upconversion nanocrystals (UC-NC) are well researched for temperature sensing applications [20, 83–85] and offer specific advantages due to energy level structure, spectroscopic characteristics and chemical specifications. There are different possible synthesis routes for this fluoride crystals system [69, 70], and the nanocrystals used for this thesis were manufactured using thermal decomposition in an Oswald ripening process [69]. In this process, hydrated lanthanide chlorides of the active ions Er ( $\text{ErCl}_3 \cdot 6\text{H}_2\text{O}$ ), Yb ( $\text{YbCl}_3 \cdot 6\text{H}_2\text{O}$ ) were dissolved in methanol. Additionally, Gadolinium ( $\text{GdCl}_3 \cdot 6\text{H}_2\text{O}$ ) was added during the synthesis to assure the highly luminescent hexagonal  $\beta$ -crystal phase [75]. Following this, oleic acid, which acts as a ligand, was added and cycles of heating and stirring were applied. After these cycles were finished, the resulting nanocrystals were washed and redispersed. A more detailed description of the manufacturing can be found in [69].

The resulting doping concentration was determined by the amount of added lanthanide chloride and the final chemical formula for the nanocrystals is  $\text{Yb,Er,Gd}(20:2:20):\beta\text{-NaYF}_4$ . Because all of the used optical transitions occur in Er and Yb and the abbreviation used in this work remains Er,Yb:YNaF. The hexagonal crystal phase was confirmed by comparing X-ray diffraction measurements with reference diffraction spectra, as depicted in Figure 7.6a.

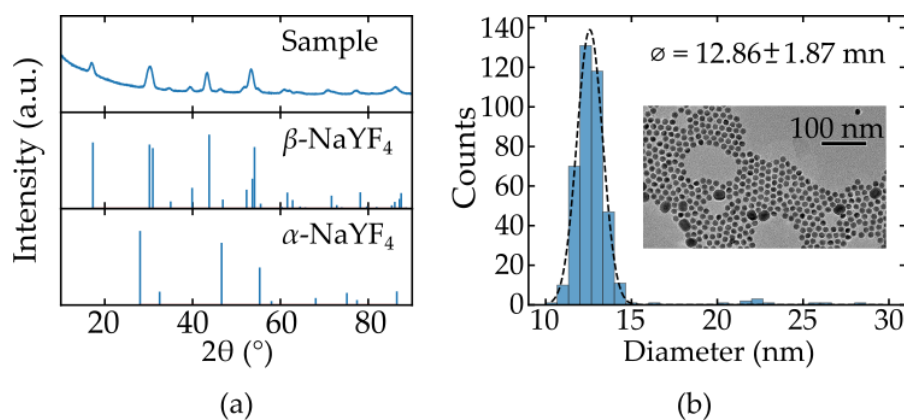


Figure 7.6: Characterization of Er,Yb:YNaF nanocrystals by X-ray diffraction (a) and TEM Measurements (b). The definition of the crystal phases in (a) is based on ICSD: 98-005-1917 and ICSD: 98-007-7100 for the  $\beta\text{-NaYF}_4$  and  $\alpha\text{-NaYF}_4$  crystal phase, respectively [69].

TEM measurements were again used to investigate the particle size, and a mean diameter of  $12.86 \pm 1.87$  nm was revealed, as shown in Figure 7.6. The particle size is important to estimate the influence of scattering, but based on the small size and the low refractive index

miss match ( $n_{\text{Er,Yb:YNaF}} = 1.4748$  [86],  $n_{\text{Polymer}} \approx 1.49$  [86]) to the host polymer, scattering caused by the nanocrystals can be neglected.

The energy level characteristics of the nanocrystals and a typical emission spectrum measured from an excited doped polymer fiber, is shown in Figure 7.7. The emission spectrum reveals that the influence of the host polymer on the spectral positions of the energy lines can be neglected compared to other host materials [20]. The optical excitation

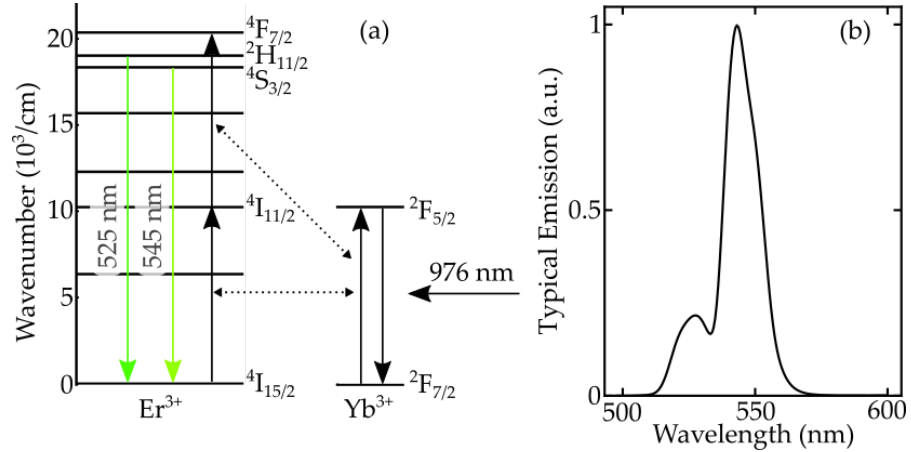


Figure 7.7: Section of the energy level scheme of Er,Yb:YNaF nanocrystals [83] (a) and a typical emission spectrum measured from an optical excited doped fiber (b).

of Er,Yb:YNaF was performed with an up-conversion process to enhance the efficiency. This leads to an anti-stokes like mechanisms and a blue shift between excitation and emission. This process is based on multi-photon absorption and energy transfers between  $\text{Er}^{3+}$  and  $\text{Yb}^{3+}$ . First electrons of the  $\text{Yb}^{3+}$  are optically excited, via pumping with laser light at 976 nm, from  $^2F_{7/2}$  to  $^2F_{5/2}$ . From this level multiple energy transfers happen which lead to a two-step excitation of the  $\text{Er}^{3+}$ , with  $^2I_{15/2} \rightarrow ^2I_{11/2}$  and  $^2I_{11/2} \rightarrow ^4F_{7/2}$ , respectively. The upper emission levels  $^2H_{11/2}$  and  $^4S_{3/2}$  are then populated via non-radiative transitions. The emission lines most commonly used for nanothermometry are centred at 525 nm and 545 nm and originate from these levels with the corresponding transition back to the ground state  $^4I_{15/2}$ , as depicted in Figure 7.7a.

### 7.2.2 Manufacturing of the Fiber

After the nanocrystals were successfully synthesized, they had to be incorporated inside the polymer fiber. This was again achieved by scientists at the Technische Universität Braunschweig by applying an in-situ polymerization. Co-polymers consisting of mixed methyl methacrylate (MMA) and cyclohexyl methacrylate (CHMA) were chosen as the host polymer. Contrary to polymer fibers purely based on poly-methyl methacrylate (PMMA) [87], this host enables doping

of UC-NC while minimizing agglomeration and precipitation of the UC-NC, which in terms would lead to a decrease in transparency. Still, a ligand consisting of an oleic acid had to be added to increase the solubility of the UC-NC in the co-monomer.

The solution of UC-NC and co-monomer was then used in a radical polymerization process to prepare preforms, as depicted in Figure 7.8. The highest doping concentration achieved, while maintaining a transparent preform, was 0.5 wt% and since a high doping concentration leads to strong fluorescence emission, this concentration was used for the thermometer experiments. After this, doped polymer fiber

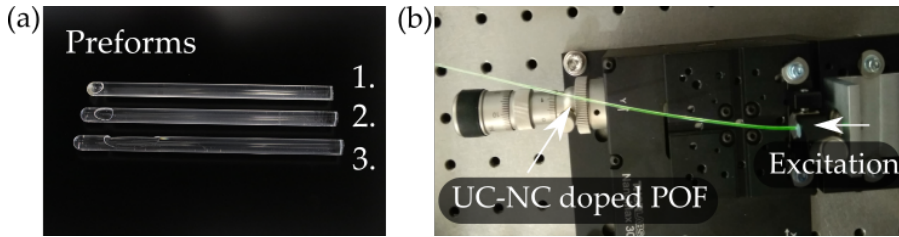


Figure 7.8: Co-monomer polymer preforms 1, 2, and 3 doped with 0.5 wt%, 0.1 wt%, and 0 wt% of UC-NCs, respectively (a). An UC-NC doped polymer fiber after excitation with 976 nm (b).

cores with a diameter of  $980 \mu\text{m}$  were drawn, using a drawing tower. Afterwards an acrylate cladding was added to the fibers, yielding the final diameter of  $1000 \mu\text{m}$ , as shown in Figure 7.8. A more detailed description of the steps necessary for the fiber manufacturing can be found in [69, 88–90].

### 7.2.3 Absorption in Polymer Fibers

Optical absorption causes material heating, as discussed in Chapter 4.2. This heating is generally not desired in temperature measurements, as it may affect both, the performance of the thermometer as well as the sample. Polymer fibers usually have a stronger attenuation than fused silica fibers [87] due to their chemical structure. Therefore, thorough discussions of the mechanisms responsible for transmission losses are necessary to fully understand the functionality of the UC-NC doped polymer fiber thermometer. The main processes responsible for attenuation of optical transmission are absorption through electronic transitions, scattering, and absorption through molecular vibrations, with the first two dominating for short wavelengths and the latter mainly occurring at longer wavelengths.

The electronic absorption  $\alpha_e$  of polymer fibers consisting of PMMA is approximately described by [91] with

$$\alpha_e(\lambda) = 1.58 \cdot 10^{-12} \exp\left(\frac{1.15 \cdot 10^4}{\lambda[\text{nm}]}\right) \quad (7.1)$$

and depends in this normalized form exponentially on the wavelength  $\lambda$  and the two material specific numeric constants  $1.58 \cdot 10^{-12}$  and  $1.15 \cdot 10^4$  [87]. This mechanism contributes to heating but is only significant for short wavelengths, e.g. at 525 nm the theoretical absorption per meter polymer fiber is approximately 5 ppm.

Scattering occurs at refractive index mismatches caused by small imperfections of the polymer or inclusions. Scattering does not raise the heat input to the fiber but causes loss by destroying the light guiding condition. The mathematical description of loss through Rayleigh scattering  $\alpha_R$  can be simplified [91] to

$$\alpha_r(\lambda) = 13 (633/\lambda)^4. \quad (7.2)$$

In this case the wavelength dependence is expressed as  $\propto \lambda^{-4}$ , and the values 13 and 633 nm arises from scattering measurement of the material at 633 nm and a fitting routine [92].

Figure 7.9 shows the wavelength dependence of both  $\alpha_e$  and  $\alpha_R$  and again highlights the rising influence for shorter wavelengths.

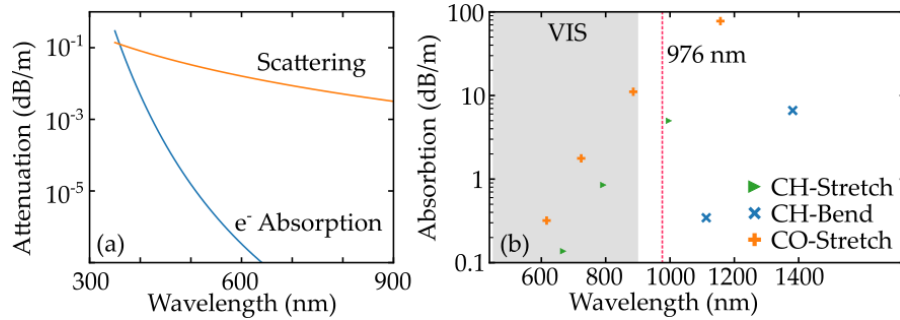


Figure 7.9: Numerical approximation of the strength of different loss mechanisms in polymer fibers. Depicted in (a) is the attenuation caused by Rayleigh scattering and electronic transitions and in (b) the attenuations due to the excitation of vibrational modes in the molecules.

The excitation wavelength of the used UC-NC is 976 nm and the pumping power is expected to strongly exceed the emission power. Therefore, the infra-red absorption caused by the excitation of the higher harmonics of the molecular vibrations is the most important loss mechanism. The influence of the absorption can be estimated, if the atomic composition of the molecules is known. The complete chemical formulas for the different mixture parts of the co-monomer are  $C_{10}H_{16}O_2$  and  $C_5H_8O_2$  for CHMA and MMA, respectively. Therefore C-H and C-O bonds and consequently vibration modes make up for most of the absorption. Both spectral position  $\nu$  and absorption strength  $A$  of these vibration modes can be estimated as described in the following, according to [93].

The potential curve of these molecule systems can be approximated with the Morse potential

$$G(v) = \left(v + \frac{1}{2}\right) - \frac{\sqrt{k}}{2\pi c\mu} x \left(v + \frac{1}{2}\right) \quad (7.3)$$

with  $v$  as the set of natural numbers, the anharmonicity constant  $x$ , and the vibrational ground state

$$\nu_0 = \frac{\sqrt{k}}{2\pi c\mu} \quad (7.4)$$

which depends on  $k$  as a force constant, and  $\mu$  as the reduced mass. The spectral position of the overtones ( $v=2, 3, 4, \dots$ )

$$\nu_v = \frac{\nu_1 v - \nu_1 x v(v+1)}{1 - 2x} \quad (7.5)$$

can be calculated with the fundamental vibration frequency  $\nu_1$ . The formula for the absorption strength  $\alpha$  in dB/m can be derived from the Lambert-Beer law and the transition moment from the ground state to the higher vibrations states, as described in [93] to be

$$\alpha(\nu_v) = 3.2 \cdot 10^5 \frac{\rho}{M_G} n_c \left( \frac{E_v}{E_1^{CH}} \right). \quad (7.6)$$

In this equation  $E_v/E_1^{CH}$  is the relation of energy between an arbitrary vibration mode and the fundamental vibration mode of the C-H bond,  $\rho$  is the density,  $M_G$  is the molar mass, and  $n_c$  is the amount of this specific bound in the macro-molecule. These formulas were used to calculate the vibration mode absorption shown in Figure 7.9b.

From this theoretical description it can be estimated that the absorption of the excitation wavelength lies between 5-10 dB/m, and measurements were conducted to characterize the fiber attenuation in more detail.

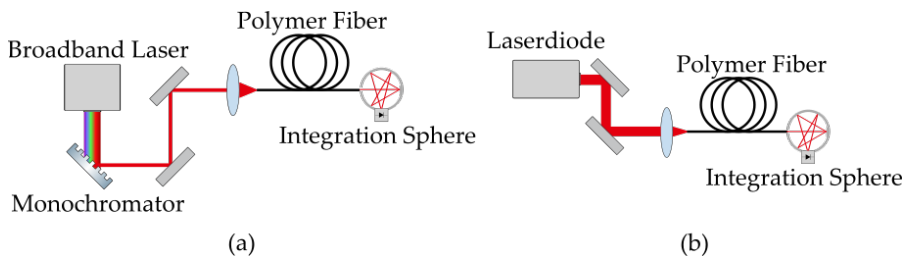


Figure 7.10: The two setups used to measure the attenuation of the polymer fiber. The main distinction between the setups is the excitation laser. The configuration (a) was used to characterize the attenuation in the visible spectral range whereas variant (b) measured the absorption at the excitation wavelength 976 nm.

The setups used for this measurements are shown in Figure 7.10. The attenuation was investigated using the cut-back method [87] to

minimize the influence of the surface quality. A broadband laser source (400 nm-800 nm) was used as light source, as shown in Figure 7.10a, and in a second step the pump absorption was measured with a laser diode emitting at 976 nm, as depicted in Figure 7.10b.

The resulting attenuation spectrum is given in Figure 7.11. The

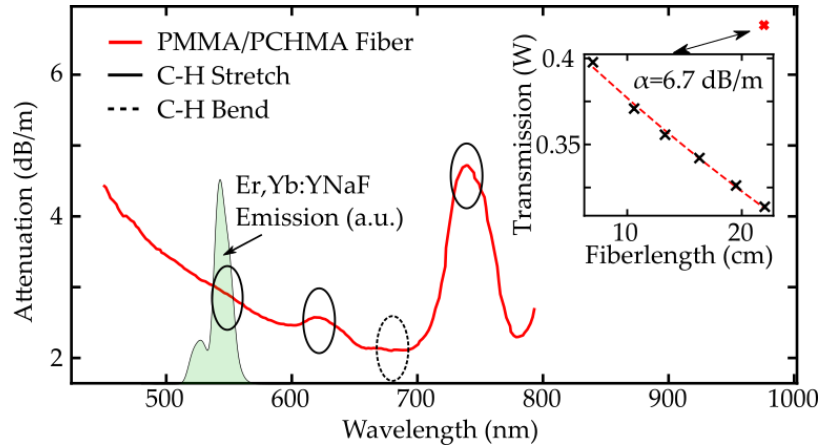


Figure 7.11: Comparison of attenuation of an PMMA/PCHMA fiber with the emission spectrum from Er,Yb:YNaF nanocrystals. Shown in the inset is the measurement data used to estimate the pump absorption.

previously determined absorption peaks can be observed at the calculated spectral positions and the pump absorption is determined to be 6.7 dB/m. Furthermore, Figure 7.11 gives the emission of Er,Yb:YNaF in comparison to the polymer attenuation in arbitrary units. From this data, the attenuation of emerging fluorescence can be deduced to be roughly 3 dB m. The comparison of this measured attenuation with the previously calculated 5 ppm of intrinsic absorption inside the polymer and the vibrational absorption of <math><0.5\text{ dB/m}</math> for a wavelength below 600 nm shows a significant difference with the measured attenuation being much higher. The most probable reason for this deviation is Rayleigh scattering, which as discussed earlier is not caused by doping but either by material defects, impurities or differences in the confirmation of the polymer chains. Because the absorption of the pump wavelength is still much stronger, the influence of fluorescence re-absorption on heat input was neglected. However, the high attenuation entails the need for increased emission and with that for higher pump powers. Because of this, potential optimization in regard of the polymer composition should aim at reducing host attenuation.

## MEASUREMENT SETUPS

Different setups were used to investigate the performance of both thermometer approaches and the variations are based on the sample type, namely fiber or dispersion, as well as the physical properties of the active ions, where the main distinction is the excitation wavelength. The main tasks each setup needs to fulfil are optical excitation, detection of the emitted photons, separation of the different emission lines with a spectrometer and evaluation of the collected data with a computer.

## 8.1 DISPERSION CHARACTERIZATION

The temperature dependent emissions from a bulk Pr:YLF crystal and the dispersed Pr:YLF nanocrystals were measured with two different setups. A pulsed optical parametric oscillator (OPO) was used as excitation source at 444 nm with pulse energies ranging from 1 mJ to 5 mJ. The corresponding setup is shown in Figure 8.1. The fluorescence and residual pump light was spectrally separated using a long pass filter in a transmitting arrangement, and the fluorescence was recorded with a fiber coupled spectrometer with a resolution of 1 nm and a minimum integration time of 2.17 ms.

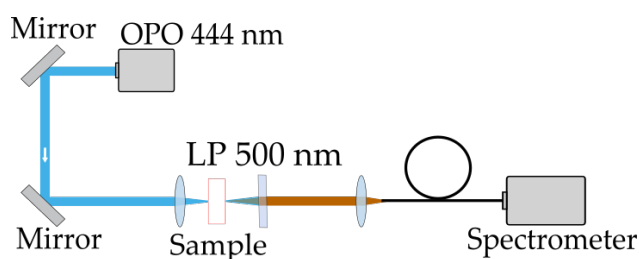


Figure 8.1: Setup used for the measurements of temperature dependent emission of different Pr:YLF under pulsed excitation.

First baseline measurements were conducted using a bulk Pr(0.65 at%):YLF crystal embedded in a copper block, as depicted in Figure 8.2a. The copper block in combination with a thermally conducting foil was chosen to assure mechanical stability as well as sufficient thermal coupling between the laser crystal and the heating element. The results of these measurements were subsequently used to identify emission lines suitable for temperature measurements. Following this, the setup was slightly varied, and different dispersions containing Pr:YLF nanocrystals were used as samples as shown in Figure 8.2b. The temperature for both samples was set and monitored with an electrical transistor

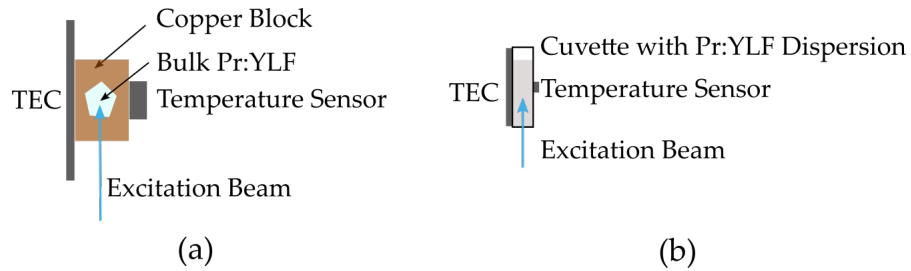


Figure 8.2: Different samples and their installation in the setup. Shown are bulk Pr:YLF (a) and Pr:YLF nanocrystals dispersed in a solution (b). The temperature control of either sample was realized by TECs combined with Pt100 sensors and additional temperature monitoring of the dispersions was performed with a TMP36 sensor.

based thermometer (TMP36) and a thermoelectric cooling element (TEC) combined with a Pt100. Additional calibration measurements were performed to estimate the influence of the thickness of the cuvette on the measured temperature and to access the time necessary to reach a steady temperature distribution inside the cuvette. Conversion factors were extracted from this measurement to re-calculate the sample temperature based on the externally set values between 5 °C and 40 °C.

After the calibration data was obtained using a pulsed pumping scheme, further experiments were conducted to measure the influence of continuous excitation. For this task, the used setup was adapted, since the previously used optical filters did not offer sufficient extinction of residual pump light. The emission was therefore collected perpendicular to the excitation in this configuration, and an additional power meter was added to measure the transmitted pump light as is shown in Figure 8.3. The excitation source for this was a laser diode with a center emission wavelength of 444 nm and up to 5 W output power.

The evaluation of all emission intensities was done by fitting Voigt profiles to the spectral data. A numerical routine was developed to apply additional exponential or polynomial terms, to account for additional background radiation caused by the ligand were also added if needed. One exemplary fitting result is depicted in Figure 8.4. The intensity data used for the temperature measurement is subsequently extracted by integrating the Voigt profile centred at the desired wavelength, in this case 639 nm.

## 8.2 FIBER CHARACTERIZATION

The setup used for the characterization of the UC-NC doped fiber thermometer is presented in Figure 8.5. A fiber coupled wavelength stabilized laser diode emitting up to 20 W with central wavelength



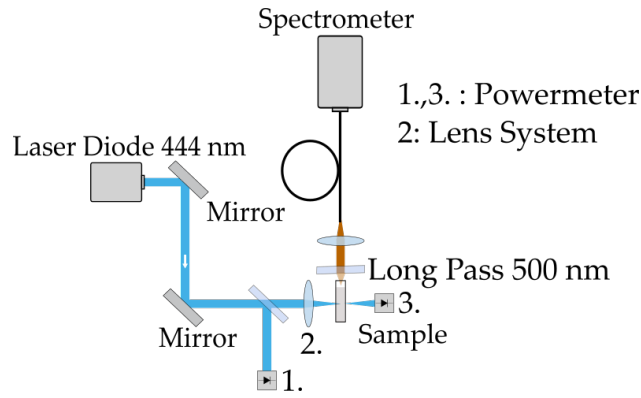


Figure 8.3: Setup used to characterize the emission variations of dispersed Pr:YLF nanocrystals under continuous excitation, with 1 and 3 marking different power meters and 2. is a lens system designed to achieve a collimated line profile of the excitation beam.

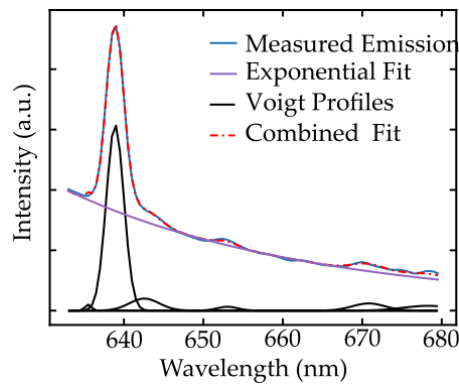


Figure 8.4: Example for an emission fit resulting from the combination of Voigt profiles and an exponential function to include the broad luminescence background.

of  $976 \text{ nm} \pm 0.5 \text{ nm}$  was used as the excitation source. The measured pump power fluctuations of below 2% were negligible because of the energy level structure of the active ions, as discussed in the previous chapters. The doped polymer fiber was butt-coupled to multimode fused silica fibers, with matching numerical apertures and core diameters to assure good coupling efficiency. The coupling efficiency from the fused silica fiber to the polymer fiber was measured to be 85%. The signal was spectrally filtered with two long pass filters, and only the fluorescence below 750 nm was detected using a fiber coupled spectrometer, with a spectral resolution of 1 nm and an integration time of 1 s.

After the detection a real time routine was applied, to fit Voigt profiles to the emission spectra. These profiles can be approximated by a linear combination of a Gaussian Function  $G(x)$  and a Lorentzian Function  $L(x)$  as discussed in Section 3.2 with

$$f(x) = (1 - \alpha)G(x) + \alpha L(x) \quad (8.1)$$

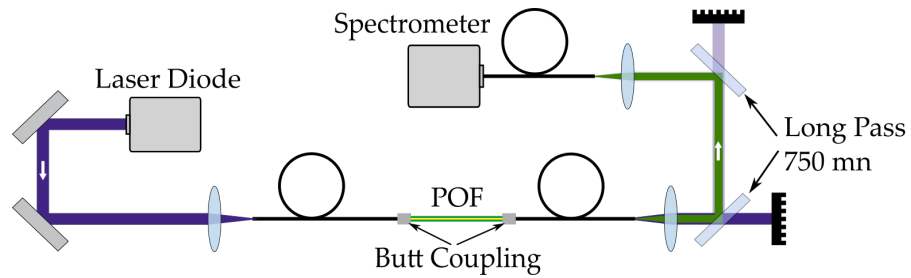


Figure 8.5: Basic setup used for the measurements of temperature dependent emission of the UC-NC doped polymer fiber.

thus allowing for a flexible adaptation to the different line-broadening mechanisms. The fiber temperatures were set to different values to

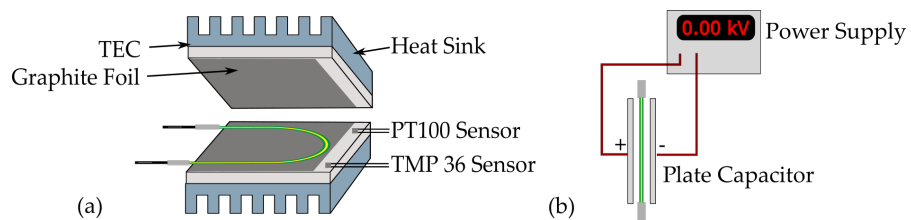


Figure 8.6: Simulated environments for the characterization of the sensor response. Influence of external temperature changes (a), where control of the sample temperature was achieved by thermoelectric cooling elements (TEC). Effects of external electrical fields on the sensor (b) were characterized by substituting the TECs with a plate capacitor

characterize the thermal response. Thermoelectric cooling elements (TEC) and a PT100 temperature sensor was used to set the temperature, similar to the dispersion characterization. Graphite foil was used as contact material to ensure a stable sample temperature, as shown in Figure 8.6a. Another electronic temperature sensor (TMP36) in combination with an arduino microcontroller was used as power supply, and an A/D converter monitored the temperature of the sample. This data was used inside the aforementioned fitting routine. The emission was measured for set temperatures between  $5^{\circ}\text{C}$  and  $40^{\circ}\text{C}$ , but applications of the sensor should not be limited to that range, as both polymer fibers and UC-NC have been successfully used outside of that range [20, 83, 94].

The influence of electric fields on the emission was also investigated to help exploit potential applications fields. The TECs were therefore replaced with a plate capacitor, as shown Figure 8.6b. With this modification electric fields of up to  $12.5\text{ kV/cm}$ , resulting in electrical flashovers, could be applied. The spectrometer was exchanged for this measurement and the emission was then measured with a resolution of  $0.5\text{ nm}$  to be able to detect even small changes.

This chapter contains the characterization of the thermometer specifications for Pr:YLF nanocrystals in a liquid dispersion. First, the baseline of the temperature induced emission variations was measured, as described in section 8.1. Emission spectra were recorded at 5 °C and 35 °C, as shown in Figure 9.1a. Higher temperatures shift the emission intensity to the green emission centered around 522 nm corresponding to higher photon energy levels, as expected. A first selection of the analysed emission lines was made based on the emission spectra collected from bulk Pr:YLF, shown in Figure 9.1, with the emission strength relative to the background as main criterion. Besides that, spectral separability of the desired emission from other peaks is also desired, because it further assures correct measurement. Based on this set of

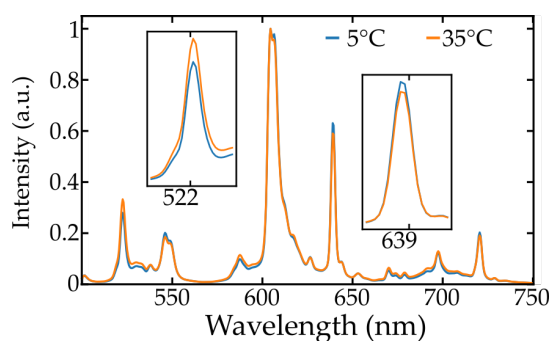


Figure 9.1: Temperature dependent emission of a Pr:YLF bulk crystal measured at 5 °C and 35 °C.

requirements the emission lines centred at 522 nm, 639 nm and 720 nm, respectively, were chosen for the conducted temperature measurements. The strongest emission centred at 607 nm was excluded from further evaluation, because the spectral shape of this peak, caused by an overlap of different emissions lines, aggravates the numerical fitting.

Therefore, the results presented in the following sections are all based on the aforementioned emissions lines. The thermal sensitivity and the temperature resolution achievable with Pr:YLF nanocrystal dispersions were acquired using pulsed excitation. This was followed by an assessment of the influence of continuous pumping on the temperature measurement and the determination of the laser induced heating rate. Lastly an application of the recalibration routine, presented in Chapter 5.2.2, is provided for the obtained measurements.

## 9.1 SENSITIVITY AND TEMPERATURE RESOLUTION

Two different nanocrystal dispersions were used to measure the FIR baseline. The main difference between the samples was the varying nominal doping concentrations of 0.65 at% and 2 at%, whereas the volume percentage of nanocrystals inside the solution was the same. The results are shown in Figure 9.2. Both samples show tempera-

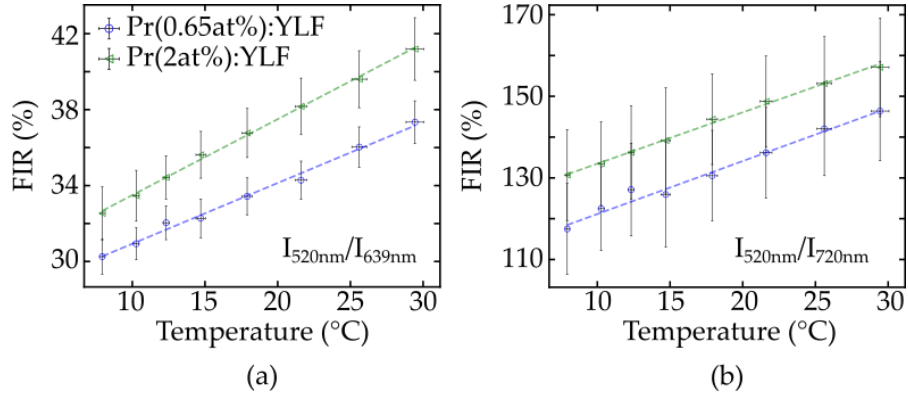


Figure 9.2: Ratio of the emission intensities of the lines 522 nm and 639 nm in (a) and 522 nm and 720 nm in (b), both shown for two different samples with varying doping concentration.

ture dependent emission changes with slightly varying base levels of  $\text{FIR}_0$ , especially for the ratio of the emissions 522 nm and 639 nm. One reason for this may be the luminescence background caused by the ligand system, which is stronger around 639 nm compared to 720 nm. Therefore, the emission at 639 nm is affected differently by the background compared to the two other peaks as shown in Figure 7.5a. The

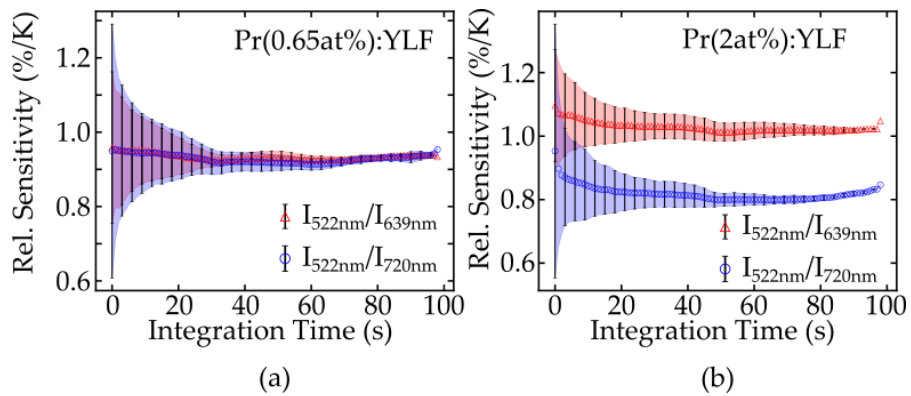


Figure 9.3: Dependence of the relative sensitivity of different Pr:YLF nanocrystals on the integration time.

relative sensitivity of the nanothermometers, as shown in Figure 9.3 is determined depending on the integration time to be approximately 0.8–1.1%/K, which is in accordance to previously reported values [22, 54]. The deviation between the sensitivities can again most likely be

attributed to the luminescence background and its varying effect on the different emission lines. The absolute value of the sensitivity does not depend on time as expected, however the signal-to-noise ratio increases for longer sampling times leading to a reduced measurement uncertainty for longer integration times. The temperature on the other hand strongly affects the sensitivity, as depicted in Figure 9.4, and an exponential decrease of the sensitivity can be observed. Building on these sensitivity values, the temperature resolution at

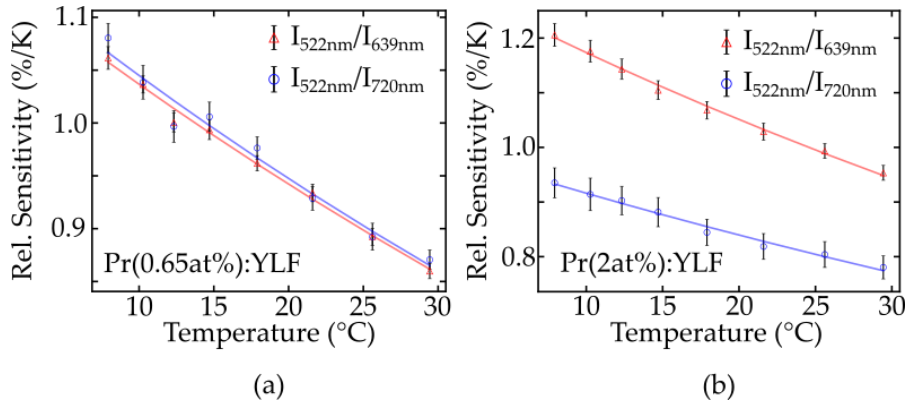


Figure 9.4: Dependence of the relative sensitivity of different Pr:YLF nanocrystals on the temperature.

room temperature was then determined by including the measurement uncertainty  $\Delta\text{FIR}$ . Therefore, an influence of the integration time on the temperature resolution is to be expected. The corresponding curves are depicted in Figure 9.5. For short integration times or low averaging rates, the temperature resolution is approximately 2 K–5 K for both samples. Because of the relatively stronger emission at 639 nm compared to 720 nm, the intensity relation  $I_{520\text{ nm}}/I_{639\text{ nm}}$  has a larger signal-to-noise ratio and with that an improved temperature resolution. This does not change, if the integration time is increased and the temperature resolution for both FIRs is optimized for longer integration and values below 0.4 K were achieved.

## 9.2 CONTINUOUS WAVE PUMPING

Additional experiments were carried out with continuous excitation to estimate the influence of laser induced heating. The first observation was the increase in luminescence background, as depicted in Figure 9.6a.

### 9.2.1 Laser induced Heating Effects

This could be due to the change of the pumping regime, but could also be attributed to an increased oxidation of the oleic acid ligand compared to the previous measurements. Still, the normalized spectra

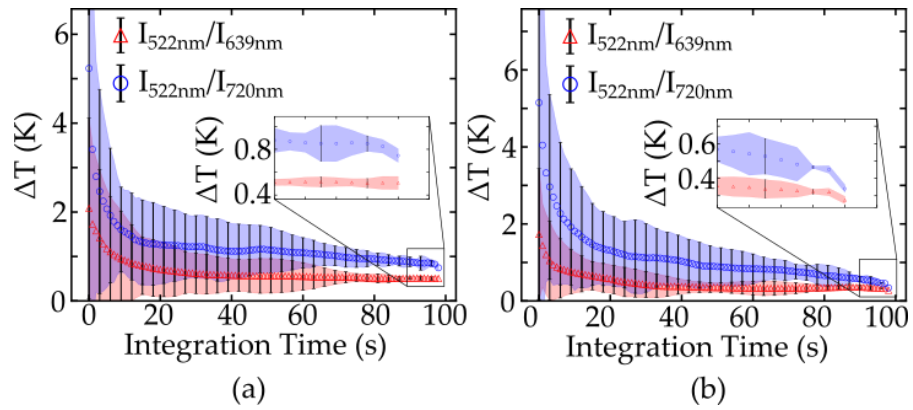


Figure 9.5: Temperature resolution for different Pr:YLF nanodispersions for different integration times.

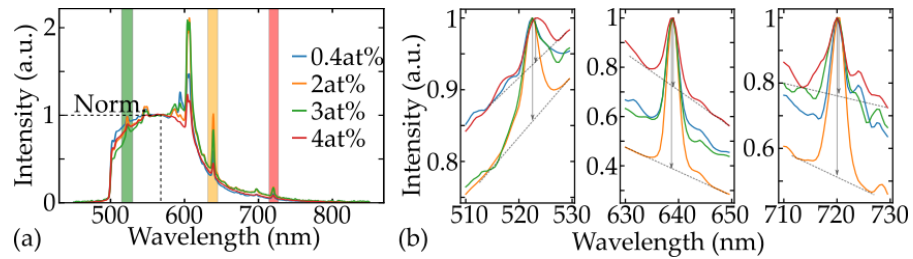


Figure 9.6: Normalized emissions spectra of different Pr:YLF dispersions (a) and a qualitative comparison of the signal-to-noise ratio of the different samples.

show no major difference in the spectral shape of the background emission. The main difference between the samples with different doping concentration is the signal-to-noise ratio, exemplary defined by the intensity difference of an emission peak and the underlying background, as seen in Figure 9.6b.

The dispersion containing Pr(2 at%):YLF nanocrystals offers the highest emission intensity and Pr(4 at%):YLF the lowest. The samples with Pr(0.4 at%):YLF and Pr(3 at%):YLF show intermediate signal levels, hinting at a local optimum of the emission efficiency of the nanocrystals around 2 at% doping.

The samples also vary in the degree of oxidation, which affects the luminescence background, as previously mentioned. One qualitative way of accessing the oxidation inside the sample is the measurement of the corresponding discolouration. This was done by placing the samples in front of a neutral background, taking pictures and analysing the color values of the pixels. The results are shown in Figure 9.7 for the four samples and the values were calibrated using the  $x,y$ -coordinates of the CIE colorspace [95]. Besides the resulting temperature measurements, the oxidation of oleic acid has additional implications as it may influence the absorption and with that the laser induced heating. Therefore, in the next step, the FIR was measured

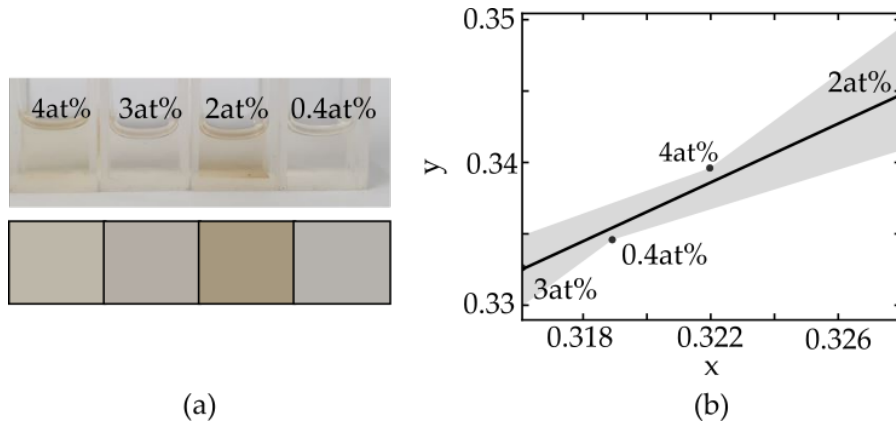


Figure 9.7: Qualitative characterization of the degree of oxidation of the different samples, based on their discoloration. The coordinates  $x$  and  $y$  are defined according to the CIE colorspace [95].

depending on the absorbed pump power for a constant excitation wavelength. The results are depicted in Figure 9.8 for the two emission ratios  $I_{520\text{ nm}}/I_{639\text{ nm}}$  and  $I_{520\text{ nm}}/I_{720\text{ nm}}$ . The correlation between FIR

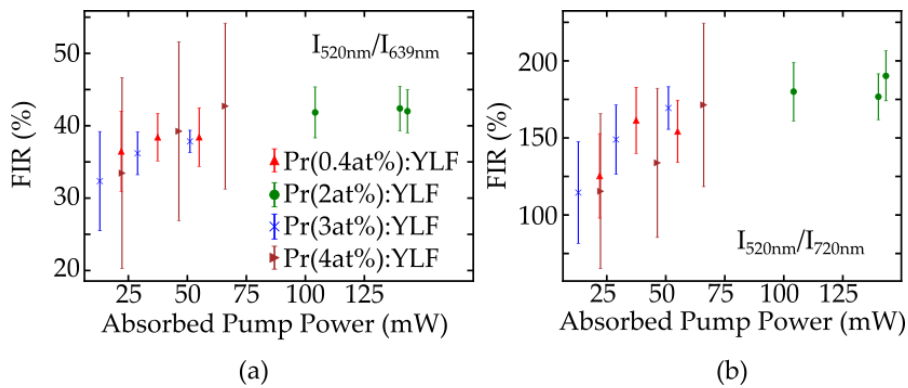


Figure 9.8: FIR depending on the absorbed pump power for the two characterized emission ratios in (a) and (b)

and absorbed pump power should mainly be governed by the quantum defect of nanocrystals and additional absorption mechanisms in the host material or the ligand system. Therefore, the variations of the FIR should not depend on the doping concentration. This assumption is justified, if the efficiency of non-radiative transitions is assumed to be equal for the involved energy levels  $^3P_0$  and  $^3P_1$  at any given doping concentration. In this case the non-radiative transitions only affect the signal-to-noise ratio, which is in accordance to the previously shown data on emission efficiency, seen in Figure 9.6.

Following this argument, the values for 0.4 at%, 3 at% and 4 at% overlap with variations due to the differing signal-to-noise ratio, as depicted in Figure 9.8. The 2 at% sample however, shows a significantly increased absorption and higher FIR and is an outlier for both intensity ratios. The influence of non-radiative transitions inside the

nanocrystals offers no explanation for this effect, because the emission efficiency should be maximal around approximately 2 at% leaving only minimal energy to heat conversion, as discussed earlier. The oleic acid remains as the cause of this deviation and this can be further confirmed by a comparison between absorption and discolouration.

### 9.2.2 Calibration of Temperature Measurements

The previously obtained FIR values were converted to temperature differences by using the sensitivity measured with pulsed excitation. The doping concentration was neglected for this evaluation, as the FIR measurement indicates no clear correlation between doping and temperature increase. The resulting temperature differences  $\Delta T$  are shown in Figure 9.9. In this first assessment the temperature increase

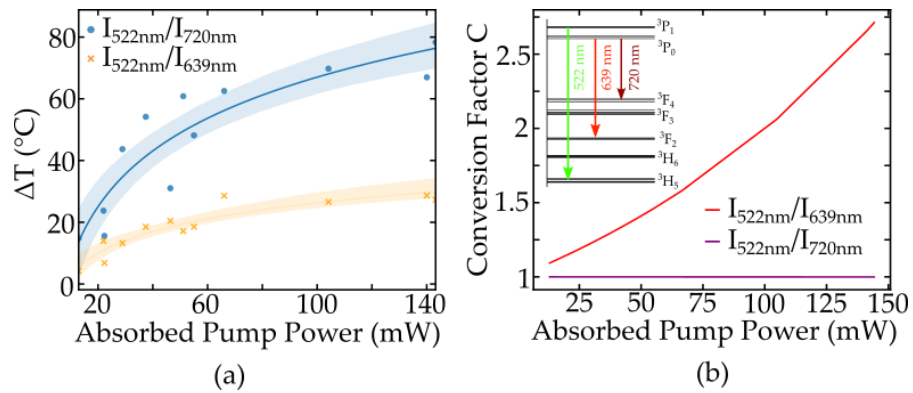


Figure 9.9: Temperature depending on the absorbed pump power in (a) and conversion factor also depending on the absorbed pump power (b).

strongly depends on the utilized intensity ratio with maximum values of approximately 80 °C for  $I_{520\text{nm}}/I_{720\text{nm}}$  and roughly 30 °C for  $520\text{nm}/I_{639\text{nm}}$ . As described in the earlier sections, this deviation could be caused by differences in the lower lying energy levels and a non-negligible lifetime of these energy levels. Therefore, conversion factors were derived using the described formalism for both transitions  $^3P_0 \rightarrow ^3F_2$  and  $^3P_0 \rightarrow ^3F_4$ . The lifetimes for the lower levels were assumed to be 58  $\mu\text{s}$  for  $^3F_4$  and 125 ms for  $^3F_2$ , corresponding to reported values for Pr:LaF<sub>3</sub> [58] and Pr:YLF [96], respectively. The calculated conversion factors are depicted in Figure 9.9b and a much stronger influence of reabsorption for the intensity ratio  $I_{520\text{nm}}/I_{639\text{nm}}$  can be observed with the reason being the relative populations and the respective absorption cross section.

Applying the conversion factor to the FIR measurements yields new temperature values, as depicted in Figure 9.10 and now both curves show a temperature increase of roughly 75 °C. Additionally the absorbed pump power was also corrected to exclude the influence of



ligand absorption, which cannot be precisely included in the recalibration algorithm. In a simplified approach, absorption values of the 2 at% sample was reduced an approximated value of 20%. However, this last recalibration step yields no major changes in the estimated temperature as the values seem to be saturated.

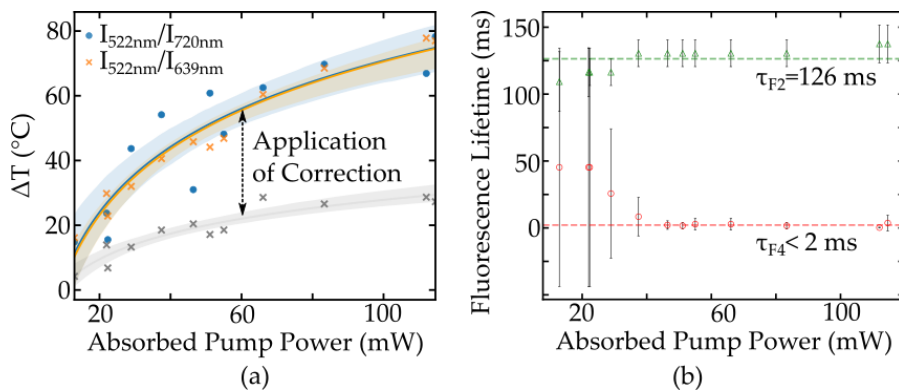


Figure 9.10: Measured Temperature increase corrected by numerically including the reabsorption of fluorescence (a) and tolerance range for the lifetime of the lower laser levels (b).

In the last step, a tolerance range for the lifetimes of the energy levels  $^3F_2$  and  $^3F_4$  was calculated, because the lifetime values extracted from the literature cannot directly be transferred to nanocrystal lifetimes. The acceptance range for lifetimes is much larger for low pump power as expected yet the accepted values for the two levels for higher pump powers are 126 ms and below 2 ms. Therefore the tolerance range of the conversion factor shows good agreement with the reported literature values of 125 ms for  $^3F_2$  and 58  $\mu$ s for  $^3F_4$ .

### 9.3 CONCLUSION PR:YLF DISPERSION MEASUREMENTS

The aim of this chapter was to show the application of dispersed Pr:YLF nanocrystals as nanothermometers, since liquid dispersions are the most commonly used form in nanothermometry measurements. These nanothermometers offer a high sensitivity as well as an efficient excitation, as expected from the energy level scheme. A comparison to other nanocrystals in terms of sensitivity and spectral position of the transitions, is listed in Table 9.1.

However, some disadvantages of dispersed nanocrystals were also revealed. The most prominent one is the low signal-to-noise ratio. Due to this, the temperature resolution measured in this work was limited to be 0.4 K even in presence of the high sensitivity. One reasons for this is the luminescence background, which in this case cannot be completely suppressed, because the excitation wavelength of  $\text{Pr}^{3+}$  and the oleic acid ligand overlap. Therefore, the background can only be

Table 9.1: Comparison between different nanocrystals and their specifications in nanothermometer measurements.

Material	Excitation Wavelength	Signal Wavelength	Sensitivity (%/K)	Source
Pr:YLF	444 nm, 480 nm	520 nm-720 nm	0.8-1.1	This work
Nd:YAG	808 nm	938 nm, 940 nm	0.15	[21]
Er,Yb:YNaF	920 nm	525 nm, 545 nm	1.2	[20]
Ho,Yb:GdNaF	640 nm	974 nm, 1181 nm	2	[97]

minimized by preventing the oxidation of the samples during the synthesis.

Another reason for the low signal-to-noise ratio can be found in the measurement approach itself, as dispersion measurements offer only a short interaction length and only negligible light guiding. The amount of collected signal therefore strongly depends on the numerical aperture of the measurement system. Both of these restrictions can be addressed by doping nanocrystals inside a host material with light guiding properties, such as fibers or waveguides, as presented in the following chapter.

ER,YB:YNAF DOPED POLYMER FIBER  
THERMOMETER

In this chapter, the performance of the UC-NC doped polymer fiber thermometer is characterized and again, the obtained specifications are presented. First, the temperature dependent emission characteristics were measured and a calibration range was determined. After that, the sensitivity and temperature resolution were calculated for different pump powers. The last sections include experiments and simulations, which help to identify possible applications of the the sensor for example in the presence of external fields.

A doped polymer fiber was set to different temperatures in a range of 13–35 °C to obtain the temperature dependent FIR values. Three exemplary emission spectra and their temperature dependences are shown in Figure 10.1a. A blue shift of the integrated emission intensity

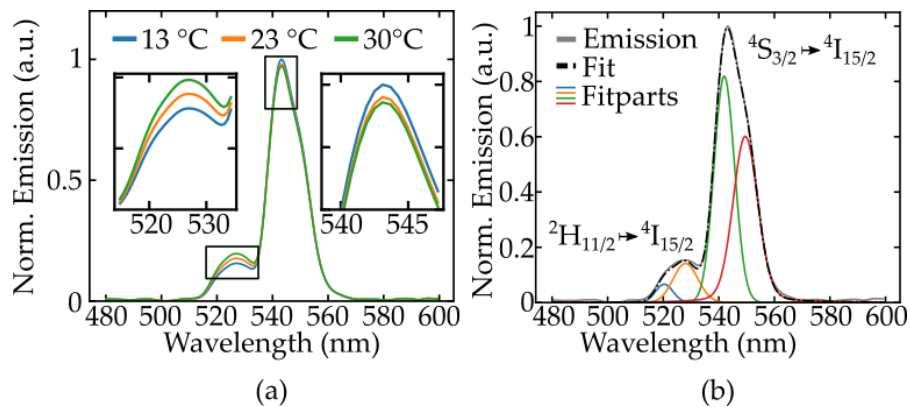


Figure 10.1: Temperature dependence of the fluorescence emission of an excited polymer fiber in (a) and exemplary fits to assign the emission lines to electronic transitions in (b).

can be observed, as expected from the energy level diagram shown in chapter 7.2.1. This shift is quantified by assigning electronic transitions to the emission peaks through fitting of Pseudo-Voigt profiles, as depicted in 10.1b. The main energy level transitions responsible for the two emission lines are  ${}^2H_{11/2} \rightarrow {}^4I_{15/2}$  and  ${}^4S_{3/2} \rightarrow {}^4I_{15/2}$  of  $\text{Er}^{3+}$  centered around 525 and 545 nm, respectively. The following analysis of the fiber thermometer is based on these measurement, if not otherwise stated.

## 10.1 SENSOR CALIBRATION

All measurements were carried out multiple times at different pump power levels, because the absorption of the pump laser, especially in the host polymer, also leads to intrinsic heating and with that to variations of the emission. The baseline measurements necessary for the sensitivity calculations were therefore performed at 90 mW, 162 mW, and 234 mW of absorbed pump power, respectively. The temperature for each of those measurements was externally controlled, as described in the corresponding section 8.2. The results of these baseline measurements are given in Figure 10.2. A linear dependence

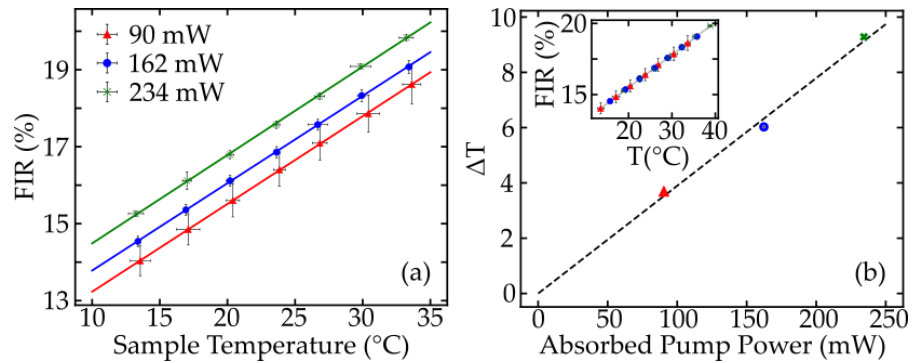


Figure 10.2: Baseline measurements of FIR. Depicted in (a) is the temperature dependence of the FIR for different pump powers and in (b) linear interpolation of the temperature shifts inside the fiber due to intrinsic heating effects.

of the FIR on temperature is visible in Figure 10.2a, as expected. Applying linear regression yields the slope  $d\text{FIR}/dT$  for all pump powers with a high fit quality of  $R^2 > 0.99$ . The slope of the FIR is equivalent to the absolute sensitivity of the thermometer and the value of  $S_a \approx 2.3\% / \text{K}$  is found to be pump power independent.

The absolute value of the FIR measured nominally at room temperature of approximately  $22^\circ\text{C}$ , varies with the pump power indicating an offset in the internal temperature of the fiber. This absorption induced heating can be approximated by assuming  $\Delta T$  of temperature difference without pump power and again applying linear regression, as shown in Figure 10.2b. The temperature offset can be calculated to be 10 K relative to the sample for the maximum value of applied pump power. The longitudinal temperature distribution inside the fiber is assumed to be homogeneous, which is justified for either weakly doped or short fibers, because, for these fibers, absorption can be linearly approximated [60]. For example, at an absorption rate of 6.7 dB/m, approximately 2.5% of pump power is absorbed per centimetre propagation inside the fiber. This means only minor variations in the amount of absorbed pump power between, e.g., the first length

increment of the fiber and the last, which, combined with heat flux inside the fiber, justifies the assumption.

Still, the need for a calibration of the sensor is apparent from these measurements, since the value of  $FIR_0$  directly influences the relative sensitivity. For a valid calibration it has to be determined whether the  $FIR_0$  only depends on the pump power and if a steady state temperature is reached for any given pump power values. The temporal evolution of the FIR was therefore measured depending on absorbed pump power and the results are depicted in Figure 10.3. The heat

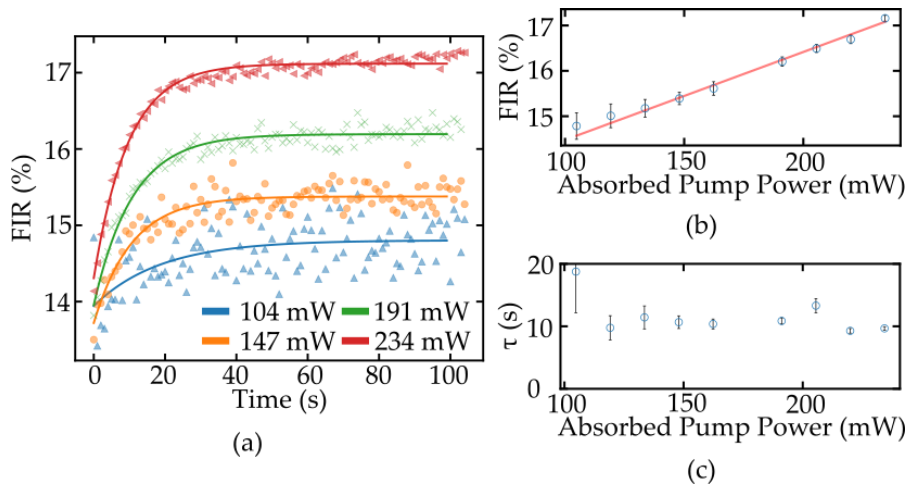


Figure 10.3: FIR of the UC-NC doped polymer fiber Thermometer measured at different absorbed pump powers. Response after the pump laser is turned on (a) equilibrium levels (b) and time constant until the equilibrium is reached (c).

control was turned off for this measurements, therefore the shown variations of the FIR directly correspond to a pump light induced heating of the fiber and the time dependent temperature rise is given in Figure 10.3a. The improved signal-to-noise ratio at higher pump powers, due to stronger fluorescence emission, is also visible from the reduced scattering of the obtained values. All of the FIR curves start at values of approximately 14%, which identifies this as the FIR at room temperature. A state of thermal equilibrium inside the fiber is reached after 40 s-60 s for all pump powers. The corresponding values of the FIR are plotted in Figure 10.3b, where the linear correlation of the pump power to fiber temperature again is visible, comparable to Figure 10.2. To further quantify the temporal behaviour, exponential functions were fitted to the data, and the  $1/e$  time constant was calculated to be approximately 10 seconds, as shown in Figure 10.3c.

The influence of the fiber temperature on the sample temperature can be estimated by comparing the FIR values at nominal sample temperature of  $21^\circ\text{C}$ , Figure 10.2a, with the equilibrium values without external temperature control, Figure 10.3b. For example, both figures show an FIR of roughly 17% at an absorption level of 234 mW. Since

both measurements were performed at the same pump power, the only difference is the sample temperature, which translates to the room temperature plus the temperature change caused by additional heat input through the fiber, in the case of the unregulated sample. The influence of the fiber heating on the sample temperature can therefore be narrowed down to 0.5 K-1 K for the maximum value of pump power. Therefore, the heat dissipation inside the sample seems to be fast enough, and the influence of the fiber on sample temperature is negligible. The temperature sensitivity depends on  $FIR_0$  and the absolute sensitivity  $dFIR/dT$ , which is constant for different pump powers, as mentioned before. The assumption that sample heating only creates an offset in the thermometer signal, seems to be valid, and intrinsic heating can be addressed by calibrating the sensor. Following this, the total range of the measured values was used for the calibration range, as shown in 10.4a.

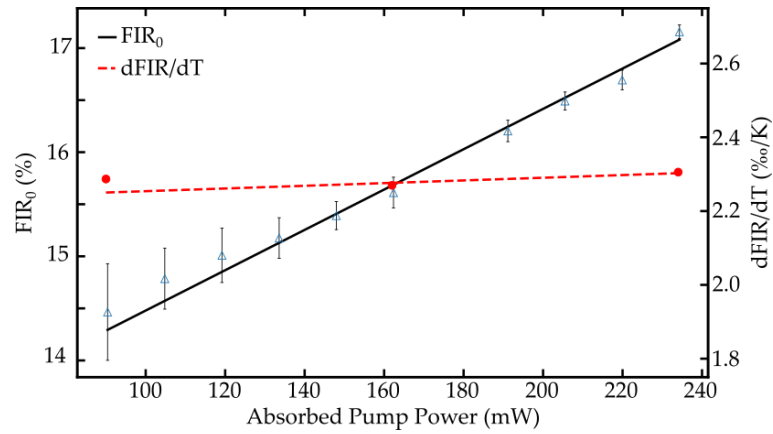


Figure 10.4: Calibration range of the polymer fiber thermometer.

Transversal variations of the fiber temperature can also cause measurement errors and are not as easily accessible as the longitudinal temperature gradient due to a lack of material parameters. However, the experimentally determined linear correlation between fiber temperature and absorbed pump power can also be used to numerically identify material constants, by using equations presented in [60]. Among the most important parameters are the thermal conductivity  $k$  and a coefficient for the surface temperature transport  $h$ . Especially the value of  $h$  varies with material composition and surface quality of the fiber and is therefore hard to access experimentally. Because of this, a fitting function was applied to the temperature values derived in Figure 10.2b. The fitting function

$$T_{av} = T_c + \frac{Q_0 a^2}{2k} + \frac{Q_0 a^2}{2bh} - \frac{Q_0 a^2}{3k} \quad (10.1)$$

is used to calculate average temperatures inside a fiber [60] with the geometrical parameters, as shown in Figure 10.5. Even though the

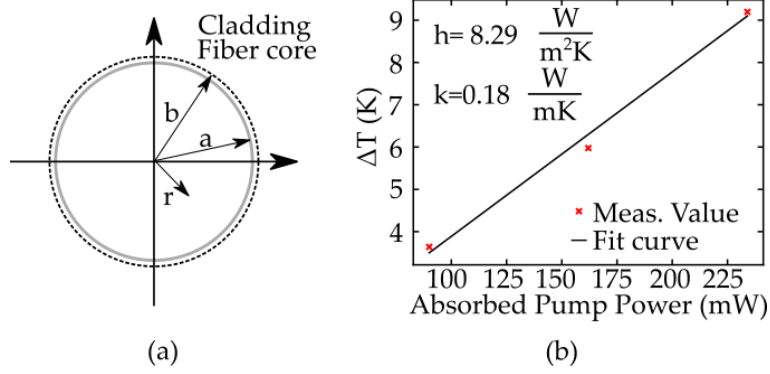


Figure 10.5: Model of a fiber consisting of a core and a cladding with the radii  $a$  and  $b$ , respectively in (a). Linear fit of the average fiber temperature and estimation of the parameters for thermal conductivity  $h$  and surface temperature transport  $k$  (b).

validity of the fit is restricted due to the sample size, the calculated values for  $h=8.29 \text{ W/m}^2\text{K}$  and  $k=0.18 \text{ W/mK}$  are in good agreement with literature values for comparable fiber types [60, 98]. The longitudinal temperature distribution is homogeneous, as mentioned before, and using these coefficients, the transverse temperature distribution can now be calculated with the equations [60]

$$T_{core}(r) = T_c + \frac{Q_0 a^2}{4k} \left( 2 \ln \left( \frac{a}{b} \right) + \frac{2k}{bh} \right) + \frac{Q_0 a^2}{4k} \left( 1 - \left( \frac{r}{a} \right)^2 \right) \quad (10.2)$$

and

$$T_{cladding}(r) = T_c + \frac{Q_0 a^2}{2bh} - \frac{Q_0 a^2}{2k} \ln \left( \frac{r}{b} \right). \quad (10.3)$$

The results of these calculations are presented in Figure 10.6. A temperature increase of roughly 80 K caused by 2 W of absorbed power would lead to an absolute temperature value of  $100^\circ\text{C}$ , and therefore exceed the feasible temperature range of the host polymer. The

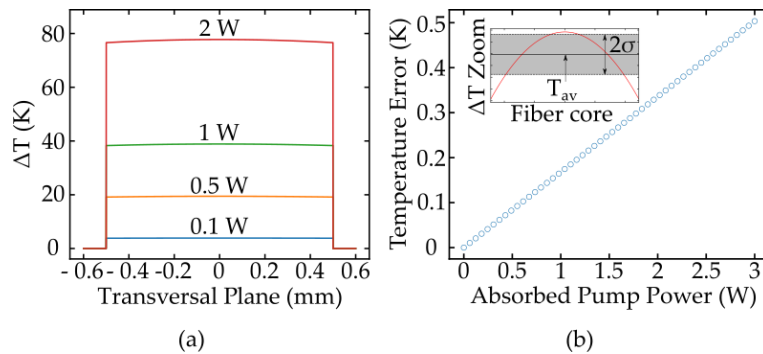


Figure 10.6: Transversal temperature distribution inside the fiber (a) and temperature error due to the calculated temperature profile e.g. for 2 W of absorption (b).

amount of absorbed pump power affects the fiber performance beyond

material degradation. A transverse temperature profile can lead to a temperature error, as different nanocrystals are subjected to different local temperature. The amplitude of this internal transversal temperature gradient is depicted in Figure 10.6. Low values of pump power lead to small temperature gradients and a reduced temperature error, as expected. However, the signal-to-noise ratio is also reduced for these excitation regimes which in terms increases the measurement uncertainty. Therefore, the right choice of pump power is crucial to balance the accuracy of the measurement and tolerable heat input to the system.

In terms of the calibration range the transversal temperature profile yields an error of below 0.3 K even at pump levels that would result in a destruction of the polymer fiber sensor, as shown in 10.6b. Still, this calculation hint at a minimum limit for temperature resolution even at lower pump powers with values e.g. for 500 mW of absorption corresponding to 100 mK resolution. The actual resolution value should exceed this numerical result, as the influence of the signal-to-noise ratio needs to be factored in, as described in the following section.

## 10.2 SENSITIVITY AND TEMPERATURE RESOLUTION

The next step for the validation of the sensor is the determination of the sensitivity, as defined in chapter 5. The previously determined values of the FIR and  $d\text{FIR}/dT$  are decisive for this and the resulting sensitivity is shown in Figure 10.7. The results range from 1.37 %/K

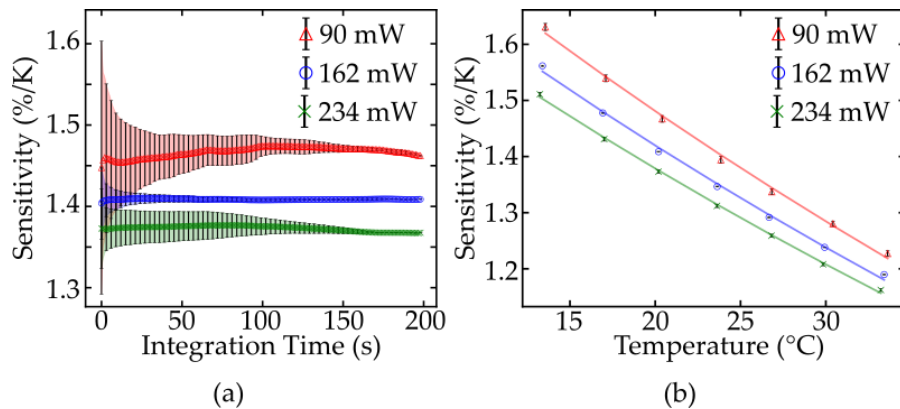


Figure 10.7: Sensitivity of the UC-NC doped fiber sensor depending on integration time (a) and temperature (b).

to 1.45 %/K at absorbed pump powers values of 234 mW and 90 mW, respectively. The observed difference in sensitivity is a consequence of the temperature increase inside the fiber. This correlation is also depicted in Figure 10.7b by the sensitivity values at different nominal sample temperatures. As depicted, there are only minor influences of the integration time on the absolute value of the sensitivity, as expected from the corresponding formula. Contrary to that, the temperature res-



olution is heavily affected by the signal-to-noise ratio and therefore the integration time. This correlation can be seen by the progression of the curves in Figure 10.8a. For short integration times, the signal-to-noise

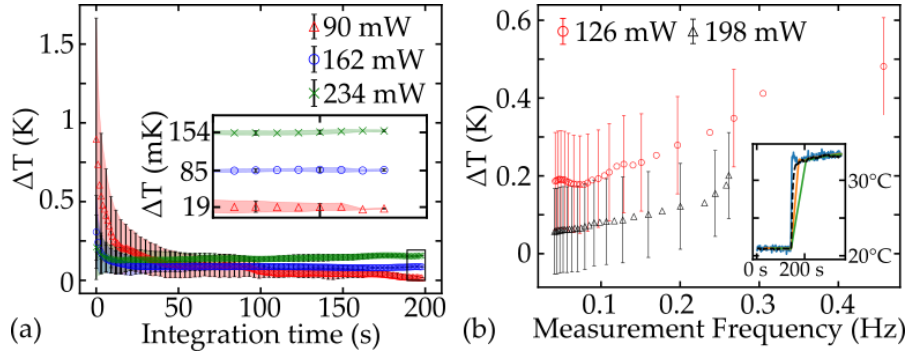


Figure 10.8: Temperature resolution  $\Delta T$  as a function of integration time (a) and measurement frequency as measured by a step response (b).

ratio obtained at high pump powers prevails the reduced sensitivity, and the optimal resolution of approximately 0.25 K is reached for the highest pump power. In comparison to that, the resolution for the minimum pump power and a short integration time is  $\approx 1$  K. The signal-to-noise ratio gradually improves for longer integration times. This leads to an increase in the temperature resolution for all pump powers with the final values of 200 s of 19 mK, 85 mK and 154 mK for the pump powers 90 mW, 162 mW and 234 mW, respectively. Comparing these values to the numerically obtained error margins, presented in the previous section even hints at further optimization potential by taking additional measures to enhance the signal-to-noise ratio.

The consequence of the temporal evolution in terms of applications is that low pump powers should be used in environments with slowly varying temperatures, whereas high pump powers are desirable for robust samples with quickly changing temperature. Further investigations were carried out, specifically on fast temperature variations by measuring a step response, as depicted in the inset of 10.8b. Different moving averages were used to evaluate the temperature resolution by comparing the sensor read out value with a reference signal that was electrically measured. The resulting settling time was converted to the depicted measurement frequency. This analysis shows that temperature resolutions of 0.5 K can be maintained even at temperatures oscillating with 0.4 Hz.

In conclusion to this section, Table 10.1 shows the results for sensitivity and temperature resolution compared to different sensors based on passive polymer fibers [94] and Er,Yb:YNaF NTs [83]. This comparison highlights that especially the temperature resolution benefits from the combination of the both approaches, the high sensitivity of nanothermometers and the excellent signal-to-noise ratio of fiber based measurements caused by their light guiding character.

Table 10.1: Comparison of different temperature sensors.

	UC-POF	Er,Yb:YNaF NTs [20, 83–85]	POF Sensors [94, 99, 100]
Sensitivity (%/K) Temperature	1.45	1.2–1.1	0.192–0.104
Resolution (mK) Temperature	19	83	–
Range (°C)		–50–210	–55–70

### 10.3 INFLUENCE OF FIBER DIMENSIONS

The geometrical dimensions of a fiber play an important role in the optical characteristics as well as the applications ranges. For example, the absorption scales with the fiber length and the number of supported modes depends on the numerical aperture and therefore the fiber radius among other things. In terms of the fiber thermometer, the fiber length can be expected to be more important, as light guiding and interaction length is the main reason for the improved temperature resolution of the UC-NC polymer fiber compared to other applications of dispersed UC-NC.

For this reason, the emission was measured for different fiber lengths between 13 and 6 cm. The fluorescence emission was then interpolated using the equation

$$P(z) = \frac{C}{\alpha}(1 - \exp(-z\alpha)) \quad (10.4)$$

which is used to describe spontaneous emission intensity along a fiber [101]. The parameters are  $\alpha$  for the wavelength dependent attenuation,  $C$  as a measure for spontaneous emission, and  $z$  for the fiber length. The corresponding spectra are shown in Figure 10.9a. The standard evaluation of the FIR, consisting of fitting followed by an integration, was then conducted for all curves and the resulting fit error was calculated. The result of these calculations is that the fiber length could be reduced to 2.5 cm without a major temperature error. However, additional steps such as an increase in pump power may even further push this border.

### 10.4 INFLUENCE OF EXTERNAL FIELDS

Monitoring temperature in the presence of external fields is a challenging task for most available thermometers e.g. the commonly used Pt100. Optical thermometers on the other hand, should be mostly insensitive against such fields and this section aims to investigate this robustness against the influence of external electric and magnetic

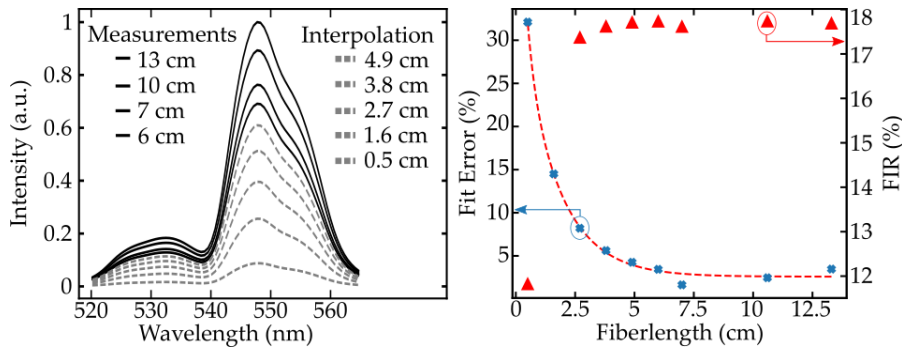


Figure 10.9: Fluorescence emission for different fiber lengths via measurement and interpolation (a) and estimation of the fit error caused by the reduced signal-to-noise ratio for shorter fiber lengths.

fields with experimentally measurements and numerically estimations, respectively.

10.4.1 Electric Fields

The applicability of the UC-NC polymer fiber thermometer inside an electric field was investigated by placing the fiber inside a plate capacitor, as described in Chapter 8.2. The emission was the measured for different applied voltages. The corresponding field strength ranges from 0 kV/cm to 12.5 kV/cm. At the highest values the emission was monitored even during multiple discharges. The resulting fluorescence spectra are depicted in Figure 10.10a for different electrical field strengths. The physical relations between external electric field and

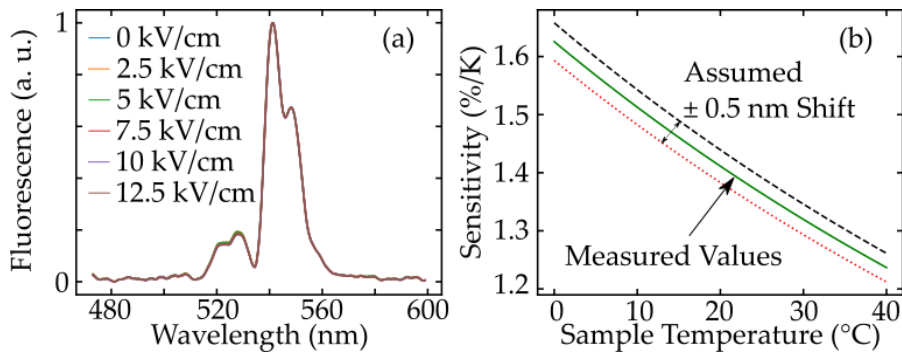


Figure 10.10: (a) Normalized fluorescence of a Er,Yb:YNaF POF exposed to different electrical fields and (b) assessment of the variation of the sensitivity change that follows a 0.5 nm shift of the emission lines.

energy level distribution are described by the Stark effect [46] and deviations that could be anticipated are the onset of new peaks followed by a shift in the emission shape or a relative spectral shift of the emission lines relative to one another. None of these deviations are visible from the normalized emission, seen in 10.10, and tempera-

ture measurement with the fiber sensor as described earlier are still possible in the presence of electric fields.

This measurement proves the absence of a susceptibility to electric fields with an amplitude higher than the spectrometer resolution of 0.5 nm. Shifts of the energy gap  $\Delta E$  causing smaller emission changes than 0.5 nm are still possible. Therefore, the sensitivity deviation resulting from a positive and negative shift of the emissions was calculated with [22]

$$S = \frac{\Delta E}{k_B T^2}. \quad (10.5)$$

The results, shown in Figure 10.10b, are the maximal possible errors that could be missed due to the spectrometer resolution. The sensitivity ranges from 1.38 %/K to 1.44 %/K, for shifts corresponding to -0.5 nm and 0.5 nm, respectively. If a linear correlation is assumed this leads to an error coefficient of approximately 50 ppm (kV/cm). This calculation again demonstrates that highly sensitive temperature measurements are still feasible even inside strong electric fields.

#### 10.4.2 Magnetic Fields

Magnetic fields are the second external perturbation, besides the electric field, that are be present in many applications, from batteries to medical examinations. The investigation of the sensitivity of the fiber thermometer to such fields was performed by a numerical analysis.

Generally, the splitting of energy levels in the presence of magnetic fields is described by the Zeeman effect [32] or the Paschen-Back effect [46] for weak or strong magnetic fields, respectively. Further divisions can be made depending of the quantum number  $s$  with the normal Zeeman effect for  $s=0$  and the anomalous Zeeman effect for  $s \neq 0$ . The degree of splitting is determined the angular momentum and energy levels split into a maximum of  $2L+1$  sub-states, again denoted by quantum number  $m$ . This splitting is illustrated for two arbitrary energy levels and the normal Zeeman effect in Figure 10.11. The corresponding energy shift  $\Delta E$  of a single sublevel  $j$  is given by

$$\Delta E = g_j m_j \mu_B B \quad (10.6)$$

and depends on the field strength  $B$ , the Bohr magneton  $\mu_B$  the Landé factor [46]

$$g_j = 1 + \frac{j(j+1) + s(s+1) - l(l+1)}{2j(j+1)}. \quad (10.7)$$

As mentioned earlier, nanothermometry measurement depend on the spectral separability of two emission levels originating from different energy levels, as described in Chapter 5. The magnetic fields  $B_{\max}$  that causes an overlap of the lowest and highest Stark levels of the two laser levels can be seen as limitation and the corresponding

$$B_{\max} = \frac{\Delta E}{(g_1 m_1 - g_2 m_2) \mu_B} \quad (10.8)$$

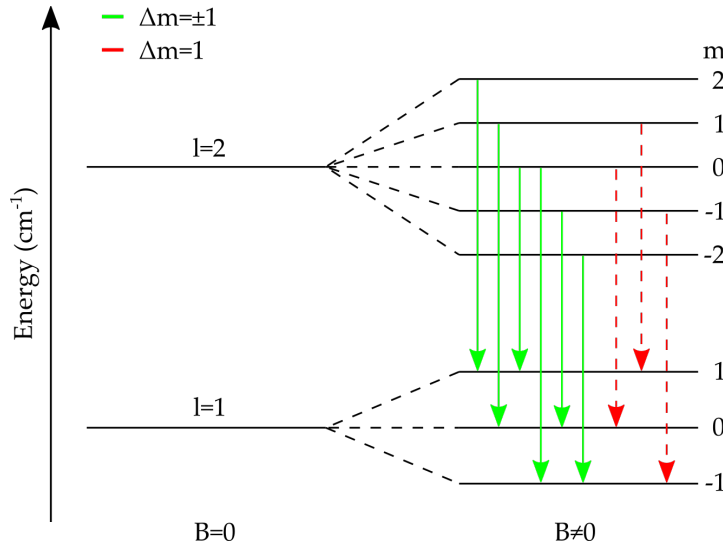


Figure 10.11: Schematic energy level splitting caused by the normal Zeeman effect and allowed optical transitions.

can be derived from Equation 10.6 [62].

Thus, this equation is used to calculate the feasibility of a nanothermometer measurements inside an external magnetic field by estimating the spectral separability of emission lines for the case of  $\text{Er}^{3+}$ . The spectral distance of the emission lines, corresponding to the transitions  ${}^4\text{H}_{11/2} \rightarrow {}^4\text{I}_{15/2}$  and  ${}^4\text{S}_{3/2} \rightarrow {}^4\text{I}_{15/2}$  transitions of  $\text{Er}^{3+}$  is plotted over the magnetic field strength in Figure 10.12.

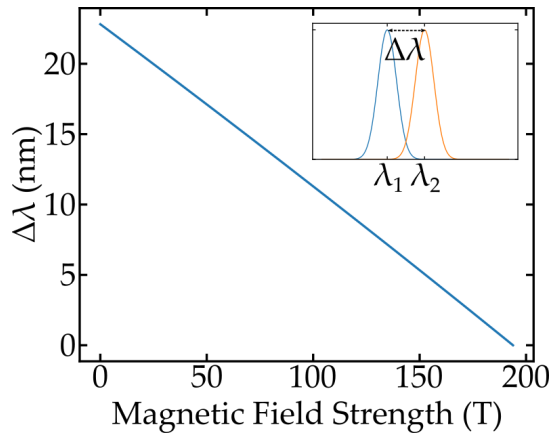


Figure 10.12: Influence of the magnetic field strength on the spectral distance of two Stark levels approximately corresponding to the transitions  ${}^4\text{H}_{11/2} \rightarrow {}^4\text{I}_{15/2}$  and  ${}^4\text{S}_{3/2} \rightarrow {}^4\text{I}_{15/2}$  of  $\text{Er}^{3+}$ .

As is shown, the magnetic field, resulting in a overlap of the depicted emission lines is 200 T. The maximal magnetic field value tolerable in a measurement additionally depends on the instrument resolution and the non-negligible line width of the emission lines.

In the case of the fiber thermometer the spectral resolution limit of the two emission lines were assumed to be the half of their linewidth

combined with the spectrometer resolution. Applying approximated values of 5 nm for the linewidth and a spectrometer resolution of 0.5 nm, led to a minimum spectral distance of 3 nm before numerical separation of the emission lines becomes impossible. The corresponding magnetic field strength was then calculated to be approximately 170 T. The sensor should therefore be applicable in most applications that utilize static magnetic fields such as MRIs [102] where the applied field strength is mostly below 10 T.

## CONCLUSION TEMPERATURE RESOLUTION

The previous chapters 9 and 10 presented the characterization of different nanocrystals systems used for nanothermometry measurements.

It was shown that the fluorescence emission of both, Pr:YLF and Er,Yb:YNaF offer a high sensitivity to temperature changes in the range of 0.8–1.45 %/K, depending on their energy level scheme. The recalibration of sensitivity curves obtained with pulsed excitation was shown for continuous measurements performed with dispersed Pr:YLF nanocrystals, with a lifetime tolerance in agreement with values reported for other Pr<sup>3+</sup> doped systems. Still, the signal-to-noise ratio was identified as main limitation for the temperature resolution in dispersion measurements.

Consequently, a polymer fiber thermometer doped with Er,Yb:YNaF was developed, which manages to greatly increase the signal-to-noise ratio and temperature resolutions below 50 mK were achieved. Furthermore this thermometer offers a high robustness against external influence, shown for electric fields and magnetic fields and inhibits all mechanical and chemical properties of polymer fibers. Future research on this thermometer type should therefore be aimed at increasing the degree of integration e.g. in endoscopic applications, as depicted in Figure 11.1. Comparable setups could be used to address needs of temperature measurement as discussed in the introduction, e.g. monitoring temperature in batteries or due to its biological inert properties to measure temperature in food or medicine.

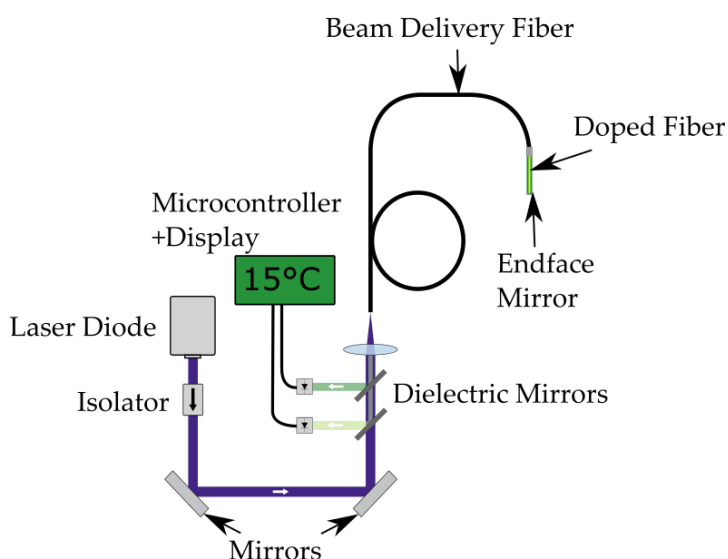


Figure 11.1: Possible setup for an integration of the polymer fiber thermometer in endoscopic applications.

However, the main drawback of this fiber based setup is the near complete surrender of spatial resolution, because the fiber needs to be roughly 2 cm long to unfold its benefits, as shown in previous sections. Therefore, for high spatial resolution measurements nanocrystal dispersion should still be preferable and one approach to achieve even sub-diffraction limited resolution is presented in the following part of this thesis.



Part IV

SPATIAL RESOLUTION IN  
NANOTHERMOMETRY



## NUMERICAL MODEL FOR STED NANOTHERMOMETRY

---

In this chapter a numerical model is presented, which combines a STED microscopy approach with nanothermometers to achieve high spatial resolutions in temperature measurements. First a brief overview over the theoretical background of STED microscopy is given. Following that the numerical model for beam propagation through active media is described. The main findings are then presented in the subsequent section. Additionally, the results shown in these chapter were published in [2].

### 12.1 STIMULATED EMISSION DEPLETION

Since the discovery of the diffraction limit in confocal microscopy and its formulation by Abbe [103], many efforts have been made to break this barrier and enable sub diffraction limit imaging. One particular successful approach was the STED microscopy invented by Stefan Hell and Jan Wichmann in 1994 [104] and consequently awarded with the Nobel prize for chemistry in 2014. The great part of STED microscopy is that its fundamentals seems easy to understand yet it manages to achieve astounding results.

The general principle is similar to fluorescence microscopy, where an optical active material is excited and the emitted fluorescence is collected. Since the backwards emitted light is then used as signal, the spatial resolution is determined by the spotsize of the excitation (EXC), as depicted in Figure 12.1. Building on this, STED microscopy utilizes stimulated emission to suppress the fluorescence emission from certain areas, by depleting the excited energy levels. The stimulated emission is directed according to the incident depletion (DEP) photons therefore only non-depleted areas emit light backwards and the new resolution is given by a superposition of EXC and DEP, as seen in Figure 12.1. By using STED microscopy spatial resolutions even below 100 nm can be achieved in non-contact measurement [105] thus vastly exceeding the diffraction limit.

So far high laser powers are used for STED microscopy to assure sufficient signal strength and fluorescence suppression. This imposes a potential drawback of these methods but it is already addressed in various studies [106, 107]. One way to overcome this barrier of high laser power in STED applications is to work on emission and DEP efficiency of the active materials. This can be done by tuning of the doping concentrations of the active ions inside the nanocrystals thus

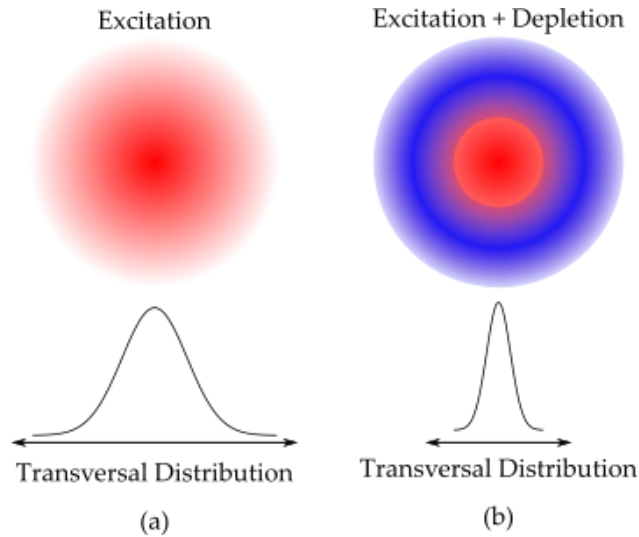


Figure 12.1: Spatial restriction of the fluorescence emission visualized through only excitation (a) and combination of excitation and depletion (b).

utilizing energy migration processes for effective DEP [106]. Another approach is to optimize the timing of EXC and detection which leads to an improved signal-to-noise ratio even at low pump powers [107]. The principle of STED microscopy can be translated to other fluorescence based measurement methods and a detailed numerical study of its potential in nanothermometry is shown in the following sections.

## 12.2 BEAM PROPAGATION METHOD FOR ACTIVE MEDIA

A numerical model was developed to estimate the viability of temperature measurements below the diffraction limit. This was done by combining wide angle beam propagation formalism [108] with laser rate equations. The model was developed for 2-D simulations of a cylindrical symmetric system. The fundamental idea is to model a confocal microscope with an added DEP beam, similar to the aforementioned STED microscopy. A depiction of this setup alongside an exemplary sample with dispersed nanocrystals, is shown in Figure 12.2. As given in the picture, the beam delivery and the geometrical setup correspond to a confocal microscope. The numerical aperture of the imaging system is assumed to be large enough to capture all of the backwards emerging fluorescence. Therefore, the propagation beyond the sample dimension is not necessary.

However, it could be incorporated into the model on the cost of computational resources, if desired. The corresponding spatial resolution  $\Delta x$  of a confocal microscope can be calculated by the beam divergence  $\theta$ , the refractive index  $n$  and the EXC wavelength  $\lambda_{\text{EXC}}$  to be approximately  $0.35\lambda_{\text{EXC}}/(n\sin(\theta))$  [109]. The sample consists of nanocrystals homogeneously dispersed inside a medium, as shown in

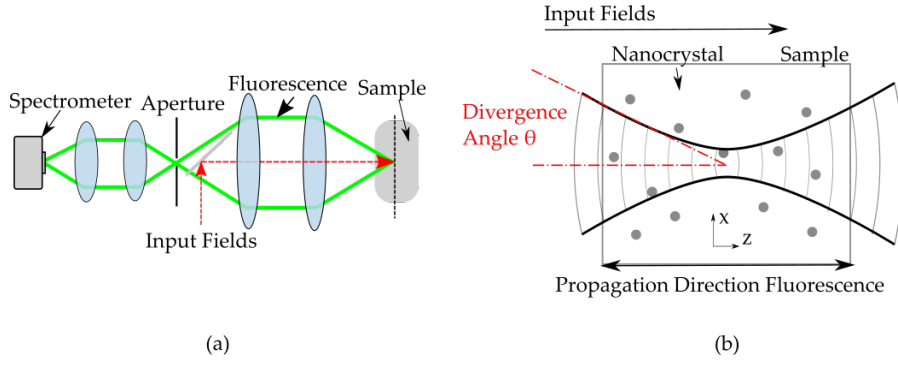


Figure 12.2: Exemplary depiction of a confocal setup with input fields corresponding to EXC and DEP in (a) and a depiction of the geometrical dimensions of the sample with dispersed nanocrystals in (b). Figure partially reprinted from own publication [2].

Figure 12.2b. The modelling was carried out by an iterative algorithm, represented by the corresponding flow chart in Figure 12.3.

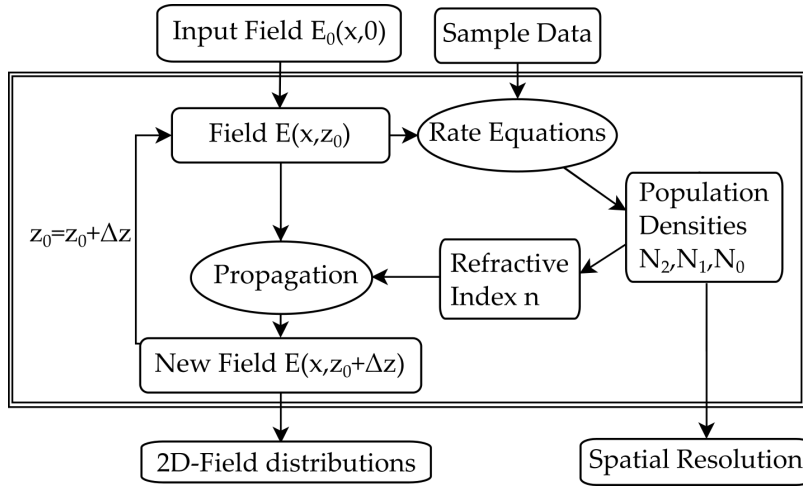


Figure 12.3: Flowchart of the algorithm used to simulate the STED nanothermometry.

In the following sections the two parts, propagation and rate equations, as marked by the elliptical edges in Fig. 12.3 are described, starting the formalism for the beam propagation. Further details on the general formalism can be found in [108, 110].

### 12.2.1 Wide Angle Beam Propagation

The fundamental equation used to model the propagation of light fields  $E=E(x,z)$ , which the coordinate  $x$  perpendicular to the propagation direction  $z$ , is the scalar Helmholtz equation

$$\frac{\partial^2 E}{\partial z^2} - 2in_0k_0 \frac{\partial E}{\partial z} + \frac{\partial^2 E}{\partial x^2} + k_0^2(n^2 - n_0^2)E = 0 \quad (12.1)$$

with a reference refractive index  $n_0$ , the free space propagation constant  $k_0$  and the refractive index of the considered medium  $n$ . Unlike most other beam propagation methods the wide angle formalism does not use the slowly varying envelope approximation, which neglects the fast varying term  $\partial^2 E / \partial z^2$ . Instead, the equation is rewritten to

$$\frac{1}{K^2} \mathcal{D}^2 E - \frac{2i}{K} \mathcal{D} E + \mathcal{P} E = 0 \quad (12.2)$$

with

$$\mathcal{D} \equiv \frac{\partial}{\partial z}, \quad (12.3)$$

$$K = k_0 n_0, \quad (12.4)$$

and

$$\mathcal{P} \equiv \frac{1}{K^2} \left( \frac{\partial^2}{\partial x^2} + (k_0^2 n^2 - K^2) \right). \quad (12.5)$$

By solving this equation similar to a quadratic differential equation, a solution for  $\partial E / \partial z$  is determined to be

$$\mathcal{D} E \equiv \frac{\partial E}{\partial z} = -iK \left( \sqrt{(1 + \mathcal{P})} - 1 \right) E. \quad (12.6)$$

Different expansion approaches can be used to evaluate this expression, and for example applying the first-order Taylor expansion yields the paraxial approximation for light propagation. Since this approximation is not valid for the simulation of strongly focussed lasers beams, a Padé expansion is used [108] with the polynomials  $M$  and  $N$ , with the degree  $m$  and  $n$  respectively, such as

$$\sqrt{(1 + \mathcal{P})} - 1 \approx \frac{M_m(\mathcal{P})}{N_n(\mathcal{P})}. \quad (12.7)$$

Therefore, equation 12.6 can be rewritten to

$$\frac{\partial E}{\partial z} = -iK \frac{M_m(\mathcal{P})}{N_n(\mathcal{P})} E. \quad (12.8)$$

A detailed derivation of the Padé polynomials of arbitrary degree can be found in [110] and here only the exemplary zero order is discussed. The starting point of the calculations is again the wave equation which is recursively expressed as

$$\frac{\partial}{\partial z} \Big|_n = -iK \frac{\mathcal{P}/2}{1 + \frac{i}{2K} \frac{\partial}{\partial z} \Big|_{n-1}}. \quad (12.9)$$

Assuming that the zero order  $z$ -derivative is equal to zero, the first-order approximation, referred to as (1,0) Padé approximation, is therefore

$$\frac{\partial E}{\partial z} = -iK \frac{\mathcal{P}}{2} E. \quad (12.10)$$

The numerical implementation is done by using the finite difference method [110]. These numerical method relies on the discretization of the derivative  $d/dz$  into discrete steps with the width  $\Delta z$  like

$$\frac{dE}{dz} = \frac{E^{z+\Delta z} - E^z}{\Delta z} \quad (12.11)$$

and

$$\frac{d^2E}{dz^2} = \frac{E^{z-\Delta z} - 2E^z + E^{z+\Delta z}}{\Delta z^2}. \quad (12.12)$$

One exemplary implementation is the forward scheme, where the field at the node  $j+1=z_0+\Delta z$  is derived from the discretised values of the field in the plane  $j=z_0$  as shown in Figure 12.4. Another implementation is the Crank-Nicolson scheme [110], which is shown in Figure 12.4c, which is commonly used due to its increased numerical stability. Applying the Crank-Nicolson discretization to equation 12.8 leads

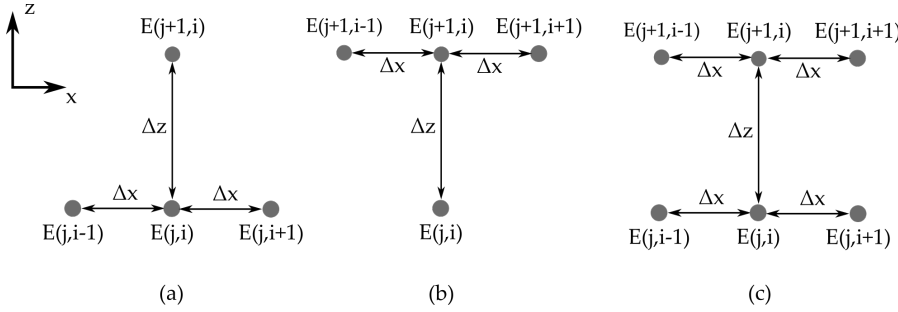


Figure 12.4: Different variants of finite difference schemes. Shown in (a) the forward in (b) the backward and in (c) the combined Crank-Nicolson scheme [111].

to an expression of the field at position  $z=j+1$  in dependency of the position  $z=j$

$$E^{j+1} = \frac{N - iK\Delta z(1 - \alpha)M}{N + iK\Delta z\alpha M} E^j \quad (12.13)$$

where  $\alpha$  is introduced as a parameter to ensure numerical stability [111]. This equation can also be written as [112]

$$E^{j+1} = \frac{\sum_{i=0}^n \xi_i \mathcal{P}^i}{\sum_{i=0}^n \chi_i \mathcal{P}^i} E^j \quad (12.14)$$

using the polynomial coefficients  $\xi$  and  $\chi$ , because both  $M$  and  $N$  are polynomials of degree  $n$ .

The numerical implementation of equation 12.13 is done by a multi-step method according to [112]. For this, both numerator and denominator of the polynomials in equation 12.13 are expressed by their roots, leading to

$$E^{j+1} = \frac{(1 + \alpha_1 \mathcal{P})(1 + \alpha_2 \mathcal{P}) \dots (1 + \alpha_n \mathcal{P})}{(1 + \beta_1 \mathcal{P})(1 + \beta_2 \mathcal{P}) \dots (1 + \beta_n \mathcal{P})} E^j, \quad (12.15)$$

which can be rewritten into a multi-step expression of n steps as

$$E^{j+\frac{i}{n}} = \frac{(1 + \alpha_i \mathcal{P})}{(1 + \beta_i \mathcal{P})} E^{j+\frac{i-1}{n}}. \quad (12.16)$$

The parameters  $\alpha_i$  and  $\beta_i$  are derived for a second order Padé approximation by inserting the corresponding values for M and N in equation 12.13, which after rearranging [110] results in

$$E^{j+1} = \frac{1 + \mathcal{P} \left[ \frac{3}{4} - \frac{iK\Delta z(1-\alpha)}{2} \right] + \mathcal{P}^2 \left[ \frac{1}{16} - \frac{iK\Delta z(1-\alpha)}{4} \right]}{1 + \mathcal{P} \left[ \frac{3}{4} + \frac{iK\Delta z\alpha}{2} \right] + \mathcal{P}^2 \left[ \frac{1}{16} + \frac{iK\Delta z\alpha}{4} \right]} E^j. \quad (12.17)$$

Combining equations 12.14 and 12.17, the coefficients  $\zeta_{1,2}$  and  $\chi_{1,2}$  are then determined to be

$$\zeta_1 = \frac{3}{4} - \frac{iK\Delta z(1-\alpha)}{2}, \quad (12.18)$$

$$\zeta_2 = \frac{1}{16} - \frac{iK\Delta z(1-\alpha)}{4}, \quad (12.19)$$

$$\chi_1 = \frac{3}{4} + \frac{iK\Delta z\alpha}{2}, \quad (12.20)$$

$$\chi_2 = \frac{1}{16} + \frac{iK\Delta z\alpha}{4} \quad (12.21)$$

while  $\zeta_0$  and  $\chi_0$  are equal to one. The relations between these parameters and  $\alpha_{1,2}$  and  $\beta_{1,2}$  are derived from multiplications up to the second order, namely n equal to two in equation 12.15, and are given by

$$\alpha_1 = \frac{1}{2} \left[ \zeta_1 - \sqrt{\zeta_1^2 - 4\zeta_2} \right], \quad (12.22)$$

$$\beta_1 = \frac{1}{2} \left[ \zeta_1 + \sqrt{\zeta_1^2 - 4\zeta_2} \right], \quad (12.23)$$

$$\alpha_2 = \frac{1}{2} \left[ \chi_1 - \sqrt{\chi_1^2 - 4\chi_2} \right], \quad (12.24)$$

$$\beta_2 = \frac{1}{2} \left[ \chi_1 + \sqrt{\chi_1^2 - 4\chi_2} \right]. \quad (12.25)$$

Once all parameters are defined the second order split-step propagation of the light field E performed starting with the first propagation step as

$$E^{j+\frac{1}{2}} = \frac{1 + \alpha_1 \mathcal{P}}{1 + \beta_1 \mathcal{P}} E^j. \quad (12.26)$$

Inserting  $\mathcal{P}$ , as defined in 12.7, and consequently applying the finite difference discretization, given in 12.12, results in

$$\begin{aligned} E_i^{j+\frac{1}{2}} + \frac{\beta_1}{K^2} \frac{E_{i-1}^{j+\frac{1}{2}} - 2E_i^{j+\frac{1}{2}} + E_{i+1}^{j+\frac{1}{2}}}{\Delta x^2} + \frac{\beta_1}{K^2} (k^2 - K^2) E_i^{j+\frac{1}{2}} \\ = E_i^j + \frac{\alpha_1}{K^2} \frac{E_{i-1}^j - 2E_i^j + E_{i+1}^j}{\Delta x^2} + \frac{\alpha_1}{K^2} (k^2 - K^2) E_i^j. \end{aligned} \quad (12.27)$$



There are different ways to efficiently solve equations like these and one popular is the Thomas algorithm [110], which is mostly used to solve tridiagonal matrix equations. Therefore, equation 12.27 is rewritten by separating the variables in a way that it can be expressed by

$$\begin{bmatrix} b & c & 0 & 0 & . & . & 0 & 0 & 0 & 0 \\ a & b & c & 0 & . & . & 0 & 0 & 0 & 0 \\ 0 & a & b & c & . & . & 0 & 0 & 0 & 0 \\ . & . & . & . & . & . & . & . & . & . \\ 0 & 0 & 0 & 0 & . & . & 0 & a & b & c \\ 0 & 0 & 0 & 0 & . & . & 0 & 0 & a & b \end{bmatrix} \begin{bmatrix} E_0^{j+\frac{1}{2}} \\ E_1^{j+\frac{1}{2}} \\ E_2^{j+\frac{1}{2}} \\ \dots \\ E_{n-1}^{j+\frac{1}{2}} \\ E_n^{j+\frac{1}{2}} \end{bmatrix} = \begin{bmatrix} r_0 \\ r_1 \\ r_2 \\ \dots \\ r_{n-1} \\ r_n \end{bmatrix} \quad (12.28)$$

where

$$a_j = \frac{\beta_j}{K^2 \Delta x^2}, \quad (12.29)$$

$$b_j = 1 - \frac{2\beta_j}{K^2 \Delta x^2} + \frac{\beta_1}{K^2} (k^2 - K^2), \quad (12.30)$$

$$c_j = \frac{\beta_j}{K^2 \Delta x^2}, \quad (12.31)$$

$$r_j = E_i^j + \frac{\alpha_1}{K^2} \frac{E_{i-1}^j - 2E_i^j + E_{i+1}^j}{\Delta x^2} + \frac{\alpha_1}{K^2} (k^2 - K^2) E_i^j. \quad (12.32)$$

This wide angle formalism allows for the simulation of highly divergent beams, as shown in Fig. 12.4, and as mentioned earlier, it can even be extended to higher order Padé approximation if needed.

### 12.2.2 Depletion Intensity

The second part necessary to describe the propagation of light in this model are the laser rate equations [110]. This set of equations is used to calculate populations dynamics of the energy levels, as mentioned in chapter 4.1. The populations densities  $N_i$ , with  $i(=0,1,2,\dots)$  being the index of the corresponding energy levels, combined with the optical cross sections  $\sigma_{\text{ems}}$  and  $\sigma_{\text{abs}}$  can then be used to calculate the refractive index by further expanding it into real and imaginary part to account for amplification and absorption like

$$\begin{aligned} n(\lambda) &= n_0(\lambda) + i\kappa \\ &= n_0 + i \frac{\lambda}{4\pi} (N_2 \sigma_{\text{ems}}(\lambda) + N_1 \sigma_{\text{ems}}(\lambda) - N_0 \sigma_{\text{abs}}(\lambda)). \end{aligned} \quad (12.33)$$

Material absorption or scattering could further influence the propagation but these mechanisms were neglected due to the low sample thickness. However, if needed they could be incorporated into the algorithm.

The basic equations are similar to the ones presented in earlier sections. The most important one for this application is the steady state equation describing the population density  $N_2$  inside the upper laser level, which for the steady state can be derived to be

$$N_2 = \frac{\frac{\sigma_{\text{abs}} I_{\text{EXC}}}{h\nu_{\text{EXC}}}}{\frac{1}{\tau_{2,1}} + \frac{\sigma_{\text{abs}} I_{\text{EXC}}}{h\nu_{\text{EXC}}} + \frac{\sigma_{\text{ems}} I_{\text{DEP}}}{h\nu_{\text{DEP}}}}. \quad (12.34)$$

Inside the STED nanothermometry model, this equation is used to estimate the spatial distribution of the fluorescence emitting levels. Also from this expression, the saturation intensity can be derived to satisfy the condition

$$N_2(I_{\text{EXC}} = I_{\text{Sat}}) = \frac{1}{e} N_2(I_{\text{EXC}} = 0). \quad (12.35)$$

Since the probability of the emission of a photon is proportional to the population density  $N_2$ , this corresponds to the seed intensity at which this probability of fluorescence emission drops below  $1/e$ . The saturation intensity is then calculated by

$$I_{\text{Sat}} = h\nu_{\text{DEP}} \left( \frac{1}{\sigma_{\text{ems}} \tau_{2,1}} + \frac{\sigma_{\text{abs}} I_{\text{EXC}}}{\sigma_{\text{ems}} h\nu_{\text{EXC}}} \right). \quad (12.36)$$

The input fields for EXC and DEP consist of a Gaussian laser mode  $TEM_{00}$  and a  $TEM_{01}$  (1D approximation of a donut mode), respectively. The transversal distributions and an overview of the longitudinal propagating fields are depicted in Figure 13.1. The total power and

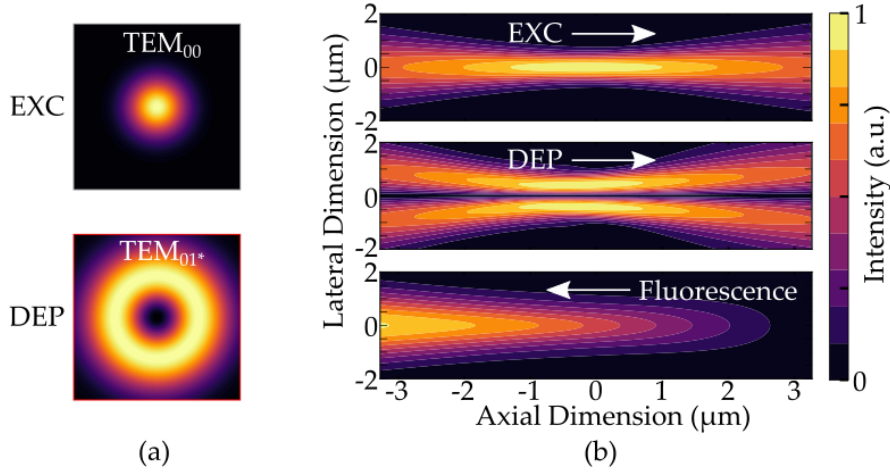


Figure 13.1: Depiction of the propagating fields EXC, DEP and the emerging fluorescence. Shown are the transversal distribution of the input fields (a) and the longitudinal propagation of all fields (b). Figure partially reprinted from own publication [2].

FWHM of the EXC is kept constant throughout the simulations, and only the power and the beam waist of the DEP are varied, with the latter defined as the outer diameter of the  $TEM_{01}$  mode. These variations are expressed by the ratio of powers  $PR=P_{DEP}/P_{Sat}$ , where  $P_{Sat}$  is calculated from the saturation intensity  $I_{Sat}$  at which the population of the upper laser level drops to 50% of its initial value [105]. The material specific relations of  $I_{Sat}$  can be derived from the laser rate equations [110], depending on the EXC intensity  $I_{EXC}$  and the fluorescence lifetime  $\tau$ , to be

$$I_{Sat} = h\nu_{DEP} \left( \frac{1}{\sigma_{ems}\tau} + \frac{\sigma_{abs}}{\sigma_{ems}} \frac{I_{EXC}}{h\nu_{EXC}} \right). \quad (13.1)$$

The other parameter, that was varied throughout the calculations, is the beam waist ratio  $BR=w_{DEP}/w_{EXC}$ .

The simulation window, as shown in Figure 13.1 spans up to  $14\ \mu\text{m}$  in the  $z$ -direction, and the simulations were conducted for forward and backward propagating fields as shown in Figure 13.1b. The incorporated fields are EXC, DEP and two different emission lines, each for

two directions, resulting in eight different simulation slots. The spatial resolution  $\Delta x$  is then given by the transverse distribution of the excited energy levels,  $N_2$  and  $N_1$ . More specifically different definitions for the resolution can be applied which are distinguished by the acceptable noise level, as shown in Fig. 13.2. One,  $\Delta x_{50\%}$ , corresponds to the definition of resolution commonly used in optical microscopy, which is depicted in Figure 13.2a. However, since the signal-to-noise ratio is a crucial parameter for the temperature resolution, another definition was applied. For this definition a conservative assumption of a 5% noise level was made. Therefore,  $\Delta x_{5\%}$ , is more in accordance with nanothermometry measurements where the complete signal strength measurable above the noise level of 5% is considered.

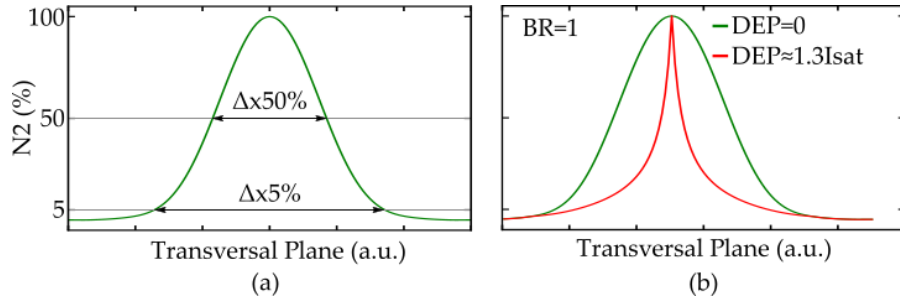


Figure 13.2: Two definitions of the spatial resolution,  $\Delta x_{50\%}$  corresponding to optical microscopy and  $\Delta x_{5\%}$  used in accordance to nanothermometry measurements in (a) and the construction of population densities due to depletion in (b). Figure partially reprinted from own publication [2].

The initial value for the sample thickness was 80 nm, which is equivalent to the minimal axial resolution achieved in a 4-Pi confocal microscope [113].

Up to this point all defined correlations and parameters can be universally translated to different active materials. However, to solve the rate equations, certain material specific parameters are necessary such as the optical cross sections  $\sigma_{\text{abs}}$  and  $\sigma_{\text{ems}}$ , and the fluorescence lifetime  $\tau$ .

Pr:YLF NCs were chosen as model system because they combine high sensitivity to temperature changes of 1.1% /K [22] with a short EXC wavelength of e.g. 444 nm or 480 nm [45], therefore enabling a tighter focussing of EXC compared to e.g. Er,Yb:YNaF. The wavelengths of the input fields were consequently chosen according to the Pr:YLF transition spectra [22] to be 444 nm and 607 nm, respectively. By choosing a DEP beam at 607 nm a large spectral separation of the two signal beams of 520 nm and 639 nm whose FIR is used to determine the systems temperature is assured.

Pr:YLF nanothermometer enable an easy spectral separation of signal, excitation and depletion, which again highlights their potential for such applications. The EXC waist  $w_0$  of the Gaussian beam was

chosen to be 500 nm, and the EXC fluence was set to 1200 MW/cm<sup>2</sup>. This fluence was chosen for multiple reasons. First to assure sufficient fluorescence emission and secondly because similar values are currently used in other STED approaches [104, 105]. However, the high level of laser radiation may cause additional heating, as discussed in detail in the previous sections containing the doped polymer fiber. Therefore, the tolerance of sample heating needs to be determined before the measurement. If the application allows a small temperature increase, these effects can be calibrated, as shown in previous sections, and exact temperature measurement is still possible. Else, additional measures can be taken to minimize this, e.g. utilizing short pulses or adapting the active ion, and with that tuning the excitation wavelength to prevent host absorption, have proven useful to minimize heating.

The lateral resolutions depending on both the PR and the BR were calculated and the results are given in Figure 13.3. Improvement in

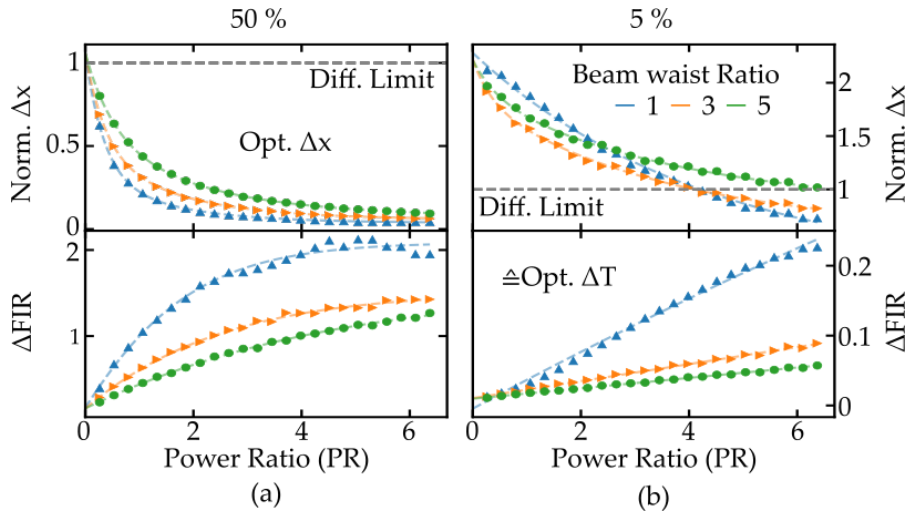


Figure 13.3: Influence of power ratio  $P_{\text{DEP}}/P_{\text{EXC}}$  and beam waist ratio  $w_{\text{DEP}}/w_{\text{EXC}}$ , on both resolutions for the two definitions  $\Delta x_{50\%}$  in (a) and  $\Delta x_{5\%}$  in (b). Figure partially reprinted from own publication [2].

spatial resolution is accompanied by a decrease in temperature resolution. This effect can be explained by a change in the signal-to-noise ratio, which arises as the outer shape of the population distribution changes from a Gaussian to a steeper distribution, as depicted in Figure 13.2a. Through this, the FWHM of the population strongly decreases, which consequently leads to the mentioned enhancement in spatial resolution. On the other hand, the signal-to-noise ratio as defined by the noise level in Figure 13.2a decreases and following this the  $\Delta$ FIR increases. This opposite behaviour of spatial resolution and temperature resolution was already observed in other nanothermometry applications [28], though STED nanothermometry manages to push the severance of this trade off to higher spatial resolution than what was previously reported. However, a trade-off between the two resolu-

tions is inevitable for both definitions of  $\Delta x$ , as shown in 13.3. Since this work is aimed to find an optimal compromise between the spatial resolution  $\Delta x$  and the temperature resolution  $\Delta T$  the definition of  $\Delta x_{5\%}$  is used for further calculations.

The product of both resolutions is used as a figure-of-merit to quantify the performance of STED nanothermometry. The results are shown in Fig. 13.4. It might be necessary to adapt the figure-of-merit

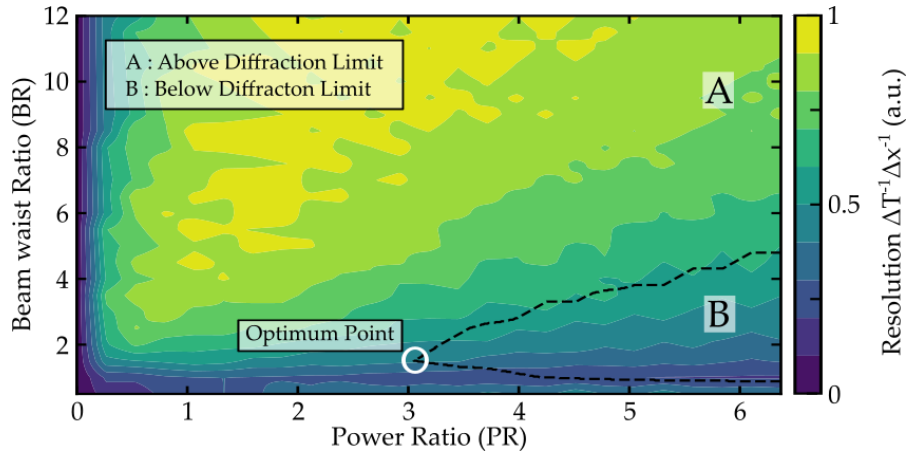


Figure 13.4: Combined resolution value as a figure of merit to optimize the parameters. Marked by the white circle is the optimum point which corresponds to the minimal depletion power that still leads to sub-diffraction spatial resolution. Figure partially reprinted from own publication [2].

for specific measurement, however the simple product is well suited to study the general performance enhancement. The overall performance is optimized by gradually increasing PR and BR, respectively. The combination of large EXC diameter and strong EXC power compensates the aforementioned shape of the population distribution through assuring sufficient noise suppression, though on the cost of a reduced improvement in spatial resolution.

To highlight the spatial resolution and to further evaluate optimal parameters for applications, the parameter space, as shown in Figure 13.4, is divided in two regions, A and B, marked by the dashed line in Figure 13.4. The main distinction between the two regions is the corresponding spatial resolution with the boundary value being the limit of the corresponding confocal microscope. Furthermore, to avoid laser induced heating the DEP power should be kept at a minimum value. High DEP powers also lower the absolute fluorescence intensity  $P_{\text{out}}$  extractable from the system by reducing the population of the emission levels. The optimum point for sub-diffraction limited thermometry is therefore chosen as marked in Figure 13.4. At this point temperature measurements below the diffraction limit are possible, while maintaining the value of  $\Delta \text{FIR}$  below 8 %.

## 13.1 SAMPLE THICKNESS AND POSITION

Building up on this general assessment, further calculations can be performed to estimate the influence of the sample position, relative to the EXC beam. These results correspond to an axial scan through the sample and help to deepen the understanding of the fundamental relation between temperature and spatial resolution. The simulations were carried out at the values of PR and BR previously defined as the optimum, shown in Figure 13.4. The dependence of the inverse resolutions  $\Delta x^{-1}$ ,  $\Delta T^{-1}$ , and the total emission  $P_{\text{out}}$  are presented in Figure 13.5.

First, different sample positions are considered, as depicted in Figure 13.5a, and again a complementary tendency of the temperature and the spatial resolution becomes visible, especially outside of the focal region ( $\pm 2 \mu\text{m}$ ). This behaviour can be again explained by a change in the shape of the population distribution due to the DEP, which is stronger around the focal plane and weaker in the other regions.  $P_{\text{out}}$  also reaches a minimum value in this region due to the strong DEP in the focal plane. The local maximum of the inverse  $\Delta T$  should prove useful in further optimizing the measurement for specific applications, as it shows that even inside the focal region precise temperature measurements are possible.

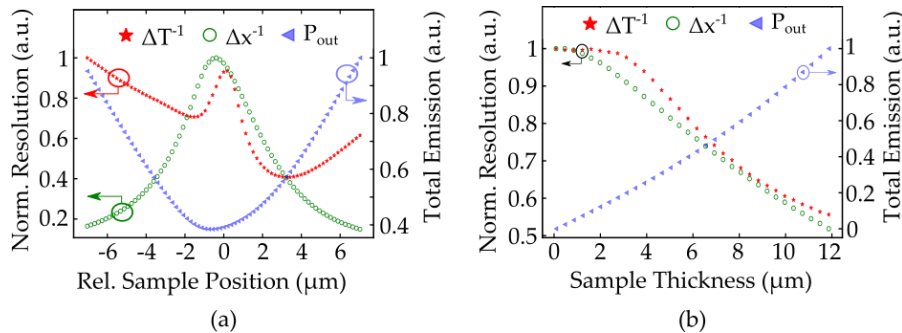


Figure 13.5: Dependence of the  $\Delta T$ ,  $\Delta x$  and  $P_{\text{out}}$  on the position of the sample relative to the EXC beam (a) and on the sample thickness (b). Figure partially reprinted from own publication [2].

Increasing the sample thickness, while keeping the central position leads to correlations, as shown in Figure 13.5b. Here both resolutions drop as less depleted regions are included, while  $P_{\text{out}}$  strongly increases for thicker samples because of the higher total number of active ions providing the emission. The absolute decrease is lower than the values for different sample positions, which is as expected since the highly depleted regions are always included.

Both numerical studies highlight the potential of adapting spatial and temperature resolution to applications, following the correlation between  $\Delta\text{FIR}$  and FWHM. They also show the feasibility of temperature measurements in voluminous media with high spatial resolution

and ways to address the required compromises, by e.g. shifting the sample position.

### 13.2 ABSOLUTE TEMPERATURE RESOLUTION

As mentioned before, the developed model is applicable to different nanothermometers systems. The fundamental parameters necessary to evaluate the performance of a nanothermometers are discussed in the first part of this work. As a brief repetition, most important are the sensitivity

$$S = \frac{d\text{FIR}}{dT} \text{FIR}_0 \quad (13.2)$$

which is independent of the spatial resolution and only depends on the energy level structure and the emission lines of the material [20] and the temperature resolution

$$\Delta T = \frac{1}{\text{FIR}_0} \frac{1}{S} \Delta \text{FIR} \quad (13.3)$$

which is derived from  $S$ , the value of the FIR at the center of the measurement range ( $\text{FIR}_0$ ) and  $\Delta \text{FIR}$  [22].

Most of the current research is aimed at optimizing the sensitivity and explain its role in resolution e.g. [52]. The model presented here provides the other part in the optimization by addressing the signal-to-noise ratio, as evident by Equation 13.3. The minimum  $\Delta \text{FIR}$  with a simultaneous value of  $\Delta x$  below the diffraction limit achieved in the simulation was 5.8%. Applying this to sensitivities of currently used nanothermometer reveals their possible temperature resolution in nanoscale measurements and the results are shown in Table 13.1. This numerical study reveals necessary steps to increase the spatial

Active Material	$\text{FIR}_0$	$S$ (%/K)	$\Delta T_{calc}$ (K)
Pr:YLF[22]	1	1.1	$\pm 2.5$
Er,Yb@Yb,Tm:LaF [114]	0.38	5	$\pm 1.5$
Tm,Ho,Yb:YAG [52]	3.35	0.7	$\pm 1.25$

Table 13.1: Sub-diffraction limited temperature resolutions theoretical achievable with STED nanothermometry at  $T_0$  of 20°C.

resolution beyond the diffraction limit, while still keeping temperature resolution below an absolute value of  $\pm 1.25$  K. Combined with the presented ability of three-dimensional measurements independent on sample surface quality and outer dimensions, STED nanothermometry could therefore be valuable especially for threshold measurements in biomedical applications e.g. strongly localized hyperthermia treatment of cancer cells [115].

The high laser power used for STED as a potential drawback of STED based methods via induced heating is already being addressed



in various studies [106, 107] e.g. by working on the emission and DEP efficiency of the active materials. This can be achieved by tuning of the doping concentrations as mentioned earlier [106]. Since these tuning steps also play in role in laser optimization of comparable nanocrystals [36], this shows the feasibility of the proposed STED nanothermometry but also hints at the potential in future research on this topic. Besides this, the fact that simply switching off the DEP beam, the benefits of classical fluorescence thermometry are restored, further adds to the flexibility of STED nanothermometry.



Part V

CONCLUSION



SUMMARY AND OUTLOOK

---

In this last part the achieved results in terms of both, temperature and spatial resolution, are summarized, and further optimizations approaches are discussed. Generally, lanthanide doped nanocrystals are already used as a versatile platform for temperature monitoring, however the different optimization steps presented manage to push their performance even further.

The first strategy explained in the first part of this thesis, is the selection of an appropriate pumping regime. This choice is mostly influenced by the energy level scheme of the respective active ions. It was shown that the temperature error due to fluctuations often associated with conventional nanosecond pulsed lasers can be as high as 0.5 K. Additionally the difference in energy level population can prevent the flexible switching of the pump regime. A formalism was developed to recalibrate baseline measurements and exchange calibration data between the two optimal pump regimes, short pulsed or continuous excitation. This formalism was subsequently applied to correct the temperature measurements conducted with Pr:YLF dispersions under continuous excitation.

Following this the embedding of nanocrystals in a polymer fiber was examined. This doping of nanocrystals inside a solid host, functions as an approach to increase the signal-to-noise ratio. This fiber thermometer was then thoroughly characterized, and effects like laser induced heating were identified. The impact of laser induced heating led to the derivation of a calibration range. Overall it was shown that by doping upconversion nanocrystals inside polymer fibers, temperature sensors with an excellent sensitivity of 1.45%/K and resolution of 19 mK can be manufactured. The associated values are given in Table 10.1. The system was characterized in a temperature range of 13 to 33 °C, but there is no indication that the sensor is limited to these values. The measurement range solely depends on the integrity of the host material and a polymer sensor has been successfully demonstrated between -55 to 70 °C [100]. The operating range of our temperature sensor therefore matches the required temperature range of 15 to 50 °C [16] for monitoring lithium batteries, which is one task where commonly used thermometers might struggle due to the presence of external fields, as mentioned in the introduction. The influence of electrical fields on the sensor readout was measured to study the feasibility of nanothermometers in these applications, and no deviation of the performance is visible for electric fields up to 12.5 kV/cm.

The effect of magnetic fields on the sensor readout was calculated in a numerical study. These results show that precise temperature monitoring should be possible under the influence of magnetic fields up to approximately 170 T.

Both of these investigations hint at the potential for the doped polymer in applications such as monitoring in batteries.

Besides the higher temperature resolution, this sensor shows additional advantages compared to other passive fiber sensor concepts, like the one presented in [100]. For example, the fluorescence intensity ratio extracted from this doped fiber is virtually independent of bending or mechanical deformations of the fiber. Other passive sensors often rely on the difference in transmittance between two wavelengths and they also need at least two light sources. This is requirement is also reduced by incorporating active nanocrystals where only one laser diode is needed to excite emission. Therefore, reducing the cost of a measurement setup and simplifying the usage of the sensor. Adding that the polymer host material also shows good bio-compatibility, the developed sensor constitutes an ideal candidate to monitor temperatures in various medical applications. Further simplification of the setup could be realized by adding reflecting films to the fiber end facets similar to the approach in [116]. This preparation would allow for more compact setups and with that especially beneficial for endoscopic temperature monitoring, as discussed in the previous part. However, the pump-light-induced heating might be a drawback for example, in medical examinations. A possible solution to this could be the usage of smaller fiber cores combined with improvements in emission measurement. By reducing the fiber core size, the same pump energy density and the same population density could be reached at reduced absolute values of pump power. This would minimize the absolute value of deposited heat but also reduce the absolute emission output, and therefore, potentially, the accuracy.

Further research should also focus on the utilisation of different polymers to reduce host absorption of the pump light and, therefore, heating of the host material. The application areas of the nanocrystal polymer combination can also be significantly broadened by setting aside the fiber design, as much more flexible light-guiding structures can be manufactured from polymer by 3-D printing [117]. These techniques enable the integration of the nanothermometers into more complex photonic structures such as multi-functional lab-on-a-chip components.

Another disadvantage of this macroscopic thermometer is the reduced spatial resolution, which was addressed in the last part of this work, by utilizing STED microscopy. In this approach a second laser beam is used to deplete the energy levels via stimulated emission. A numerical model was developed to study the influence of different relations between excitation and depletion beam. Parameters studies

were performed for an exemplary Pr:YLF nanothermometer. It was illustrated that this approach can be used to push the spatial resolution of lanthanide based nanothermometers below the diffraction limit. The temperature resolutions corresponding to these sub-diffraction measurements were assessed by analysing the signal-to-noise ratio. The result was a single degree precision ( $\pm 1.5$  K) that can be achieved with commonly used nanothermometers. It can be expected that further optimization of the sensitivity of nanothermometers leads to even lower values. The adaptation of this approach to desired applications was shown by deducing an exemplary figure of merit. The most promising application field for such a technique should be nanocrystals dispersed in liquid solutions for example in medical sciences, as one selling point of STED nanothermometry is its robustness against surface errors. Therefore, additional simulations were carried out to investigate the influence of sample thickness and to prove the viability of volumetric scans. The results of these calculations were sequentially presented for the optimum point identified from the figure of merit.

The major drawback of STED nanothermometry is the high laser powers, commonly used in STED applications. These high powers may cause additional heating of even destruction of the sample. However, various research efforts are directed at this challenge for example [106, 107] with the main idea being optimization of the efficiency of energy transfers inside the nanocrystals. The most promising approaches in this regard evolve around the implementation of new active materials or the tuning of doping concentrations in known nanocrystal configurations. Especially the influence of doping concentrations need to be carefully considered. For example, increasing the concentration of Neodymium ions in  $\text{Nd}^{3+}:\text{LaPO}_4$  may increase the absorption efficiency [118] and therefore, reduce the necessary pump power. This would enable improvements in many measurements and would also affect both doped fiber thermometers as well as STED nanothermometry. However, a higher concentration of neodymium ions also increases non-radiative transitions [118] such as cross relaxations. If the rate of these transitions exceeds the rate of thermalization between the energy levels they can break the Boltzmann dependency and therefore introduce measurement errors. Additionally, heating can be minimized by carefully matching absorption and optical transitions through adequate selection of the active material from the plethora of possible nanocrystals.

In conclusions, nanothermometry can be used for temperature measurements with high resolutions in both temperature and space with relatively simple setups. The underlying measurement principle manages to clearly differentiate from other thermometers like electrical sensors or optically passive components. Therefore, possible applications can be found throughout engineering and medicine, and even

though many exciting approaches were already demonstrated, the research field still offers much to be explored.



## BIBLIOGRAPHY

---

- [1] J. Thiem, S. Spelthann, L. Neumann, F. Jakobs, H.-H. Johannes, W. Kowalsky, D. Kracht, J. Neumann, A. Ruehl, and D. Ristau. "Upconversion Nanocrystal Doped Polymer Fiber Thermometer". In: *Sensors* 20.21 (2020), p. 6048.
- [2] J. Thiem, S. Spelthann, J. Neumann, A. Ruehl, and D. Ristau. "Three-dimensional nanothermometry below the diffraction limit". In: *Optics Letters* 46.14 (2021), pp. 3352–3355.
- [3] J. Thiem, A. Ruehl, and D. Ristau. "Influence of Pumping Regime on Temperature Resolution in Nanothermometry". In: *Nanomaterials* 11.7 (2021), p. 1782.
- [4] Olof Beckman. "Anders Celsius and the fixed points of the Celsius scale". In: *European Journal of Physics* 18.3 (1997), p. 169.
- [5] Lord Kelvin. "William (October 1848)." On an Absolute Thermometric Scale". In: *Philosophical Magazine*. Lee, JM (1997).
- [6] Joachim Fischer. "The Boltzmann Constant for the Definition and Realization of the Kelvin". In: *Annalen der Physik* 531.5 (2019), p. 1800304. DOI: <https://doi.org/10.1002/andp.201800304>. eprint: <https://onlinelibrary.wiley.com/doi/pdf/10.1002/andp.201800304>. URL: <https://onlinelibrary.wiley.com/doi/abs/10.1002/andp.201800304>.
- [7] David G. Cahill, Wayne K. Ford, Kenneth E. Goodson, Gerald D. Mahan, Arun Majumdar, Humphrey J. Maris, Roberto Merlin, and Simon R. Phillpot. "Nanoscale thermal transport". In: *Journal of Applied Physics* 93.2 (2003), pp. 793–818. DOI: [10.1063/1.1524305](https://doi.org/10.1063/1.1524305). eprint: <https://doi.org/10.1063/1.1524305>. URL: <https://doi.org/10.1063/1.1524305>.
- [8] Kittel C. In: *Am. J. Phys.* 41 (1973), p. 1211.
- [9] Grey Sh. Boltachev and Jörn W. P. Schmelzer. "On the definition of temperature and its fluctuations in small systems". In: *The Journal of Chemical Physics* 133.13 (2010), p. 134509. DOI: [10.1063/1.3486557](https://doi.org/10.1063/1.3486557).
- [10] Robert McGraw and Randall A LaViolette. "Fluctuations, temperature, and detailed balance in classical nucleation theory". In: *The Journal of chemical physics* 102.22 (1995), pp. 8983–8994.
- [11] Joanna Berteaud, Johanna Pasquet, Thomas Schücker, and André Tilquin. "On a quadratic equation of state and a universe mildly bouncing above the Planck temperature". In: *Journal of Cosmology and Astroparticle Physics* 2019.10 (2019), p. 069.

- [12] Tim Kovachy, Jason M Hogan, Alex Sugarbaker, Susannah M Dickerson, Christine A Donnelly, Chris Overstreet, and Mark A Kasevich. "Matter wave lensing to picokelvin temperatures". In: *Physical review letters* 114.14 (2015), p. 143004.
- [13] Meijun Jin, Junming Li, Caili Wang, and Ruilan Shang. "A Practical Split-Window Algorithm for Retrieving Land Surface Temperature from Landsat-8 Data and a Case Study of an Urban Area in China". In: *Remote Sensing* 7.4 (2015), pp. 4371–4390. ISSN: 2072-4292. DOI: [10.3390/rs70404371](https://doi.org/10.3390/rs70404371).
- [14] Florent Calvo, Elke Pahl, Michael Wormit, and Peter Schwerdtfeger. "Erklärung des niedrigen Schmelzpunkts von Quecksilber mit relativistischen Effekten". In: *Angewandte Chemie* 125.29 (2013), pp. 7731–7734.
- [15] José Antonio Sobrino, Yves Julien, and Susana García-Monteiro. "Surface temperature of the planet earth from satellite data". In: *Remote Sensing* 12.2 (2020), p. 218.
- [16] Seyed Mohammad Rezvanizani, Zongchang Liu, Yan Chen, and Jay Lee. "Review and recent advances in battery health monitoring and prognostics technologies for electric vehicle (EV) safety and mobility". In: *Journal of Power Sources* 256 (2014), pp. 110–124. ISSN: 0378-7753. DOI: <https://doi.org/10.1016/j.jpowsour.2014.01.085>. URL: <https://www.sciencedirect.com/science/article/pii/S0378775314001098>.
- [17] Nuala M Rynne, Thomas P Beresford, Alan L Kelly, and Timothy P Guinee. "Effect of milk pasteurization temperature and in situ whey protein denaturation on the composition, texture and heat-induced functionality of half-fat Cheddar cheese". In: *International Dairy Journal* 14.11 (2004), pp. 989–1001.
- [18] Fernando G Gardim, Giuliano Giacalone, Matthew Luzum, and Jean-Yves Ollitrault. "Thermodynamics of hot strong-interaction matter from ultrarelativistic nuclear collisions". In: *Nature Physics* 16.6 (2020), pp. 615–619.
- [19] Thomas D. McGee. *Principles and Methods of Temperature Measurements*. John Wiley & Sons, Inc., 1988.
- [20] F. Vetrone, R. Naccache, A. Zamarron, A. Juarranz de la Fuente, F. Sanz-Rodriguez, L.M. Maestro, E.M. Rodriguez, D. Jaque, J.G. Sole, and J.A. Capobianco. "Temperature Sensing Using Fluorescent Nanothermometers". In: *ACS NANO* 4 (2010), 3254–3258.
- [21] Antonio Benayas, Blanca Del Rosal, Alberto Pérez-Delgado, Karla Santacruz-Gómez, Daniel Jaque, Gustavo Alonso Hirata, and Fiorenzo Vetrone. "Nd: YAG near-infrared luminescent nanothermometers". In: *Advanced Optical Materials* 3.5 (2015), pp. 687–694.

- [22] M.S. Pudovkin, S.L. Korableva, D.A. Koryakovtseva, E.V. Luki-nova, A.V. Lovchev, O.A. Morozov, and V.V. Semashko. "The comparison of  $\text{Pr}^{3+}:\text{LaF}_3$  and  $\text{Pr}^{3+}:\text{LiYF}_4$  luminescent nano-and microthermometer performances". In: *J. Nanopart. Res.* 21 (2019), p. 266.
- [23] Vesna Lojpur, M Nikolic, L Mancic, O Milosevic, and MD Dramicanin. " $\text{Y}_2\text{O}_3:\text{Yb}$ , Tm and  $\text{Y}_2\text{O}_3:\text{Yb}$ , Ho powders for low-temperature thermometry based on up-conversion fluorescence". In: *Ceramics International* 39.2 (2013), pp. 1129–1134.
- [24] Bumsoo Han, Willard L Hanson, Karim Bensalah, Altug Tuncel, Joshua M Stern, and Jeffrey A Cadeddu. "Development of quantum dot-mediated fluorescence thermometry for thermal therapies". In: *Annals of biomedical engineering* 37.6 (2009), pp. 1230–1239.
- [25] Manjusha Ramakrishnan, Ginu Rajan, Yuliya Semenova, and Gerald Farrell. "Overview of fiber optic sensor technologies for strain/temperature sensing applications in composite materials". In: *Sensors* 16.1 (2016), p. 99.
- [26] Subramaniam Bagavathiappan, BB Lahiri, T Saravanan, John Philip, and T Jayakumar. "Infrared thermography for condition monitoring—A review". In: *Infrared Physics & Technology* 60 (2013), pp. 35–55.
- [27] Y. Yue and X. Wang. "Nanoscale thermal probing". In: *Nano Reviews* 3.11586 (2012).
- [28] Peter Löw, Beomjoon Kim, Nobuyuki Takama, and Christian Bergaud. "High-spatial-resolution surface-temperature mapping using fluorescent thermometry". In: *Small* 4.7 (2008), pp. 908–914.
- [29] P. D. Dragic, M. Cavillon, and J. Ballato. "Materials for optical fiber lasers: A review". In: *Applied Physics Reviews* 5.4 (2018), p. 041301. DOI: [10.1063/1.5048410](https://doi.org/10.1063/1.5048410).
- [30] Guokui Liu and Bernard Jacquier. *Spectroscopic properties of rare earths in optical materials*. Vol. 83. Springer Science & Business Media, 2006.
- [31] André Richter. *Laser parameters and performance of  $\text{Pr}^{3+}$ -doped fluorides operating in the visible spectral region*. Cuvillier Verlag, 2008.
- [32] Stephen Blundell. *Magnetism in condensed matter*. 2003.
- [33] H. Steinkemper, S Fischer, M Hermle, and J. C. Goldschmidt. "Stark level analysis of the spectral line shape of electronic transitions in rare earth ions embedded in host crystals". In: *New Journal of Physics* 15.053033 (2013).

- [34] A Richter, E Heumann, E Osiac, G Huber, W Seelert, and A Diening. "Diode pumping of a continuous-wave  $\text{Pr}^{3+}$ -doped  $\text{LiYF}_4$  laser". In: *Optics letters* 29.22 (2004), pp. 2638–2640.
- [35] Thomas Graf. *Laser*. Springer-Verlag, 2009.
- [36] S. Spelthann, J. Thiem, L. Neumann, H.-H. Johannes, W. Kowalsky, D. Kracht, J. Neumann, A. Ruehl, and D. Ristau. "Fluorescence Dynamics of Laseractive Nanocrystals Emitting in the Visible". In: *In Proceedings of the 2019 Conference on Lasers and Electro-Optics Europe & European Quantum Electronics Conference (CLEO/Europe-EQEC)* (2019).
- [37] GK Wertheim, MA Butler, KW West, and DNE Buchanan. "Determination of the Gaussian and Lorentzian content of experimental line shapes". In: *Review of Scientific Instruments* 45.11 (1974), pp. 1369–1371.
- [38] Nicholas Rivera and Ido Kaminer. "Light–matter interactions with photonic quasiparticles". In: *Nature Reviews Physics* 2.10 (2020), pp. 538–561.
- [39] Hermann Haken. *Laser light dynamics*. Vol. 1. North-Holland Amsterdam, 1985.
- [40] S. Spelthann, S. Unland, J. Thiem, F. Jakobs, J. Kielhorn, P. Y. Ang, H.-H. Johannes, D. Kracht, J. Neumann, A. Ruehl, W. Kowalsky, and D. Ristau. "Towards Highly Efficient Polymer Fiber Laser Sources for Integrated Photonic Sensors". In: *Sensors* 20.15 (2020), p. 4086.
- [41] NN Nedyalkov, SE Imamova, PA Atanasov, RA Toshkova, EG Gardeva, LS Yossifova, MT Alexandrov, and M Obara. "Interaction of gold nanoparticles with nanosecond laser pulses: Nanoparticle heating". In: *Applied surface science* 257.12 (2011), pp. 5456–5459.
- [42] Ali Rafiei Miandashti, Larousse Khosravi Khorashad, Alexander O. Govorov, Martin E. Kordesch, and Hugh H. Richardson. "Time-Resolved Temperature-Jump Measurements and Theoretical Simulations of Nanoscale Heat Transfer Using  $\text{NaYF}_4:\text{Yb}^{3+}:\text{Er}^{3+}$  Upconverting Nanoparticles". In: *The Journal of Physical Chemistry C* 123.6 (2019), pp. 3770–3780. DOI: [10.1021/acs.jpcc.8b11215](https://doi.org/10.1021/acs.jpcc.8b11215).
- [43] Michael Strasser, Kenji Setoura, Uwe Langbein, and Shuichi Hashimoto. "Computational modeling of pulsed laser-induced heating and evaporation of gold nanoparticles". In: *The Journal of Physical Chemistry C* 118.44 (2014), pp. 25748–25755.
- [44] Viktor K Pustovalov. "Theoretical study of heating of spherical nanoparticle in media by short laser pulses". In: *Chemical Physics* 308.1-2 (2005), pp. 103–108.

- [45] Christian Kränkel, Daniel-Timo Marzahl, Francesca Moglia, Günter Huber, and Philip Werner Metz. “Out of the blue: semiconductor laser pumped visible rare-earth doped lasers”. In: *Laser Photonics Rev.* 10.4 (2016), pp. 548–568.
- [46] Wolfgang Demtröder. *Experimentalphysik 3: Atome, Moleküle und Festkörper*. Springer-Verlag, 2016.
- [47] Yizhe An, Andrew Duhaime, and P Stanley May. “Optical observation of the kinetics of thermalization between the  $^3P_0$  and  $^3P_1$  excited states of  $Pr^{3+}$  in symmetrical  $Pr^{3+}$ – $Gd^{3+}$  pairs in  $CsCdBr_3$ ”. In: *Journal of luminescence* 111.3 (2005), pp. 131–138.
- [48] Dechao Yu, John Ballato, and Richard E Riman. “Temperature-dependence of multiphonon relaxation of rare-earth ions in solid-state hosts”. In: *The Journal of Physical Chemistry C* 120.18 (2016), pp. 9958–9964.
- [49] H Warren Moos. “Spectroscopic relaxation processes of rare earth ions in crystals”. In: *Journal of Luminescence* 1 (1970), pp. 106–121.
- [50] Hao Wu, Zhengdong Hao, Liangliang Zhang, Xia Zhang, Yu Xiao, Guo-Hui Pan, Huajun Wu, Yongshi Luo, Haifeng Zhao, and Jiahua Zhang. “Phonon energy dependent energy transfer upconversion for the red emission in the  $Er^{3+}/Yb^{3+}$  System”. In: *The Journal of Physical Chemistry C* 122.17 (2018), pp. 9611–9618.
- [51] Ferda Canbaz, Ismail Yorulmaz, and Alphan Sennaroglu. “2.3- $\mu m$   $Tm^{3+}$ : YLF laser passively Q-switched with a  $Cr^{2+}$ : ZnSe saturable absorber”. In: *Optics letters* 42.9 (2017), pp. 1656–1659.
- [52] Mochen Jia, Zhen Sun, Mingxuan Zhang, Hanyu Xua, and Zuoling Fu. “What determines the performance of lanthanide-based ratiometric nanothermometers?” In: *Nanoscale* 12 (2020), pp. 20776–20785.
- [53] Maxim Demesh, Daniel-Timo Marzahl, Anatol Yasukevich, Viktor Kisel, Günter Huber, Nikolay Kuleshov, and Christian Kränkel. “Passively Q-switched Pr:YLF laser with a  $Co^{2+}$ : $MgAl_2O_4$  saturable absorber”. In: *Optics letters* 42.22 (2017), pp. 4687–4690.
- [54] Marcin Runowski, Przemysław Woźny, Inocencio R Martín, Víctor Lavín, and Stefan Lis. “Praseodymium doped  $YF_3$ :  $Pr^{3+}$  nanoparticles as optical thermometer based on luminescence intensity ratio (LIR)–Studies in visible and NIR range”. In: *Journal of Luminescence* 214 (2019), p. 116571.
- [55] William J Miniscalco and Richard S Quimby. “General procedure for the analysis of  $Er^{3+}$  cross sections”. In: *Optics letters* 16.4 (1991), pp. 258–260.

- [56] RS Quimby. "Range of validity of McCumber theory in relating absorption and emission cross sections". In: *Journal of applied physics* 92.1 (2002), pp. 180–187.
- [57] RM Martin and RS Quimby. "Experimental evidence of the validity of the McCumber theory relating emission and absorption for rare-earth glasses". In: *JOSA B* 23.9 (2006), pp. 1770–1775.
- [58] SR Bowman, LB Shaw, BJ Feldman, and Joseph Ganem. "A 7- $\mu\text{m}$  praseodymium-based solid-state laser". In: *IEEE journal of quantum electronics* 32.4 (1996), pp. 646–649.
- [59] D Downs, J Murray, and W Lowdermilk. "Stabilizing the output of a Q-switched laser". In: *IEEE Journal of Quantum Electronics* 14.8 (1978), pp. 571–573.
- [60] D.C. Brown and H.J. Hoffman. "Thermal, Stress, and Thermo-Optic Effects in High Average Power Double-Clad Silica Fiber Lasers". In: *IEEE JOURNAL OF QUANTUM ELECTRONICS* 37.2 (2001).
- [61] Albert Einstein. "Über die von der molekularkinetischen Theorie der Wärme geforderte Bewegung von in ruhenden Flüssigkeiten suspendierten Teilchen". In: *Annalen der physik* 4 (1905).
- [62] Ping Chen, Junpei Zhang, Beibei Xu, Xiangwen Sang, Weibo Chen, Xiaofeng Liu, Junbo Han, and Jianrong Qiu. "Lanthanide doped nanoparticles as remote sensors for magnetic fields". In: *Nanoscale* 6.19 (2014), pp. 11002–11006.
- [63] A Guhur and SD Jackson. "Efficient holmium-doped fluoride fiber laser emitting 2.1  $\mu\text{m}$  and blue upconversion fluorescence upon excitation at 2  $\mu\text{m}$ ". In: *Optics express* 18.19 (2010), pp. 20164–20169.
- [64] L Esterowitz, FJ Bartoli, RE Allen, DE Wortman, CA Morrison, and RP Leavitt. "Energy levels and line intensities of  $\text{Pr}^{3+}$  in  $\text{LiYF}_4$ ". In: *Physical Review B* 19.12 (1979), p. 6442.
- [65] R. Moncorgé, A. Braud, P. Camy, and J.L. Doualan. "2 - Fluoride laser crystals". In: *Handbook of Solid-State Lasers*. Ed. by B. Denker and E. Shklovsky. Woodhead Publishing Series in Electronic and Optical Materials. Woodhead Publishing, 2013, pp. 28–53. ISBN: 978-0-85709-272-4.
- [66] Alexander A Kaminskii. "Laser crystals and ceramics: recent advances". In: *Laser & Photonics Reviews* 1.2 (2007), pp. 93–177.
- [67] F Cornacchia, Alberto Di Lieto, Mauro Tonelli, A Richter, E Heumann, and G Huber. "Efficient visible laser emission of GaN laser diode pumped Pr-doped fluoride scheelite crystals". In: *Optics express* 16.20 (2008), pp. 15932–15941.

- [68] Tuhin Samanta, Sourav Kanti Jana, Athma E Praveen, and Venkataramanan Mahalingam. "Ligand sensitized strong luminescence from Eu  $3+$ -doped LiYF<sub>4</sub> nanocrystals: a photon down-shifting strategy to increase solar-to-current conversion efficiency". In: *Dalton Transactions* 46.29 (2017), pp. 9646–9653.
- [69] L. Neumann, F. Jakobs, S. Spelthann, D. Zaremba, S. Radunz, U. Resch-Genger, R. Evert, J. Kielhorn, W. Kowalsky, and H.-H. Johannes. "Integration of b-NaYF<sub>4</sub> Upconversion Nanoparticles into Polymers for Polymer Optical Fiber Applications". In: *Opt. Spectrosc.* 128 (2018), 711–715.
- [70] Xun Wang, Jing Zhuang, Qing Peng, and Yadong Li. "Hydrothermal synthesis of rare-earth fluoride nanocrystals". In: *Inorganic chemistry* 45.17 (2006), pp. 6661–6665.
- [71] Bartłomiej Sojka, Miroslava Kuricova, Aurelia Liskova, Maria Bartusova, Mateusz Banski, Jan Misiewicz, Maria Dusinska, Mira Horvathova, Eva Jahnova, Silvia Ilavska, et al. "Hydrophobic sodium fluoride-based nanocrystals doped with lanthanide ions: assessment of in vitro toxicity to human blood lymphocytes and phagocytes". In: *Journal of Applied Toxicology* 34.11 (2014), pp. 1220–1225.
- [72] Su Yeon Kim, Jong Seok Jeong, K Andre Mkhoyan, and Ho Seong Jang. "Direct observation of the core/double-shell architecture of intense dual-mode luminescent tetragonal bipyramidal nanophosphors". In: *Nanoscale* 8.19 (2016), pp. 10049–10058.
- [73] Stefan Wilhelm, Martin Kaiser, Christian Würth, Josef Heiland, Carolina Carrillo-Carrion, Verena Muhr, Otto S Wolfbeis, Wolfgang J Parak, Ute Resch-Genger, and Thomas Hirsch. "Water dispersible upconverting nanoparticles: effects of surface modification on their luminescence and colloidal stability". In: *Nanoscale* 7.4 (2015), pp. 1403–1410.
- [74] Juan Wang, Feng Wang, Jun Xu, Yong Wang, Yongsheng Liu, Xueyuan Chen, Hongyu Chen, and Xiaogang Liu. "Lanthanide-doped LiYF<sub>4</sub> nanoparticles: Synthesis and multicolor upconversion tuning". In: *Comptes Rendus Chimie* 13.6-7 (2010), pp. 731–736.
- [75] F. Wang, Y. Han, C.S. Lim, Y. Lu, J. Wang, J. Xu, H. Chen, C. Zhang, M. Hong, and X. Liu. "Simultaneous phase and size control of upconversion nanocrystals through lanthanide doping". In: *Nature* 463 (2010), 1061–1065.
- [76] Angang Dong, Xingchen Ye, Jun Chen, Yijin Kang, Thomas Gordon, James M Kikkawa, and Christopher B Murray. "A generalized ligand-exchange strategy enabling sequential surface

- functionalization of colloidal nanocrystals". In: *Journal of the American Chemical Society* 133.4 (2011), pp. 998–1006.
- [77] L Marciniak, K Prorok, and A Bednarkiewicz. "Size dependent sensitivity of Yb<sup>3+</sup>, Er<sup>3+</sup> up-converting luminescent nanothermometers". In: *Journal of Materials Chemistry C* 5.31 (2017), pp. 7890–7897.
- [78] L Marciniak, K Prorok, A Bednarkiewicz, A Kowalczyk, D Hreniak, and W Strek. "Water dispersible LiNdP<sub>4</sub>O<sub>12</sub> nanocrystals: New multifunctional NIR–NIR luminescent materials for bio-applications". In: *Journal of Luminescence* 176 (2016), pp. 144–148.
- [79] Leyu Wang and Yadong Li. "Controlled synthesis and luminescence of lanthanide doped NaYF<sub>4</sub> nanocrystals". In: *Chemistry of Materials* 19.4 (2007), pp. 727–734.
- [80] Tomohiro Sago, Hiroshi Ishii, Hideaki Hagihara, Noriyuki Takada, and Hiroyuki Suda. "Analysis of chemiluminescence spectra in oxidative degradation of oleic acid". In: *Chemical Physics Letters* 565 (2013), pp. 138–142.
- [81] Renfu Li, Xiaodie Fang, Jilou Ren, Baojun Chen, Xiaoyun Yuan, Xuechun Pan, Peng Zhang, Lantian Zhang, Datao Tu, Zhenlan Fang, et al. "The Effect of Surface-Capping Oleic Acid on the Optical Properties of Lanthanide-Doped Nanocrystals". In: *Nanoscale* (2021).
- [82] Michael Steinke, Simon Spelthann, Axel Rühl, and Detlev Ristau. "Absorption and multi-phonon quenching in nanocrystal doped SiO<sub>2</sub> fibers". In: *Optical Materials Express* 11.6 (2021), pp. 1631–1642.
- [83] L. Lia, F. Qina, Y. Zhoua, Y. Zhengb, H. Zhaoc, and Z Zhanga. "Study on the thermal sensitivity of b-NaYF<sub>4</sub>:Yb<sup>3+</sup>-Er<sup>3+</sup> nanothermometers based on luminescence ratiometric technology". In: *Curr. Appl. Phys.* 19 (2019), pp. 480–485.
- [84] Y. Zhang, B. Chen, S. Xu, X. Li, J. Zhang, J. Sun, H. Zheng, L. Tong, G. Sui, H. Zhong, and et al. "Dually functioned core-shell NaYF<sub>4</sub>:Er<sup>3+</sup>/Yb<sup>3+</sup> @NaYF<sub>4</sub>:Tm<sup>3+</sup>/Yb<sup>3+</sup> nanoparticles as nanocalorifiers and nano-thermometers for advanced photothermal therapy". In: *Sci. Rep.* 9 (2017), p. 11849.
- [85] B. Dong, R.N. Hua, B.S. Cao, Z.P. Li, Y.Y. He, Z.Y. Zhanga, and O.S. Wolfbeis. "Size dependence of the upconverted luminescence of NaYF<sub>4</sub>:Er,Yb microspheres for use in ratiometric thermometry". In: *Phys. Chem. Chem. Phys.* 16 (2014), 20009–20012.



- [86] V. I. Sokolov, A. V. Zvyagin, S. M. Igumnov, S. I. Molchanova, M. M. Nazarov, A. V. Nechaev, A. G. Savelyev, A.A. Tyutyunov, E. V. Khaydukov, and V. Ya. Panchenko. "Determination of the Refractive Index of  $\beta$ -NaYF<sub>4</sub>/Yb<sup>3+</sup>/Er<sup>3+</sup>/Tm<sup>3+</sup> Nanocrystals Using Spectroscopic Refractometry". In: *OPTICS AND SPECTROSCOPY* 118.4 (2015).
- [87] Y. Koike. *Fundamentals of Plastic Optical Fibers*. 2nd. Weinheim, Germany: Wiley-VCH Verlag GmbH & Co. KGaA, 2015.
- [88] R. Evert, D. Zaremba, F. Jakobs, R. Caspary, W. Kowalsky, and H.-H. Johannes. "Application of thermography for thermoplastic waveguide fabrication". In: *Polym. Int.* 67 (2018), 1164–1169.
- [89] R. Caspary, F. Jakobs, J. Kielhorn, P.Y. Ang, M. Cehovski, M. Beck, H.-H. Johannes, S. Balendat, J. Neumann, S. Unland, S. Spelthann, J. Thiem, A. Ruehl, D. Ristau, and W. Kowalsky. "Polymer Fiber Lasers". In: *In Proceedings of the 2019 21st International Conference on Transparent Optical Networks (ICTON)* 67 (2019), 1–4.
- [90] D. Zaremba, R. Evert, L. Neumann, R. Caspary, W. Kowalsky, H. Menzel, and H.-H. Johannes. "Methacrylate-Based Copolymers for Polymer Optical Fibers". In: *Polymers* 9 (2017).
- [91] J. Zubia and J. Arrue. "Plastic Optical Fibers: An Introduction to Their Technological Processes and Applications". In: *Optical Fiber Technology* 7 (2001).
- [92] Toshikuni Kaino, Michiya Fujiki, Shigeru Oikawa, and Shigeo Nara. "Low-loss plastic optical fibers". In: *Applied Optics* 20.17 (1981), pp. 2886–2888.
- [93] W. Groh. "Overtone absorption in macromolecules for polymer optical fibers". In: *Makromol. Chem.* 189 (1988), 2861–2874.
- [94] A. Tapetado, P. J. Pinzon, J. Zubia, and C. Vazquez. "Polymer Optical Fiber Temperature Sensor With Dual-Wavelength Compensation of Power Fluctuations". In: *J. Light. Technol.* 33 (2015), pp. 2716–2723.
- [95] Pat W Trezona. "Derivation of the 1964 CIE 10° XYZ colour-matching functions and their applicability in photometry". In: *Color Research & Application: Endorsed by Inter-Society Color Council, The Colour Group (Great Britain), Canadian Society for Color, Color Science Association of Japan, Dutch Society for the Study of Color, The Swedish Colour Centre Foundation, Colour Society of Australia, Centre Français de la Couleur* 26.1 (2001), pp. 67–75.
- [96] Brian M Walsh, Uwe Hommerich, Akira Yoshikawa, and Alessandra Toncelli. "Mid-infrared spectroscopy of Pr-doped materials". In: *Journal of Luminescence* 197 (2018), pp. 349–353.

- [97] Hannes Rijckaert and Anna M Kaczmarek. "Ho<sup>3+</sup>-Yb<sup>3+</sup> doped NaGdF<sub>4</sub> nanothermometers emitting in BW-I and BW-II. Insight into the particle growth intermediate steps". In: *Chemical Communications* 56.92 (2020), pp. 14365–14368.
- [98] MJ Assael, S Botsios, K Gialou, and IN Metaxa. "Thermal conductivity of polymethyl methacrylate (PMMA) and borosilicate crown glass BK7". In: *International Journal of Thermophysics* 26.5 (2005), pp. 1595–1605.
- [99] A. Leal-Junior, A. Frizzera-Neto, C. Marques, and M. José Pontes. "A Polymer Optical Fiber Temperature Sensor Based on Material Features". In: *Sensors* 18 (2018), p. 301.
- [100] A. Tapetado, C. Vázquez Garcia, J. Zubia Zaballa, and J. Arrie. "A Temperature Sensor Based on a Polymer Optical Fiber Macro-Bend". In: *Sensors* 13 (2013), 13076–13089.
- [101] I. Parola, E. Arrospide, F. Recart, M.A. Illarramendi, G. Durana, N. Guarrotxena, O. García, and J. Zubia. "Fabrication and Characterization of Polymer Optical Fibers Doped with Perylene-Derivatives for Fluorescent Lighting Applications". In: *Fibers* 5.28 (2017).
- [102] Martin Mühlenweg, Gregor Schaefer, and Siegfried Trattnig. "Physikalische Wechselwirkungen in der MRT". In: *Der Radiologe* 55.8 (2015), pp. 638–648.
- [103] Ernst Abbe. "Beiträge zur Theorie des Mikroskops und der mikroskopischen Wahrnehmung". In: *Archiv für mikroskopische Anatomie* 9.1 (1873), pp. 413–468.
- [104] S. W. Hell and J. Wichmann. "Breaking the diffraction resolution limit by stimulated emission: stimulated-emission-depletion fluorescence microscopy". In: *Optics Letters* 19.11 (1994), pp. 780–782.
- [105] B. Harke, J. Keller, C. K. Ullal, V. Westphal, A. Schönle, and S. W. Hell. "Resolution scaling in STED microscopy". In: *Optics Express* 16.6 (2008), p. 4154.
- [106] L. Liang and X. Liu. "STED Nanoscopy Goes Low Power". In: *Chem* 2 (2017), pp. 326–333.
- [107] G. Vicidomini, G. M., K. Y. Han, V. Westphal, H. Ta, M. Reuss, J. Engelhardt, C. Eggeling, and S. W Hell. "Sharper low-power STED nanoscopy by time gating". In: *nature methods* 8.7 (2011).
- [108] G.R. Hadley. "Wide-angle beam propagation using Padé approximant operators". In: *Optics Letters* 17.20 (1992), pp. 1426–1428.
- [109] G. Cox and C. J. R. Sheppard. "Practical Limits of Resolution in Confocal and Non-Linear Microscopy". In: *MRT* 63.1 (2003), pp. 18–22.

- [110] Ginés Lifante Pedrola. *Special Topics on BPM*. John Wiley & Sons, Ltd, 2016, pp. 130–165.
- [111] John Crank and Phyllis Nicolson. “A practical method for numerical evaluation of solutions of partial differential equations of the heat-conduction type”. In: *Mathematical Proceedings of the Cambridge Philosophical Society*. Vol. 43. 1. Cambridge University Press. 1947, pp. 50–67.
- [112] G Ronald Hadley. “Multistep method for wide-angle beam propagation”. In: *Optics Letters* 17.24 (1992), pp. 1743–1745.
- [113] S. W. Hell, S. Lindek, C. Cremer, and E. H. K. Stelzer. “Measurement of the 4Pi-confocal point spread function proves 75 nm axial resolution”. In: *Applied Physics Letters* 64.11 (1994), pp. 1335–1337.
- [114] E. C. Ximendes, U. Rocha, T. O. Sales, N. Fernández, F. Sanz-Rodríguez, I. R. Martín, C. Jacinto, and D. Jaque. “In Vivo Subcutaneous Thermal Video Recording by Supersensitive Infrared Nanothermometers”. In: *Adv. Funct. Mater.* 27.1702249 (2017).
- [115] S.B.Field and N.M.Bleehen. “Hyperthermia in the treatment of cancer”. In: *Cancer Treatment Reviews* 6.2 (1979), pp. 63–94.
- [116] M. Jiang, A. Ping Zhang, Wang Y.-C., H.-Y. Tam, and S. He. “Fabrication of a compact reflective long-period grating sensor with a cladding-mode-selective fiber end-face mirror”. In: *Opt. Express* 17 (2009), p. 17976.
- [117] X. Wang, M. Jiang, Z. Zhou, J. Gou, and D. Hui. “3D printing of polymer matrix composites: A review and prospective”. In: *Compos. B Eng.* 110 (2017), pp. 442–458.
- [118] Joana Costa Martins, Ana RN Bastos, Rute AS Ferreira, Xin Wang, Guanying Chen, and Luís D Carlos. “Primary Luminescent Nanothermometers for Temperature Measurements Reliability Assessment”. In: *Advanced Photonics Research* 2.5 (2021), p. 2000169.



Part VI

APPENDIX



## PUBLICATIONS

The ideas and figures presented in this work may have previously appeared in some of the following publications:

- [1] J. Thiem, S. Spelthann, J. Neumann, A. Ruehl, and D. Ristau. "Three-dimensional nanothermometry below the diffraction limit". In: *Optics Letters* 46.14 (2021), pp. 3352–3355.
- [2] J. Thiem, A. Ruehl, and D. Ristau. "Influence of Pumping Regime on Temperature Resolution in Nanothermometry". In: *Nanomaterials* 11.7 (2021), p. 1782.
- [3] J. Thiem, S. Spelthann, L. Neumann, F. Jakobs, H.-H. Johannes, W. Kowalsky, D. Kracht, J. Neumann, A. Ruehl, and D. Ristau. "Upconversion Nanocrystal Doped Polymer Fiber Thermometer". In: *Sensors* 20.21 (2020), p. 6048.
- [4] J. Thiem, S. Spelthann, L. Neumann, H.-H. Johannes, W. Kowalsky, D. Kracht, J. Neumann, A. Ruehl, and D. Ristau. "Laseraktive Nanokristalle für Polymerfasern (POF)". In: *Tagungsband Drittes Deutsches POF-Symposium*. 2020, pp. 43–58.
- [5] S. Spelthann, S. Unland, J. Thiem, F. Jakobs, J. Kielhorn, P. Y. Ang, H.-H. Johannes, D. Kracht, J. Neumann, A. Ruehl, W. Kowalsky, and D. Ristau. "Towards Highly Efficient Polymer Fiber Laser Sources for Integrated Photonic Sensors". In: *Sensors* 20.15 (2020), p. 4086.
- [6] J. Thiem, S. Spelthann, L. Neumann, H.-H. Johannes, W. Kowalsky, D. Kracht, J. Neumann, A. Ruehl, and D. Ristau. "Design and optimization of laseractive nanoparticles for fiber lasers". In: *2019 Conference on Lasers and Electro-Optics Europe & European Quantum Electronics Conference (CLEO/Europe-EQEC)*. IEEE. 2019, pp. 1–1.
- [7] S. Spelthann, J. Thiem, L. Neumann, H.-H. Johannes, W. Kowalsky, D. Kracht, J. Neumann, A. Ruehl, and D. Ristau. "Fluorescence Dynamics of Laseractive Nanocrystals Emitting in the Visible". In: *In Proceedings of the 2019 Conference on Lasers and Electro-Optics Europe & European Quantum Electronics Conference (CLEO/Europe-EQEC)* (2019).
- [8] R. Caspary, F. Jakobs, J. Kielhorn, P.Y. Ang, M. Cehovski, M. Beck, H.-H. Johannes, S. Balendat, J. Neumann, S. Unland, S. Spelthann, J. Thiem, A. Ruehl, D. Ristau, and W. Kowalsky. "Polymer Fiber Lasers". In: *In Proceedings of the 2019 21st Inter-*

- national Conference on Transparent Optical Networks (ICTON) 67* (2019), 1–4.
- [9] K. Kiedrowski, J. Thiem, F. Jakobs, J. Kielhorn, I. Balasa, D. Kracht, and D. Ristau. “Determination of the laser-induced damage threshold of polymer optical fibers”. In: *Laser-Induced Damage in Optical Materials 2018: 50th Anniversary Conference*. Vol. 10805. International Society for Optics and Photonics. 2018, p. 108052C.
- [10] J. Thiem, N. Tinne, D. Kracht, J. Neumann, and D. Ristau. “Charakterisierung der optischen Dämpfung in passiven und aktiven polymeroptischen Fasern”. In: *DGaO-Proceedings (ISSN: 1614-8436)*. Deutsche Gesellschaft für angewandte Optik. 2018, 119. Tagung, Poster: P38.
- [11] D. Claus, J. Thiem, J. Hennenlotter, G. Pedrini, A. Stenzl, and W. Osten. “Iterative phase retrieval imaging based on variable wavefront curvature for biomedical imaging”. In: *Imaging Systems and Applications*. Optical Society of America. 2016, JW4A–25.



CURRICULUM VITAE

---

*Personal Details*

Name: Jonas Thiem

Date of Birth: 10.09.1989

Place of Birth: Bad Neuenahr-Ahrweiler

Nationality: German

*Education*

- 01.04.2017 – present    PhD Student at Leibniz University Hannover  
22.03.2016    Graduation Master degree (M.Sc.)
- 01.10.2013 – 01.04.2016    Studies of Photonic Engineering at University of Stuttgart  
Master Thesis: Phasenrekonstruktion mittels gekrümmter  
Beleuchtung angewandt auf medizinische Bildgebung
- 24.09.2013    Graduation Bachelor Degree (B.Eng.)
- 01.09.2010 – 30.09.2013    Studies of Physical Engineering at FH Aachen  
Bachelor Thesis: Struktur, thermische Ausdehnung und  
magnetische Eigenschaften von ternären  
Fluoridverbindungen
- 20.03.2009    Abitur, Privates Gymnasium der Ursulinen Calvarienberg  
Bad Neuenahr-Ahrweiler

*Professional Affiliations*

- 01.08.2020 – 31.12.2020    Research Associate at Laser Zentrum Hannover e.V.
- 01.04.2017 – 31.07.2020    Research Associate at Leibniz University Hannover



## ACKNOWLEDGMENTS

---

First of all I would like to thank Prof. Dr. Detlev Ristau for supervising my thesis and for his support during its creation.

I would also like to thank Prof. Dr. Martina Gerke and Prof. Dr. Bernhard Roth for the acceptance of its evaluation.

I am grateful to Dr. Axel Ruehl for his immense professional support and his continuous help with searching for the golden thread.

I am thankful to Simon Spelthann for countless interesting discussions and his help in developing new ideas for my work. In this context I would also like to thank all the people that worked with me in R163 for their professional assistance and the excellent spirit beyond that.

I would like to thank Dr. Joerg Neumann and the people from the laser development department for providing a welcoming atmosphere over the last years and their assistance during the time I stayed at the Laser Zentrum Hannover.

Let me also thank my fellow colleagues from the Technische Universität Braunschweig for providing the samples used in this work and for their flexible collaboration during the LaPOF Project.

Last but not least I am deeply grateful to my family and friends for all the support they have given me over the years.